Modélisation du comportement des sédiments riches en hydrates de gaz via l'homogénéisation des propriétés micro-mécaniques

Axelle Alavoine

Axelle Alavoine. Modélisation du comportement des sédiments riches en hydrates de gaz via l'homogénéisation des propriétés micro-mécaniques. Mécanique des matériaux [physics.class-ph]. Université Paris-Est, 2020. Français. NNT : 2020PESC1008 . tel-03020159

HAL Id: tel-03020159

https://pastel.hal.science/tel-03020159v1

Submitted on 23 Nov 2020

Thèse

soumise pour l'obtention du grade de
Docteur de l'Université Paris-Est
Ecole Doctorale Sciences, Ingénierie et Environnement (SIE)

par

Axelle Alavoine

Modélisation du comportement des sédiments riches en hydrates de gaz via l'homogénéisation des propriétés micro-mécaniques

Spécialité : *Géotechnique*

Thèse préparée au laboratoire Navier

Soutenue le 13 janvier 2020 devant un jury composé de :

J. Carlos Santamarina	KAUST	Rapporteur
Nabil Sultan	Ifremer	Rapporteur
Frédéric Collin	Université de Liège	Président
Sébastien Brisard	Ecole des Ponts ParisTech	Examinateur
Nicolas Espinoza	University of Texas at Austin	Examinateur
Anh Minh Tang	Ecole des Ponts ParisTech	Examinateur
Jean-Michel Pereira	Ecole des Ponts ParisTech	Directeur de thèse
Patrick Dangla	Ecole des Ponts ParisTech	Co-encadrant de thèse

Thèse

soumise pour l'obtention du grade de
Docteur de l'Université Paris-Est
Ecole Doctorale Sciences, Ingénierie et Environnement (SIE)

par

Axelle Alavoine

Modélisation du comportement des sédiments riches en hydrates de gaz via l'homogénéisation des propriétés micro-mécaniques

---

Spécialité : *Géotechnique*

Thèse préparée au laboratoire Navier

Acknowledgements/Remerciements

This thesis work carried out in the Navier laboratory was an unexpected opportunity for me to discover the world of research in the best possible conditions. Over the past three years, I have been able to benefit from the knowledge and support of many people without whom this manuscript would not have been possible, and whom I would like to thank.

It was while looking for an internship to complete my Master's degree in geotechnical research that I entered Jean-Michel Pereira's office in 2016 and I had no idea that I would come out of it with a thesis topic. So I thank him very much, as well as Patrick Dangla for giving me this opportunity and for having accompanied me from the very beginning. I have greatly appreciated the exchanges we have had, as well as the advice and experience you have brought me throughout my work. I would also like to thank you for the freedom of work that I have been able to enjoy and for your patience, because I know that I am not always the most organized person in my reflection and my presentations.

I thank J. Carlos Santamarina, Nabil Sultan, Frédéric Collin, Sébastien Brisard, Nicolas Espinoza and Anh Minh Tang for agreeing to form my thesis jury and for the review and enriching comments made on this thesis.

This work was funded by the French National Research Agency (ANR) within the framework of the HYDRE collaborative project, and I would like to thank the project coordinator Anh Minh Tang for his investment and for the organization of exchanges between the different laboratories. I would like to take this opportunity to thank Daniel Broseta, Nabil Sultan and their respective teams for their collaboration on this project, with a special mention to the team of the University of Pau for the welcome they gave me in their laboratory during one week. Thanks to Ross Brown and Dyhia Atig in particular, it was a pleasure for me to meet you and to discover your work.

I would like to thank the entire geotechnical team at the Navier laboratory for the wonderful welcome and the exceptional working atmosphere. Thanks to Sabrina who is no stranger to these extraordinary conditions, and who is always there to help the doctoral students and researchers of the laboratory. If my thesis does not include experimental tests in the laboratory, I still had the opportunity to intervene on the laboratory's practical courses and I would like to thank the technical team for their help (and for the coffee breaks): Emmanuel, Navier, Baptiste, Xavier and Loïc. Thanks to all the PhD students who crossed my path, with whom I had the chance to share an office, travel to conferences, share events outside or just lunch. I am thinking in particular of Benjamin, Xiu, Youssouf, Tan, Alexandre, Philipp, Hadrien, Nick, Sophie, Rawaz, Radja, Feng, and especially Anaïs with whom my tandem of the last seven years of study is coming to an end.

Je termine en français en remerciant toutes les personnes ayant contribué indirectement au bon déroulement de ces trois années de thèse par leurs encouragements, et les moments passés ensemble, à savoir ma famille et mes amis. Je remercie ceux qui ont pu faire le déplacement le jour de la soutenance, notamment depuis le bout du monde. Merci à mes parents d'avoir su témoigner leur soutien tout au long de mon parcours et ce malgré les quelques milliers de kilomètres qui nous séparent, et à mon frère pour la relation qui est la nôtre. Enfin, je réserve mes derniers remerciements à YaYa qui m'a le plus supportée ces dernières années; le meilleur coloc', meilleur ami et meilleur compagnon que je puisse avoir.

Abstract

Gas hydrates represent a potential energy resource, but also a risk of instability for the environment (slope instability, global warming) that it is essential to control. The study of gas hydrate bearing soils, most often located on the ocean floor or in permafrost regions, is therefore a major challenge. The formation and dissociation of gas hydrates in these soils modifies the microstructure and the physical properties of the material with it. The objective of the thesis was therefore to develop a model that could predict the behaviour of soils containing gas hydrates, initially at the scale of the conventional laboratory sample. Several multi-physical numerical models applied to gas hydrate bearing soils have already been published, but the mechanical part is still relatively new due to the lack of experimental data and the relatively late interest shown by the community of mechanics in this subject.

Based on this observation, we first focused our analysis on the mechanical behaviour. The results of tests performed on sediments containing methane hydrates available in the literature have been used as a basis for analysing the effect of hydrates on the mechanical properties of a soil. In particular, the relationship between the elastic moduli of a soil and the volume fraction of hydrates was determined using an analytical homogenisation calculation. However, sediments containing gas hydrate inclusions exhibit macroscopic behaviour that is far from being linear elastic. The latter is strongly related to the different physical and morphological characteristics of both matrix sediments and hydrates that form in the pore space.

These observations therefore led to the application of a numerical homogenisation method based on Fast Fourier Transforms (FFT). This method allows for the use of elastoplastic laws and complex geometries in order to define the components of the microstructure of the material. The obtained results can therefore be used to determine an appropriate macroscopic nonlinear constitutive model for the type of sediment/hydrate composite that we wish to simulate.

The presented implementations were then integrated into a finite element simulation code first at the scale of the laboratory sample. The mechanical behaviour could be defined either by analytical homogenisation laws or by multi-scale calculations. The numerical homogenisation calculation by FFT is carried out at the microstructure scale at each Gauss integration point.

Keywords: gas hydrates, sediments, numerical, homogenisation, Fourier transforms

Résumé

Les hydrates de gaz représentent une ressource énergétique potentielle importante, mais aussi un risque d'instabilité pour l'environnement (mouvements de terrain, réchauffement climatique) qu'il est essentiel de maîtriser. L'étude des sols enrichis en hydrates de gaz, le plus souvent localisés au niveau des fonds océaniques ou du pergélisol, représente donc un enjeu majeur. La formation comme la dissociation d'hydrates dans ces sols modifie la microstructure et avec elle les propriétés physiques du matériau. L'objectif de la thèse a donc été de développer un modèle qui puisse permettre de prédire le comportement des sols contenant des hydrates de gaz, dans un premier temps à l'échelle de l'éprouvette de laboratoire classique. Plusieurs modèles de calculs multi-physiques appliqués aux sols enrichis en hydrates de gaz ont déjà été publiés, cependant la partie mécanique reste encore assez peu développée du fait du manque de données expérimentales, et de l'intérêt assez tardif porté par la communauté des mécaniciens au sujet.

En partant de ce constat, nous avons d'abord concentré notre analyse sur le comportement mécanique. Les résultats d'essais sur des sédiments riches en hydrates de méthane disponibles dans la littérature ont servi de base à l'analyse de l'effet des hydrates sur les propriétés mécaniques d'un sol. En particulier, la relation entre les modules élastiques d'un sol et la fraction volumique d'hydrates a été déterminée à l'aide d'un calcul d'homogénéisation analytique. Les sédiments contenant des inclusions d'hydrates de gaz présentent toutefois un comportement macroscopique loin d'être élastique linéaire. Ce dernier est fortement lié aux différentes caractéristiques physiques et morphologiques à la fois des sédiments matriciels et des hydrates formés dans l'espace des pores.

Ces observations ont donc conduit à l'application d'une méthode d'homogénéisation numérique basée sur les Transformées de Fourier Rapides (TFR). Cette méthode permet l'utilisation de lois élastoplastiques et de géométries complexes pour définir les composants de la microstructure du matériau à homogénéiser. Les résultats qui en découlent peuvent donc servir à déterminer un modèle macroscopique constitutif non-linéaire adapté au type de composite sédiment/hydrates que l'on souhaite simuler.

Les précédents développement ont par la suite été intégrés à un code de calcul aux éléments finis d'abord à l'échelle de l'échantillon de laboratoire. Le comportement mécanique pouvait être défini soit par les lois d'homogénéisation analytiques soit par calculs multi-échelles. Le calcul d'homogénéisation numérique par TFR est mené à l'échelle de la microstructure aux points d'intégrations de Gauss.

Mots-clefs: hydrates de gaz, sédiments, numérique, homogénéisation, transformées de Fourier

Contents

Introduction (English)

1

1.1 Context

Since their discovery at the beginning of the 19th century, gas hydrates have gone from being a scientific curiosity to being an industrial, environmental and energy issue. While the term "gas hydrates" is not widely used in our society today, it has gained notoriety in the scientific community and more particularly in offshore science, to such an extent that an International Conference on Gas Hydrates (triennial) was created in 1993, whose 9th edition welcomed around 800 participants in 2017. These compounds represent a major problem for oil and gas development, particularly with regard to flow assurance in production lines, since they can form in these pipelines and block them or at least significantly slow down the transport of fluids. It is this problem that led to the development of research on gas hydrates in the first place, before the discovery of natural hydrate deposits in the 1960s.

Since then, research on gas hydrates has expanded to include the study of these natural hydrate reservoirs found in the seabed and permafrost regions. Some exploration programs such as the Ocean Drilling Program, now replaced by the International Ocean Drilling Program, have contributed significantly to the discovery and analysis of marine sediments that naturally contain gas hydrates. Other programs, such as in Canada and Alaska, have focused on studying permafrost areas containing natural gas hydrate deposits. The vast majority of natural hydrates are made up of water and methane molecules due to their organic origin and the more stable crystalline hydrate structures formed with the methane molecule as guest. The conclusions of all of these studies over the past thirty years suggest that the hydrocarbon resource, and particularly the methane, that these gas hydrates represent, is much greater than the total hydrocarbon resources on land. Based on current knowledge, it can be estimated that 90% of the natural gas hydrate resources are found on the seabed, the rest in permafrost. Natural gas hydrates, as a global carbon reserve, have therefore quickly become an energy issue and some countries such as Japan are seriously considering exploiting them.

However, this resource remains difficult to access and very unstable. Gas hydrates are only stable at high pressures and low temperatures and dissociate relatively quickly under ambient pressure and temperature conditions. This instability of gas hydrates and their deep location make them difficult to observe and even more difficult to study. Exploration programs for natural gas hydrate deposits at sea represent a significant cost and although there are currently means available to drill pressure cores, the integrity of the samples is not always completely assured. To overcome these problems, methods for the synthesis of pure gas hydrates and gas hydrates in the pores of soil matrices have been developed in laboratories in order to study and characterise the behaviour of these compounds and their influence on the physical properties of soils, and this at a lower cost. Nevertheless, experimental protocols impose test conditions that are still difficult to implement and which, if not controlled, can have an influence on the results obtained and their interpretation.

Beyond the energy resource aspect, there are also environmental issues due to the fact that this carbon resource is unstable and is found in potentially sensitive areas or underwater formations such as slopes and continental margins, which could lead to landslides, for example. Current geological evidence from the seabed indicates that such underwater landslides related to gas hydrates have occurred in the past. The study of the physical properties of gas hydrate bearing sediments is therefore essential for safety reasons and if this kind of phenomenon is to be prevented in the future, particularly in the context of global warming, but especially if we decide to exploit this submarine resource. The behaviour of these sediments, however, involves several aspects of physics, including solid and fluid mechanics, thermodynamics, chemistry and phase changes. These are all areas where it is necessary to acquire data in order to lay the foundations for the most realistic behaviour model. An key aspect for the implementation of predictive models that has emerged in studies already carried out so far is the great diversity and heterogeneity of the materials that make up natural gas hydrate reservoirs. Soils with gas hydrates may indeed have different morphologies at the microstructure level as well as different volume fractions of phases and this seems to have a significant influence on the macroscopic behaviour of the material.

1.2 Objectives

This work is part of the HYDRE project (2015-2020), a collaborative research project funded by the Agence Nationale de la Recherche (ANR) under the reference ANR-15-CE06-0008. The objective of this project is to study the mechanical behaviour of sediments containing gas hydrates in order to reduce the environmental impact of a potential future exploitation of this resource. The project was therefore divided into four tasks in a multi-scale approach:

- a task 1 that studies the behaviour of gas hydrates at the pore scale, a few micrometers, in the presence of mineral substrates,

- a task 2 dedicated to the synthesis and experimental study of methane hydrates in granular soils at the scale of the representative elementary volume, i.e. a few millimetres to a few centimetres,

- a task 3 dedicated to the numerical modeling of the behaviour of gas hydrate bearing soils, in which my thesis work is integrated,

- and finally a task 4 which focuses on the analysis of macroscopic data, at the metre scale, acquired at sea by Ifremer on natural gas hydrate bearing sediments.

The initial objectives of the thesis were therefore to set up a poro-mechanical behaviour model for gas hydrate bearing soils. This macroscopic model had to take into account the effects of gas hydrates on the overall behaviour of the material. Macroscopic constitutive laws at the scale of the centimetric specimen had therefore to be defined and calibrated based in particular on the results of laboratory tests in the literature or obtained in task 2 by a team from our laboratory. These laws then had to be implemented in a finite element (FE) code in order to simulate the behaviour of a reservoir at a larger scale.

It became clear during the advancement of the thesis though, that several models have already been defined and calibrated on literature datasets with the same objectives. And relatively few models take into account the effect of microstructure and in particular hydrate morphology on the macroscopic response of these soils. It seemed interesting in our opinion to reorient the objectives of the thesis in order to include a micro-macro mechanical approach via homogenisation theories in order to better account for the heterogeneity effects of the microstructure but also the nonlinear behaviour of the phases that constitute these soils.

1.3 Thesis Structure

This thesis work is presented in 5 main chapters and one chapter presenting the conclusions and perspectives at the end of the dissertation.

Chapter 2 presents a state of the art review of gas hydrate research. It introduces gas hydrates and their properties before focusing on soils containing natural gas hydrates. The formation of these soils, their exploration, the issues related to these soils and their geophysical properties are presented. And in a final section we review advances in the numerical modeling of sediments containing gas hydrates.

Chapter 3 presents a first micro-mechanical approach used for the modeling of sediments with hydrates, namely an analytical homogenisation based on the Mori-Tanaka and Self-Consistent models. The analytical homogenisation approach is used for mechanical applications in comparison with experimental data. The limitations of the analytical approach in the case of sediments containing gas hydrates lead to the next chapter.

Chapter 4 proposes a numerical homogenisation approach based on spectral methods with discrete Fourier transforms. One method in particular is adopted for the development of a custom homogenisation calculation code. Simple applications in elasticity and plasticity are presented and compared to finite element homogenisation in order to validate the implementation of the code.

Chapter 5 then presents the application of the developed code to the case of gas hydrate bearing sediments. Different microstructures are presented and subjected to homogenisation calculations under different strain and/or stress loadings. Different soil types and pore occupancy modes of hydrates are analysed. The code is also applied to real microstructure images in 2D and 3D.

In chapter 6 we present the multi-scale approach we have adopted to incorporate the effective behaviour of soil microstructures with gas hydrates into a finite element calculation. We also present the method used to compute the macroscopic tangent matrix involved in the Newton-Raphson algorithm at the macroscopic scale. An example of the application of the Finite Element Method-Fast Fourier Transform (FEM-FFT) model is given at the end of the chapter.

Finally, the chapter 7 gathers the conclusions of this thesis work and presents the perspectives that it entails.

1

Introduction (français)

1.1 Contexte

Depuis leur découverte vers le début du $19^{\text{ème}}$ siècle les hydrates de gaz sont passés du statut de curiosité scientifique à celui d'enjeu à la fois industriel, environnemental et énergétique. Si l'expression 'hydrates de gaz' n'est pas courante dans notre société actuellement, elle a toutefois gagné en notoriété dans la communauté scientifique et plus particulièrement dans les sciences offshore, au point qu'une Conférence Internationale sur les Hydrates de Gaz (triennale) soit créée en 1993, dont la 9^{e} édition accueillait environ 800 participants en 2017. Ces composés représentent une problématique de taille pour l'exploitation pétrolière et gazière, notamment sur les questions d'écoulement des effluents dans les lignes de production, puisqu'ils peuvent se former dans ces lignes et les obstruer ou du moins fortement ralentir le transport des fluides. C'est cette problématique qui a conduit à un développement de la recherche sur les hydrates de gaz dans un premier temps, avant la découverte de gisements naturels d'hydrates à partir des années 1960.

Depuis, la recherche concernant les hydrates de gaz s'est élargie à l'étude de ces réservoirs naturels d'hydrates présents dans les fonds marins et les régions du pergélisol. Certains programmes d'exploration comme le Ocean Drilling Program, aujourd'hui remplacé par le International Ocean Drilling Program, ont fortement contribué à la découverte et l'analyse des sédiments marins contenant naturellement des hydrates de gaz. D'autres programmes, au Canada et en Alaska notamment, se sont attachés à l'étude de zones de pergélisol contenant des formations d'hydrates de gaz naturelles. La grande majorité des hydrates naturels est constitutée de molécules d'eau et de méthane du fait de leur origine organique et d'une plus grande stabilité des structures cristallines d'hydrates formées à partir de la molécule de méthane. Les conclusions de l'ensemble de ces études sur les trente dernières années laissent penser que la ressource en hydrocarbure, et particulièrement en méthane que représentent ces hydrates de gaz est bien plus importante que la totalité des ressources d'hydrocarbures à terre. L'état actuel des connaissances permet d'estimer que 90% des ressources naturelles d'hydrates de gaz se trouvent au niveau des fonds marins, le reste se trouvant dans le pergélisol. Les hydrates de gaz naturels, en tant que ressource de carbone mondiale sont donc devenus rapidement un enjeu énergétique et certains pays comme le Japon envisagent sérieusement de les exploiter.

Cependant, cette ressource reste difficilement accessible et très instable. Les hydrates de gaz ne sont stables qu'à hautes pressions et basses températures et se dissocient assez vite dans les conditions de pressions et température ambiantes. Ce caractère instable des hydrates de gaz et leur localisation profonde les rend difficiles ne serait-ce qu'à observer et encore plus à étudier. Les programmes de reconnaissances de gisements naturels d'hydrates de gaz en mer représentent un coût important et si des moyens existent aujourd'hui pour réaliser des carottages sous pression, l'intégrité des échantillons n'est pas toujours complètement assurée. Pour pallier ces problématiques, des methodes de synthèse d'hydrates de gaz purs et d'hydrates de gaz dans les pores de matrices de sols ont été développées en laboratoire afin de pouvoir tout de même étudier et caractériser le comportement de ces composés et leur influence sur les propriétés physiques des sols, tout cela à moindre coût. Néanmoins les protocoles expérimentaux imposent des conditions d'essai qui restent encore difficiles à mettre à place et qui, si elles ne sont pas maîtrisées, peuvent avoir une influence sur les résultats obtenus et sur leur interprétation.

Au-delà de l'aspect ressource énergétique, se posent également des questions environnementales dues au fait que cette ressource en carbone soit instable et se retrouve dans des endroits ou des formations sous-marines potentiellement sensibles comme des talus et des marges continentales, ce qui pourrait engendrer des glissements de terrains par exemple. Des traces géologiques actuelles au niveau des fonds marins attestent que de tels phénomènes de glissements de terrains sous-marins en lien avec les hydrates de gaz ont eu lieu par le passé. L'étude des propriétés physiques des sédiments riches en hydrates de gaz est donc importante pour des questions de sécurité et si l'on veut pouvoir prévenir ce genre de phénomène à l'avenir, notamment dans un contexte de réchauffement climatique, mais surtout si l'on décide d'exploiter cette ressource sous-marine. Toutefois le comportement de ces sédiments fait intervenir plusieurs aspects de la physique, que ce soit la mécanique du solide et des fluides, mais aussi la thermodynamique, la chimie et les changements de phases. Autant de domaines pour lesquels il est nécessaire d'acquérir des données afin de pouvoir poser les bases d'un modèle de comportement qui soit le plus réaliste possible. Un aspect important pour la mise en place de modèles prédictifs qui est apparu dans les études déjà réalisées jusqu'à présent est la grande diversité et l'hétérogénéité des matériaux qui composent les réservoirs naturels d'hydrates de gaz. Les sols avec hydrates de gaz peuvent en effet présenter différentes morphologies au niveau de leur microstructure ainsi que différentes fractions volumiques de phases et cela semble avoir une influence non négligeable sur le comportement macroscopique du matériau.

1.2 Objectifs

Ce travail de cette thèse s'inscrit dans le cadre du projet HYDRE (2015-2020), un projet de recherche collaboratif financé par l'Agence Nationale de la Recherche (ANR) sous la référence ANR-15-CE06-0008. L'objectif de ce projet est d'étudier le comportement mécanique des sédiments contenant des hydrates de gaz afin de pouvoir réduire l'impact environnemental d'une potentielle future exploitation de cette ressource. Le projet a pour cela été divisé en quatre tâches selon une approche multi-échelle :

- une tâche 1 qui s'intéresse à l'étude du comportement des hydrates de gaz à l'échelle des pores, soit quelques micromètres, en présence de substrats minéraux,
- une tâche 2 dédiée à la synthèse et l'étude des hydrates de méthane dans des sols granulaires à l'échelle du volume élémentaire représentatifs, soit quelques millimètres à quelques centimètres,
- une tâche 3 dédiée à la modélisation numérique du comportement des sols riches en hydrates de gaz dans laquelle s'intègre mon travail de thèse,
- et enfin une tâche 4 qui se concentre sur l'analyse de données macroscopiques, à l'échelle du mètre, acquises en mer par l'Ifremer sur les sediments naturellement riches en hydrates de gaz.

Les objectifs initiaux de la thèse étaient donc de mettre en place un modèle de comportement poro-mécanique pour les sols enrichis en hydrates de gaz. Ce modèle macroscopique devaient pouvoir tenir compte des effets des hydrates de gaz sur le comportement global du matériau. Des lois constitutives macroscopiques à l'échelle de l'éprouvette centimétrique devaient donc être définies et calibrées en se basant notamment sur les résultats d'essais en laboratoire de la littérature ou bien obtenus en tâche 2 par une équipe de notre laboratoire. Ces lois devaient être ensuite implémentées dans un code aux éléments finis afin de pouvoir simuler le comportement d'un réservoir à plus grande échelle.

Il est toutefois apparu lors de l'avancement de la thèse que plusieurs modèles ont déjà été définis et calibrés sur des jeux de données de la littérature selon les même objectifs. Et assez peu de modèles prennent en compte l'effet de la microstructure et notamment de la morphologie des hydrates sur la réponse macroscopique de ces sols. Il nous a paru intéressant de réorienter les objectifs de la thèse afin d'inclure une approche mécanique micro-macro via les théories d'homogénéisation pour pouvoir mieux rendre compte des effets d'hétérogénéité de la microstructure mais aussi des effets du comportement non linéaire des phases qui composent ces sols.

1.3 Structure de la thèse

Ce travail de thèse se présente en 5 chapitres principaux et un chapitre présentant les conclusions et perspectives en fin de rédaction.

Le chapitre 2 présente un état de l'art de la recherche sur les hydrates de gaz. Il introduit les hydrates de gaz et leur propriétés avant de s'intéresser aux sols contenant des hydrates de gaz naturels. La formation de ces sols, leur exploration, les enjeux qui y sont liés ainsi que leurs propriétés géophysiques sont présentées. Et dans une dernière section nous passons en revue les avancées dans le domaine de la modélisation numérique des sédiments contenant des hydrates de gaz.

Le chapitre 3 présente une première approche micro-mécanique utilisée pour la modélisation des sédiments avec hydrates, à savoir un calcul d'homogénéisation analytique basé sur les modèles de Mori-Tanaka et Auto-Cohérent. L'approche d'homogénéisation analytique est utilisée pour des calculs mécaniques et comparée à des résultats expérimentaux. Les limites de l'approche analytique dans le cas des sédiments contenant des hydrates de gaz conduisent au chapitre suivant.

Le chapitre 4 propose une approche d'homogénéisation numérique basée sur des méthodes spectrales avec transformées de Fourier discrètes. Une méthode en particulier est adoptée pour le développement d'un code maison de calcul d'homogénéisation. Des applications simples en élasticité et plasticité sont présentées et comparées à de l'homogénéisation par éléments finis afin de valider l'implémentation du code.

Le chapitre 5 présente ensuite l'application du code développé au cas des sédiments enrichis en hydrates de gaz. Différentes microstructures sont présentées et soumises à des calculs d'homogénéisations sous différents chargements en déformations et/ou contraintes. Les cas de différents types de sols et de différents modes d'occupation des pores par les hydrates sont analysés. Le code est également appliqué à des images de microstructures réelles en 2D et 3D.

Dans le chapitre 6 nous présentons l'approche multi-échelle que nous avons choisi d'adopter pour pouvoir intégrer le comportement effectif de microstructures de sols avec hydrates de gaz dans un calcul aux éléments finis. Nous présentons également la méthode utilisée pour le calcul de la matrice tangente macroscopique intervenant dans l'algorithme de

Newton-Raphson à l'échelle macroscopique. Un exemple d'application du modèle Eléments Finis-Transformées de Fourier Rapides (EF-TFR) est donné en fin de chapitre.

Finalement, le chapitre 7 fait le bilan de ce travail de thèse et présente les perspectives qui en découlent.

2

Literature review

This chapter introduces the research context of the thesis. Section 2.1 gives an overview of the characteristics of gas hydrates as well as the environmental and industrial aspects related to these compounds. Section 2.2 then focuses on the geomechanical properties of soils containing gas hydrates. And finally, section 2.3 presents the different advances in numerical modelling of the behaviour of these soils.

2.1 Gas hydrates and their properties

2.1.1 History of gas hydrates discovery

Gas hydrates are clathrates, crystalline structures generally consisting of two species. These are guest and host, where the guest lodges itself in the cavities of the structure formed by the other. In the case of gas hydrates, the host species is water and the guest is trapped hydrocarbon molecules. For the same hydrate, different species can fill the crystalline voids. However, methane hydrates are the most naturally distributed around the globe. The history of their discovery shows that these particular clathrates have only been known for a very short time, and the chronology of research can be divided into three main periods (Makogon, 2010; Sloan and Koh, 2007):

- A period of purely academic research, with few publications and authors, which began in 1810 with the discovery of the first gas hydrates (chlorine hydrates) by Sir Humphrey Davy (Cornwall, England). Industry was not interested in studying these compounds at all, and scientists at the time focused on identifying all compounds (usually inorganic) that could form hydrates as well as their compositions and physical properties. While, according to Sloan and Koh (2007), most researchers agree on the attribution of this discovery to Davy, some, such as Makogon (1997; 2010), believe that Joseph Priestley (Calne, England) observed the formation of sulphur dioxide hydrates thirty years earlier, in 1778.

- The second period begins in 1934, when Hammerschmidt (1934, Texas, United States) published the results of his inspection of American pipelines. Based on laboratory tests, he shows that hydrates form from circulating gas and block parts of the pipelines. The interest of the oil and gas industry for gas hydrates lead to an increase in the volume of published research in the field. Natural gas hydrates such as methane, ethane, and propane were most heavily analysed. At the time, studies were more concerned with the conditions leading to the formation of these hydrates.

- The discovery by the Soviets in 1967 of the first natural gas hydrate deposit in the permafrost (Messoyakha in Siberia) is the beginning of the third period of research for hydrates. This discovery showed that hydrates could form naturally in soils under certain conditions. Research in this field has increased further, this time with a particular focus on the coupled phenomena of geophysics and thermodynamics. In situ research has also been developed, and more than 230 gas hydrate deposits have been discovered (Makogon, 2010). Many countries have initiated programmes to study gas hydrates and their industrial exploitation.

2.1.2 Molecular structure and composition

The characteristics of gas hydrates revealed by the scientific community have been identified in the book *Clathrate Hydrates of Natural Gases* by Sloan and Koh (2007). The latter therefore explains that natural gas hydrates exist under three possible crystal structures (Fig. 2.1):

- The cubic structure I (sI) contains guest molecules with a diameter of 4.2 to 6 Å, which mainly concerns the following compounds: methane, ethane, carbon dioxide and hydrogen sulphide.

- The face-centered cubic structure II (sII) can contain molecules with a diameter of less than 4.2 Å such as nitrogen, but also molecules with a diameter between 6 and 7 Å (propane, isobutane).

- The hexagonal structure H (sH) is less known and may contain larger molecules, with diameters between 7 and 9 Å, associated with smaller ones such as methane or nitrogen.

Other structures have already been observed in the laboratory, such as the III-VII structures of Jeffrey (1984), or the T structure, but they are not formed from organic molecules as guests. According to Sloan and Koh (2007), these structures are relatively close to the structure of solid water. In addition, hydrogen bonds between water molecules are also at the basis of the interactions that govern these structures, made up of 85% by water. This is why some properties of hydrates are sometimes quite similar to those of ice. However, as we will in other sections some properties are specific to hydrates.

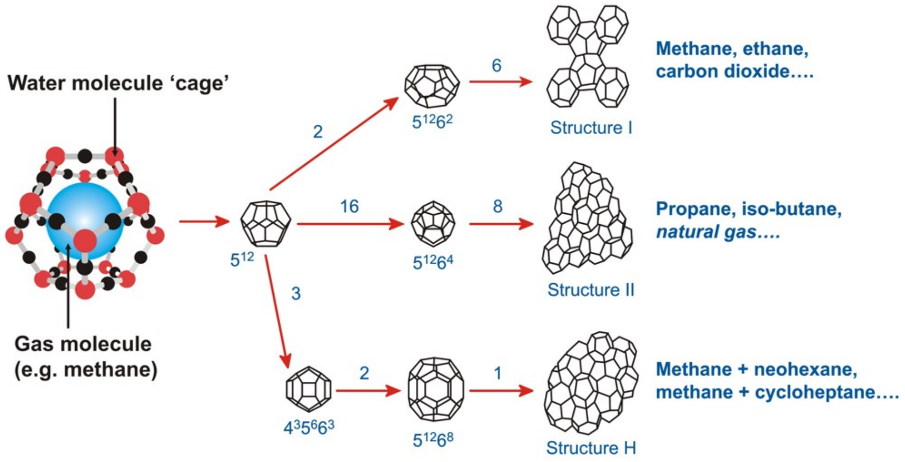

Fig. 2.1: Schematic of the types of cavities or cages formed by water molecules (hosting the guest molecules) and main gas hydrate structures composed of these cavities (from Heriot-Watt Institute of Petroleum Engineering (2018)). Notations under cavities represents the types and number of polygonal faces composing the cage types, for instance $5^{12}6^4$ indicates a cage composed of 12 pentagonal and four hexagonal faces. The numbers associated with arrows indicate the number of cage types constituting the crystal structure at the right.

The cavities enclosing the gas molecules and forming the various structures mentioned above are essentially formed by polyhedra composed of pentamers and hexamers of water molecules. The composition and, more importantly, the geometry of these cavities have been the subject of numerous analyses, which are also summarised in Sloan and Koh (2007). There are a very large number of these cavities and they are maintained thanks to the repellent forces exerted between the gas molecules they contain and the water molecules. There can only be one molecule inside a cavity except in the very rare case of hydrates subjected to very high pressures (Sloan and Koh, 2007). Such an in-depth study of gas hydrate structures provides access to the number of hydration, the number of moles of water per mole of gas in a hydrate structure. The methods for determining this number have evolved considerably and refined over time; the "Villard Rule" (Villard, 1895) estimated this number as 6 for different gases and gave the following formula: $\mathrm{M} + 6\mathrm{H_2O}$, where M represents one mole of gas. Today, the discovery of new crystalline hydrate structures and the non-stoichiometric nature of these compounds have led to the questioning of this rule. Indeed, if we take the case of the structures sI (which has 8 cavities for 46 water molecules) and sII (24 cavities for 136 water molecules), assuming that the gas fills all the cavities, their hydration number is then respectively:

$$n_H = \frac{46}{8} = 5.75 \quad \text{and} \quad n_H = \frac{136}{24} = 5.75$$

In reality, however, the number of hydration is higher than these theoretical values since gases do not necessarily fill all cavities. More precise techniques exist to evaluate n_H (Sloan and Koh, 2007), such as Raman spectroscopy, but we will not describe them in this section.

2.1.3 Phase equilibrium

For a given system, several variables can be used to describe the physical state in which it exists. The most well-known variables are generally the most easily accessible in the laboratory: pressure, temperature, concentrations, and volume. The important question is how many variables are needed to achieve a unique state of equilibrium. Gibbs' relationship allows us to calculate the variance (or the number of independent state parameters needed to specify the system) of a thermodynamic system (Gibbs, 1928):

$$v = c - r - k + n - \phi$$

with c being the number of components in the system; r the number of independent chemical equations; k the number of relationships imposed on the system; n the number of equilibrium factors (generally pressure and temperature, so that n is 2); ϕ the number of phases in the system. In the case of hydrate equilibrium we consider an isolated system ($k = 0$, no constraints imposed), without chemical reaction ($r = 0$) and whose equilibrium factors are pressure P and temperature T ($n = 2$), which gives the simplified relationship below:

$$v = c - \phi + 2$$

This relationship allows for a better comprehension of phase diagrams. In thermodynamics, phase diagrams are a very useful graphical tool for understanding the different equilibrium states of a pure substance, depending on two or three variables. The most common representations are in the Pressure-Temperature (P-T) plane, or the Pressure-Specific Volume (P-v) plane. In the case of hydrocarbon gas hydrates, the system is composed of two components, water and hydrocarbon, so $c = 2$. Several possibilities are conceivable for ϕ (ranging from 2 to 4). Depending on the number of phases, we can therefore choose either a maximum of two intensive variables fixing the state of equilibrium, or none at all: we then reach what is called a quadruple point, for which the pressure, temperature, as well as the quantities and volumes are unique. These relationships are made clear with the phase diagram of the water-methane system shown in Fig. 2.2, taken from the book of Sloan and Koh (2007).

The symbols used by the authors on the diagram refer to the different phases of the hydrocarbon (here, methane) and water: L_W corresponds to the liquid phase of water; H corresponds to hydrate; I corresponds to ice; and finally V corresponds to the vapour phase. Each line in Fig 2.2 represents a balance between three different phases, which implies a variance of one according to Gibbs' rule. Indeed, for a fixed temperature, only one pressure value allows to reach equilibrium, this value being imposed by the diagram. Similarly, the areas delimited by two lines of a diagram correspond to a balance between two constituent phases of the system. We have an infinite number of possible equilibrium pressures for a given temperature. For the observed temperature range, methane being not liquefiable,

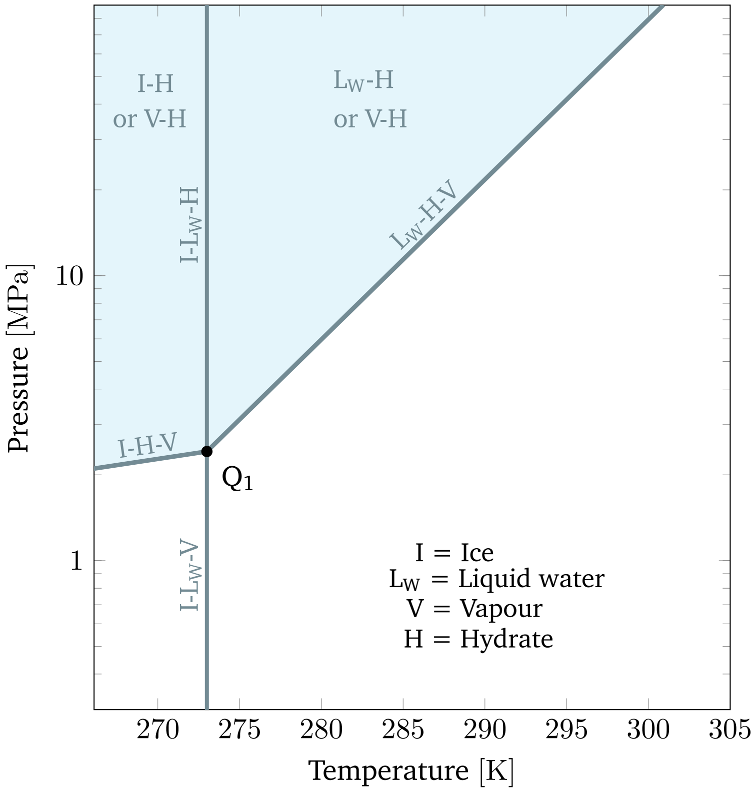

Fig. 2.2: Phase diagram of the water-methane system forming methane hydrate (from Sloan and Koh, 2007). The colored area represents the stability domain of methane hydrates.

Tab. 2.1: Parameters of the three-phase equilibrium expression (L_W-H-V and I-H-V) for pure methane hydrates (Kamath, 1984).

Equilibrium phases	a	b[K]	Range of T[K]
L_W-H-V	38.980	−8533.80	[273; 298]
I-H-V	14.717	−1886.79	[0; 273]

its diagram shows only one quadruple point, Q_1. Located in Fig. 2.2 there is a unique temperature and pressure to achieve the balance between the four phases I-L_W-H-V.

The equilibrium conditions of these systems have been experimentally established but correlation curves have been proposed by Kamath (1984) for the formation of simple hydrates of different species and for given temperature ranges. Kamath expresses the relationship of pressure as a function of temperature as:

$$P[\text{kPa}] = \exp\left(a + \frac{b}{T[\text{K}]}\right)$$

and the values of coefficients a and b are referenced in the table 2.1 for methane.

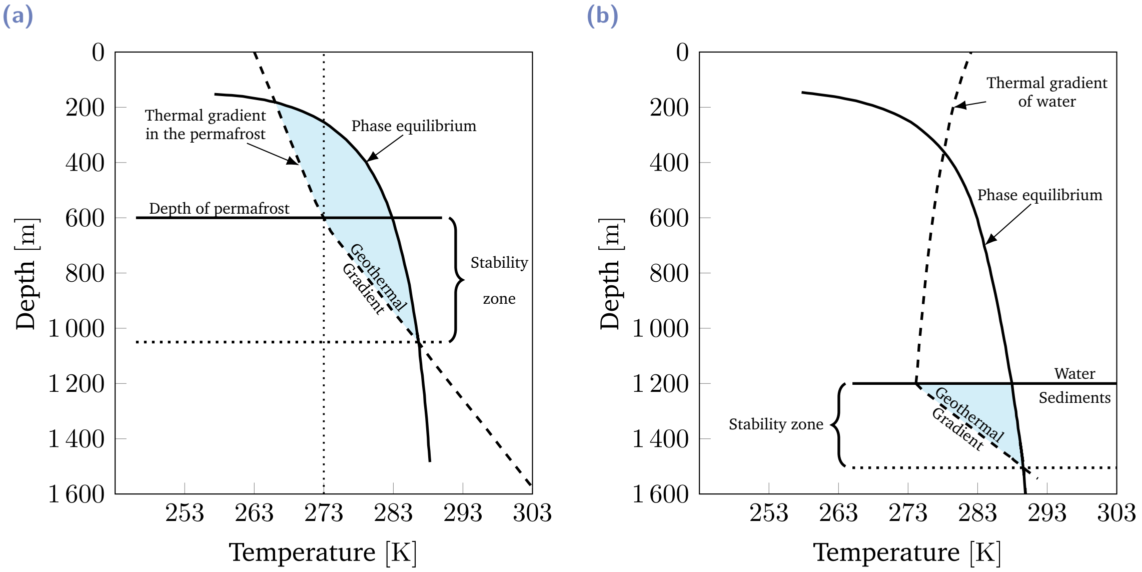

Fig. 2.3: Methane hydrate stability zones (a) in permafrost, (b) in marine sediments (from Kvenvolden, 1988).

The diagrams regularly used in the literature differ slightly from the one just described and focus only on the two equilibrium limits L_W-H-V and I-H-V but in the Depth-Temperature plane rather than in the Pressure-Temperature plane. This can be seen in Fig. 2.3, for greater clarity and connection with geology, the pressure is translated into depth (in metres). Fig. 2.3a shows this relation for permafrost regions and Fig. 2.3b for marine sediments. The geothermal gradient and the phase equilibrium line determines the upper and lower limits of the Hydrate Stability Zone (HSZ). It is in this area that gas hydrates can naturally occur.

It should be noted that the most common phase diagram represented in geophysics are for pure species systems. However, the phase diagram may change depending on the composition of the gas source forming the hydrates or on the presence of inhibiting compounds dissolved in water (such as sea salts) (Kvenvolden, 1993; Sloan and Koh, 2007). The gas can be a mixture of gases such as ethane, propane, or carbon dioxide in addition to methane. Conventional thermodynamic inhibitors of hydrate formation include salts, alcohols and glycols. These compounds have greater solubility in water and can create stronger bonds with water molecules, limiting or even inhibiting interactions between hydrocarbon and water molecules (Sloan and Koh, 2007).

2.1.4 Physical properties of gas hydrates

In addition to the geometry and composition of gas hydrates, their mechanical and thermal properties have also been studied. However, studies carried out in the laboratory remain quite difficult to exploit, especially in mechanics, given that the conditions of formation and the crystalline structures artificially formed can be very different from what is found in nature. The conditions of the existence of methane hydrates in ocean sediments, for example, are around tens of MPa and between $0\,^{\circ}\mathrm{C}$ and $10\,^{\circ}\mathrm{C}$ (Fig. 2.3). Accurately controlling such pressures and temperatures is not straightforward and require specific equipment.

Mechanical properties

There is little data available on the mechanical properties of pure gas hydrates (Ning et al., 2012). The study of compression and shear wave velocities has been widely used to estimate the elastic properties of gas hydrates in comparison to ice (see table 2.2). Creep tests have been conducted to determine the mechanical strength of methane hydrates, and the works of Durham et al. (2003b) and Durham et al. (2003a) suggest that they are less prone to creep than ice. These same tests have led to the observation that inelastic deformations of a pure methane hydrate polycrystal can lead to its partial dissociation, even if it is in the pressure-temperature stability domain of the hydrate.

Mechanical shearing tests of gas hydrates are quite rare and difficult to interpret due to the testing conditions. Hyodo et al. (2002), Yu et al. (2011b), and Stern et al. (1996) performed triaxial tests using high pressure and low temperature cells on samples synthesised from pure water and methane. The results obtained (Fig. 2.4) show a rather brittle behaviour of methane hydrate which could be compared to an elastic-perfectly plastic behaviour at first. Although the testing conditions, sample homogeneity and repeatability of these tests may be questionable, trends can be observed in the response and in particular for the resistance of methane hydrate. If we look at Fig. 2.5 we see that the higher the confining pressure and the lower the temperature, the greater the mechanical strength of the methane hydrate is for the same strain rate. Hyodo et al. (2002) also established that by increasing the strain rate the strength of the tested material tends to increase. Stern et al. (1996) conducted tests at very low temperature ($168\,\mathrm{K}$) and very high confining pressure ($100\,\mathrm{MPa}$) compared to the Hyodo et al. (2005) and Yu et al. (2011b) tests. Their results show a different rheology compared to ice under similar conditions and also a hardening of the material. The authors have also developed a new method for the synthesis of methane hydrates in the laboratory that will be used for tests on porous materials with hydrate inclusions (see section 2.3.1).

Regarding elastic properties, triaxial tests can provide an estimate of the Young's tangent modulus (Yu et al., 2011b) and the influence of different parameters on this modulus (Fig. 2.6). However, this gives us relatively little information, particularly regarding the isotropic or anisotropic nature of the material. Several studies have used compressional (V_P) and shear (V_S) wave velocities measurements to indirectly determine the values of bulk and shear moduli of pure methane hydrate samples (Sloan and Koh, 2007; Helgerud et al., 2003; Helgerud et al., 2009). If the measurements seem to be of the same order of

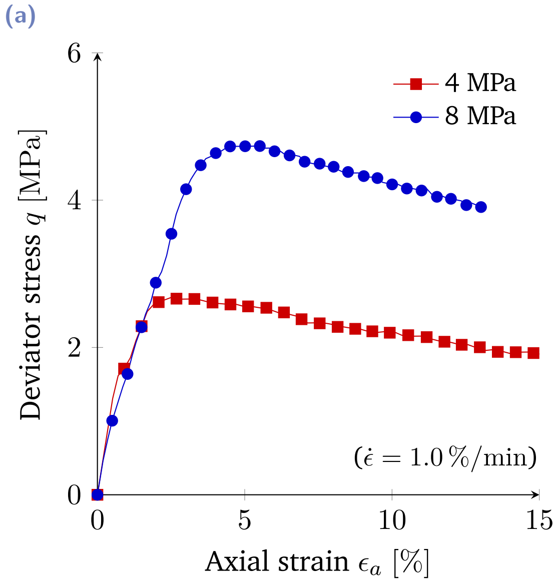

Fig. 2.4: Results of triaxial tests at -5 °C and different confining pressures on pure methane hydrate samples performed by (a) Hyodo et al. (2002) at a strain rate of 1.0 %/min and by Yu et al. (2011b) at 1.5 %/min.

magnitude overall, i. e. $3.7\,\mathrm{km\,s^{-1}}$ for V_P and $1.9\,\mathrm{km\,s^{-1}}$ for V_S (see Tab. 2.2), they should be considered with caution as they may have been performed at higher confining pressures than those observed for natural methane hydrates. For instance, Helgerud et al. (2003) obtained values of V_P and V_S for confining pressures ranging between $26\,\mathrm{MPa}$ and $62\,\mathrm{MPa}$.

Thermal properties

Like mechanical properties, the thermal properties of gas hydrates do not benefit from a large database, especially in the regards of heat capacity and dissociation enthalpy (Sloan and Koh, 2007). However, these properties have a significant influence on the energy behaviour of sediments rich in gas hydrates. As heat transfer plays an important role in hydrate formation/dissociation mechanisms, the very structure of sediments can be impacted by these properties (see Section 2.1.5).

Thermal conductivity evaluates the efficiency of an energy transfer caused by a temperature gradient in a material. Many studies have measured a thermal conductivity of hydrates on the order of $0.50\,\mathrm{W\,m^{-1}\,K^{-1}}$ (see Tab.2.2) which is much lower than that of ice, $2.23\,\mathrm{W\,m^{-1}\,K^{-1}}$ (Sloan and Koh, 2007; Waite et al., 2005). Fig. 2.7 from Gupta (2007) confirms this trend. However, thermal conductivity measurements of methane hydrates are difficult to obtain with certainty. The formation of methane hydrate samples is complex, so the samples are rarely homogeneous, and may have some intrinsic porosity and varying

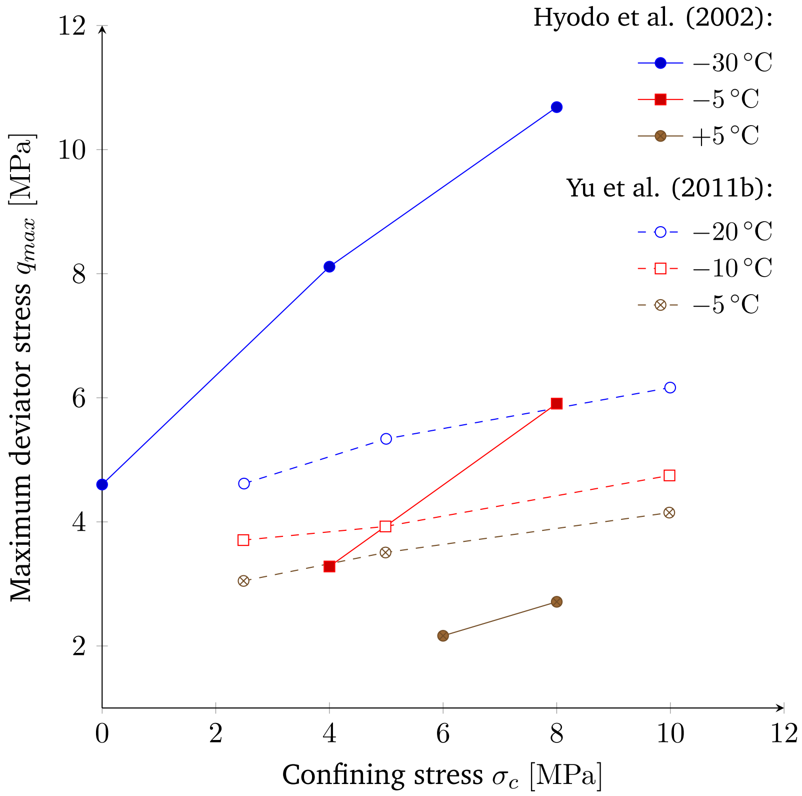

Fig. 2.5: Relationship between the confining stress and the maximum deviatoric stress for different triaxial tests performed at different temperatures on methane hydrate by Hyodo et al. (2002) at a strain rate of $1.0\,\%/\mathrm{min}$ and by Yu et al. (2011b) at $1.5\,\%/\mathrm{min}$.

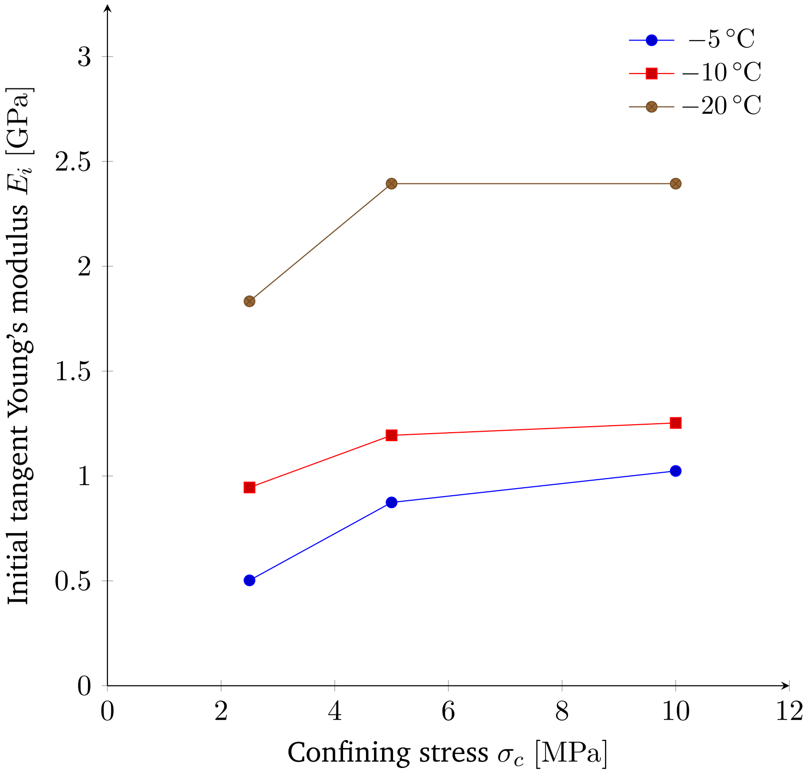

Fig. 2.6: Relationship between the confining stress and the initial tangent Young's modulus for different triaxial tests performed on methane hydrate by Yu et al. (2011b) at a strain rate of $1.5\,\%/\mathrm{min}$.

densities (Waite et al., 2005). This influences the observed thermal behaviour of synthetic methane hydrate samples. In addition, the thermal conductivity of methane hydrate and pure water are relatively close at the in situ temperatures of natural gas hydates sites(Waite et al., 2009).

Heat capacity is a measure of the amount of energy that must be supplied to a body to increase its temperature by one Kelvin, while the specific heat capacity represents the heat capacity relative to the mass of the body. The specific heat capacity of the methane hydrate was measured around $2075\,\mathrm{J\,kg^{-1}\,K^{-1}}$ (at $270\,\mathrm{K}$, Handa, 1986), half as much as pure liquid water, which can result in a decrease in the total heat capacity of gas hydrates bearing sediments (Waite et al., 2009).

Finally, the dissociation enthalpy corresponds to the energy that must be supplied to a gas hydrate in order for it to dissociate. Indeed, it is an endothermic reaction since the ordered structure of the hydrate has a lower internal energy than that of the reaction products (pure water and methane) which are in a freer state. While there are relatively few studies on the dissociation enthalpy of natural gas hydrates, Gupta et al. (2008) measure a relatively constant value for methane hydrate from $54.44\,\mathrm{kJ\,mol^{-1}} \pm 1.45\,\mathrm{kJ\,mol^{-1}}$ for a pressure range from $5.5\,\mathrm{MPa}$ to $19.3\,\mathrm{MPa}$ that corresponds to natural conditions. Gupta et al. (2008) also show that the Clapeyron equation provides a good prediction of their experimental

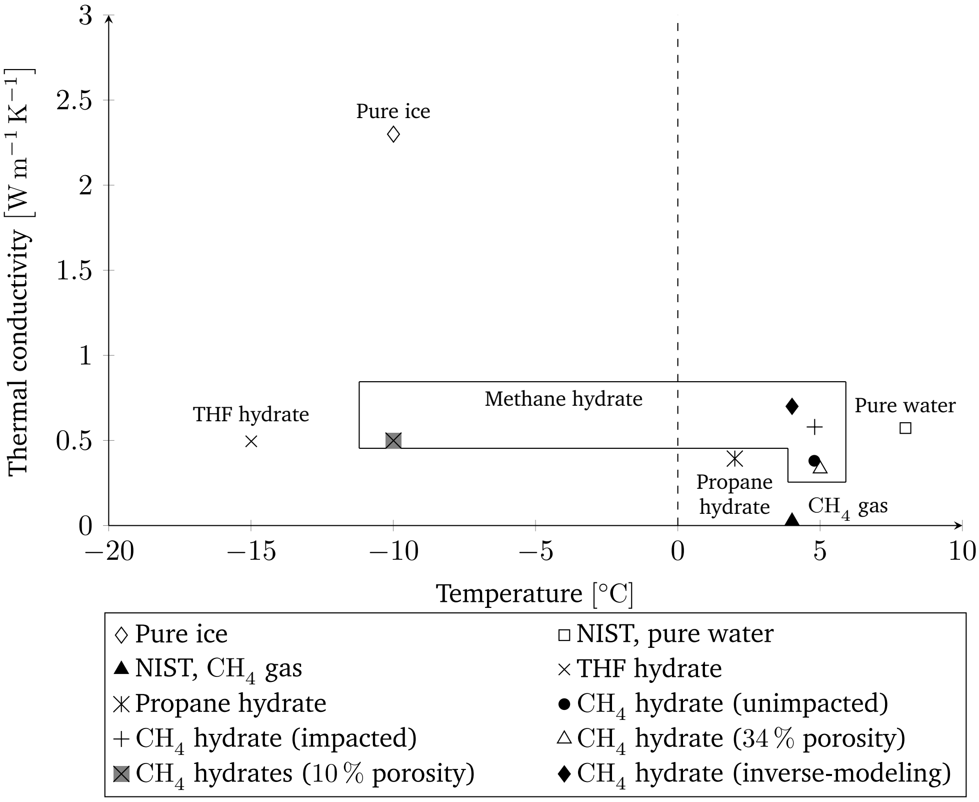

Fig. 2.7: Thermal conductivity of methane gas, water, ice and various gas hydrates (Gupta, 2007).

values, unlike the simplified Clausius-Clapeyron equation. In agreement with Gupta et al. (2008), Handa (1986) obtains a dissociation enthalpy of $54.19\,\mathrm{kJ\,mol^{-1}} \pm 0.28\,\mathrm{kJ\,mol^{-1}}$. It is worth noting that the invited molecule and hydrate structure influence the enthalpy value (Waite et al., 2009). Depending on the molecule and the type of structure (I, II or H), the size of hydrogen bonds increase and therefore the energy required to break them does as well.

Solubility

Methane, like other non-polar gases, has a very low solubility in pure water both before and after hydrate formation (Sloan and Koh, 2007). The presence of gas hydrates in marine environments is highly dependent on the concentration of dissolved gases in the liquid phase. This concentration must be higher than the solubility of the gas at seafloor pressure and temperature conditions in order to initiate hydrate formation and growth. Indeed, hydrates are essentially formed from methane in the aqueous phase (Buffett and Zatsepina, 2000; Sloan and Koh, 2007). However, the solubility of methane in water is much lower (on the order of 0.001 to 0.004 for the molar fraction of methane) than the amount of methane in hydrate (1 mole of methane for about 6 moles of water) under natural marine conditions (Sloan and Koh, 2007; Zatsepina and Buffett, 1998). Methane concentration is therefore a

Tab. 2.2: Mechanical and thermal properties of ice, and the structures I (sI) and II (sII) of methane hydrate (taken from Sloan and Koh, 2007).

Properties	Ice	sI	sII
Mechanical			
Poisson's ratio ν_H	0.3301	0.31403	0.31119
Bulk modulus K_H (GPa)	8.8 ; 9.097	5.6 ; 8.762	8.482
Shear modulus G_H (GPa)	3.9 ; 3.488	2.4 ; 3.574	3.6663
Compressional wave velocity V_P (m.s^{-1})	3870.1	3778	3821.8
Shear wave velocity V_S (m.s^{-1})	1949	1963.6	2001.14
Thermal			
Thermal conductivity k_H^T à 263 K (W.m^{-1}.K^{-1})	2.23	0.49± 0.02	0.51± 0.02
Specific heat capacity C_H (J.kg^{-1}.K^{-1})	1700±200	2080	2130±40

key element that controls the dissolution (dissociation) or precipitation (formation) rates of hydrates.

Several studies have investigated the effects of temperature, pressure and salinity of solutions on methane solubility, without hydrates and in the presence of hydrates at equilibrium between the two phases hydrate-liquid (Handa, 1990; Zatsepina and Buffett, 1998; Subramanian and Sloan, 2002). The studies in laboratory are limited by the conditions of hydrate stability, which are not without risks, and complicate measurements. The Raman spectroscopy method is therefore one of the most widely used in situ measurement methods because it does not disturb the system (Lu et al., 2008). It has been established that in the presence of hydrates, for a two-phase hydrate-liquid system, the solubility of methane decreases with decreasing temperature and increasing pressure (Subramanian and Sloan, 2002; Lu et al., 2008). The increase in salt concentration also leads to a decrease in methane solubility, which is part of the inhibitory role played by salts (Zatsepina and Buffett, 1998). In addition, the effect of the porous medium in marine sediments via capillary pressure in smaller pores also plays a role in the solubility of methane (Sun and Duan, 2007), but few studies exist on this subject.

2.1.5 Formation and dissociation of gas hydrates

As mentioned above, the understanding of the different geometric and physical characteristics of gas hydrates is strongly linked to their formation. Several studies have focused on the mechanisms of hydrate formation, growth and dissociation, and their time dependency. The formation or dissociation of these compounds in a sedimentary soil may have a significant environmental impact, which will be discussed in the next sections.

Formation

Three important phenomena in the life of hydrates should be considered: their nucleation, growth and dissociation (Sloan and Koh, 2007). Nucleation is a complex process found in other crystalline compounds, corresponding to the formation of the first hydrate crystals from pure species (water, hydrocarbon). In the case of the study of gas hydrate bearing sediments, hydrate is already formed and growth and dissociation processes play a major role. However, it is interesting to note that gas hydrate nucleation is a stochastic mechanism, generally occurring at an interface (liquid-gas for example, or solid-fluid), depending on many parameters such as the size and composition of the molecule included, the surface of reaction, or the history of water reactions (Sloan and Koh, 2007). Indeed, a known phenomenon occurring during hydrate formation is the "memory effect": the reformation of hydrates from species derived from a previous hydrate dissociation is faster than from species with no hydrate-related reaction.

Growth

The growth process is a little better controlled (Sloan and Koh, 2007). Like nucleation, hydrate growth is an exothermic phenomenon. It has also been observed that for multi-phase systems, the effects of mass transfer of components and heat released by the reaction prevail over the kinetic effects during hydrate crystal growth (Sloan and Koh, 2007). Therefore, several approaches can be considered for modelling the formation and growth of gas hydrates, with kinetic models being of less importance than mass or heat transfer models (Sloan and Koh, 2007).

Dissociation

Hydrate dissociation is certainly the most important concern for hydrates naturally present in oceanic sediments and permafrost. This phenomenon is endothermic, unlike the hydrate formation reaction, and three possible methods exist to dissociate these compounds: depressurisation, heating or adding an inhibitor. As with growth, kinetic effects are dominated by heat transfer, which seem to most often govern the dissociation process (Sloan and Koh, 2007). In addition, a "self-preservation" phenomenon has been observed (Stern et al., 2003), which manifests itself in a stabilisation of methane hydrates and a strong slowdown of the reaction during dissociation at atmospheric pressure and at temperatures of 242-271 K, but this phenomenon has not been explained yet.

2.2 Natural gas hydrates

2.2.1 Formation and origins

The discovery of the natural formation of gas hydrates in geological layers is recent. Exploration of natural gas hydrate sites began in the 1960s with the Soviet discovery and exploitation of the Messoyakha field in permafrost, where nearly one-third of the gas extracted came from gas hydrates (Sloan and Koh, 2007). Subsequently, research and investigations have led to the establishment of cartography of the global distribution of this resource (Fig. 2.9). These same projects have greatly contributed to the development of research, and exploration techniques in particular, on natural gas hydrates. Indeed, hydrates are found in the shallow ocean sedimentary layers (a few hundred metres) at several hundred or even thousands of metres underwater, or in permafrost, where the conditions of low temperatures and high pressures conducive to their formation are met (Fig. 2.3). This is why they are most often found at continental margins and sea troughs near subduction zones. But pressure-temperature conditions are not the only criterion and other factors are necessary to their development in these regions that justify the presence of hydrates: a massive influx of organic carbon and very high sedimentation rates (Sloan and Koh, 2007).

Gas hydrates that form naturally are generally limited by the supply of natural gas. Two sources are therefore possible:

- the biogenic gas resulting from the degradation of organic matter present in sedimentary layers by methanogenic microorganisms,
- thermogenic gas resulting from the decomposition of organic matter at greater depths by heat and pressure.

Biogenic gas is formed directly in the sedimentary environment at lower temperatures and slower rates, while thermogenic gas moves up to the hydrate stability zone through fractures with faster rates. This explains the association between gas hydrates and free gas at some sites, and why the oil industry uses the presence of gas hydrate layers for its prospection of heavier hydrocarbons in the underlying layers, among other things (Collett, 2002). The search for gas hydrate deposits therefore requires knowledge of the geology of a region, the position of faults, the existence of permeable and impermeable layers that can serve either as a channel for the rise of gases or as a ceiling for the natural blocking of potential reservoirs. Natural gas hydrates are essentially made up of methane with a mixture of heavier hydrocarbons in lesser quantities. The origin of natural gas forming hydrates can be determined by studying the isotopes that compose it and the knowledge of biogenic gas having a higher ratio of methane to other hydrocarbons compared to the thermogenic gas (Claypool and Kvenvolden, 1983).

The type of gas, like the type of soil, plays a role in the formation and morphology of natural gas hydrates. The latter will develop according to the circulation of fluids in the porous space of the sediments in place, which is why the porosity and permeability of the soil matrix plays a significant role (Malagar et al., 2019). Indeed, the observation of cores from several gas hydrates sites showed a great diversity in the development patterns of hydrates according to the characteristics of the soil such as: permeability, granulometry, pore size, but also the gas source. We therefore can have soils where gas hydrates are homogeneously distributed in a relatively granular soil matrix, we can have lenses or hydrate nodules formed in more fine-grained soil layers, or we can even obtain pure hydrate blocks over a certain thickness. In addition to the structural changes made by these hydrate inclusions, there are changes in the geophysical properties of soils due to their presence. It is from these variations in properties that exploration methods have been developed and that we can determine the Bottom-Simulating Reflector (BSR). This is a variation of impedance between two layers that corresponds to the base of the hydrate stability zone and is most often parallel to the seabed, and it is one of the first characteristics that is used for the detection of natural gas hydrates (Collett, 2002; Sloan and Koh, 2007).

2.2.2 Structure and pore occupancy

The data from Masui et al. (2005) and Ebinuma et al. (2005) show differences between natural samples and those synthesised in the laboratory. The authors, in agreement with all researchers in the field (Soga et al., 2006; Waite et al., 2009), explain these differences of behaviour by the fact that there are different types of hydrate distribution in the sediments. The way in which hydrates form, whether naturally or artificially, determines their position in the pores of the sedimentary matrix and therefore the nature of contact between grains and hydrates. This pore occupancy pattern or "pore habit" obviously plays a role in the macroscopic behaviour of soils.

Natural gas hydrates are known to be mainly distributed in large volumes of clayey sediments with relatively low permeability (Fig. 2.8) They can form differently in these soils, either by homogeneously filling the pores or by destructuring the matrix and forming veins and nodules (Fig. 2.8). The low permeability explains these formation patterns, as the fluids have to pass through the clay matrix, and this results in relatively small average volume fractions of hydrates in the pores, generally less than $10\,\%$ for homogeneous distributions. Granular soils represent a smaller volume compared to these clayey deposits around the globe, but they have a larger average volume fraction of hydrates, between $50\,\%$ and $90\,\%$ of the pore volume, and have more interesting characteristics for gas recovery (Boswell et al., 2014).

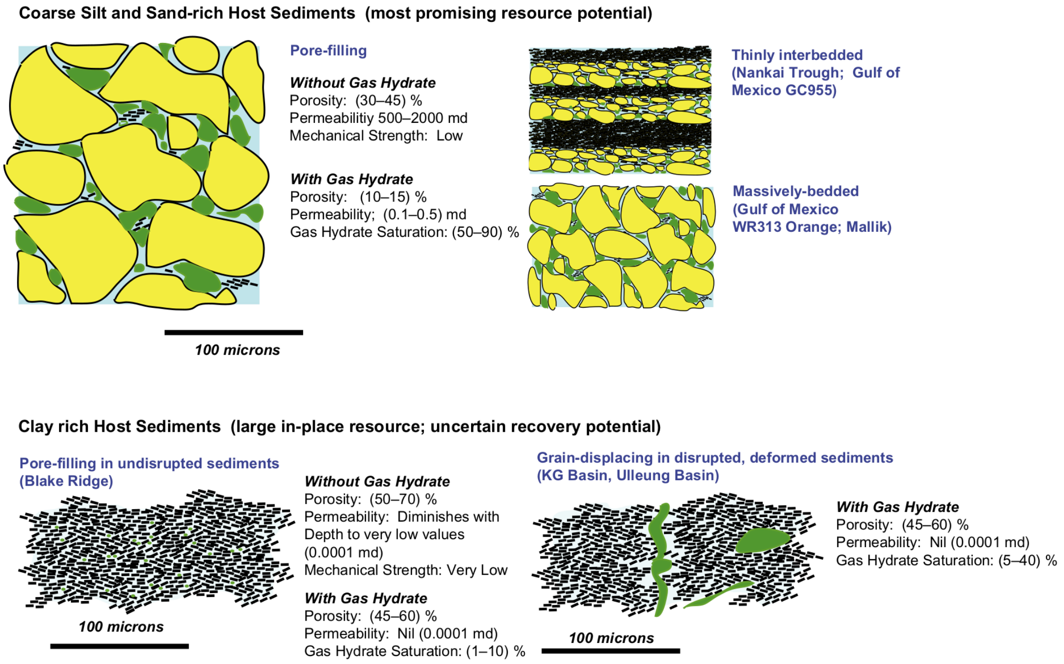

Fig. 2.8: Contrasts between gas hydrate bearing sands (top) and gas hydrate bearing clays (below) in nature (from Boswell et al., 2014).

For granular sediments, Waite et al. (2009) define three types of pore habits in the sedimentary matrix, which are commonly used in the literature:

- Pore-filling: Hydrates are present inside the pores and are free to move in the pore water. This generally corresponds to low hydrate saturations and granular soils.
- Load-bearing: as in the first case, the hydrates are in the interstitial space, but this time they are in contact between two or more grains. They are therefore part of the solid phase of the soil and can transmit forces.
- Cementing hydrates are in contact with the grains but are binding agents: they have a cementation effect between the grains, which makes the soil much stronger and more cohesive.

In reality, gas hydrates can be present in different forms among the three previous ones in the same solid matrix. Several studies have focused on observing the microstructure of these composite soils by imaging techniques (Chaouachi et al., 2015; Zhao et al., 2015; Bagherzadeh et al., 2011) in order to more accurately characterise the morphology of hydrates and how they develop in pores. These studies have mainly been based on the use of granular soils up to now, since it is difficult to synthesise hydrates in fine soils. Laboratory imaging techniques pose many practical problems simply because the stability conditions required for hydrates are far from standard conditions. In addition, in the case of X-ray tomography observations, for example, in soils with methane hydrate inclusions, data processing is delicate as the density of methane hydrate is close to that of water and ice. The solution is often to choose a gas different from methane such as xenon (Chaouachi et al., 2015; Chaouachi, 2015). However, natural samples have been observed particularly in fine sediments, most often at relatively low resolution levels or even after hydrate dissociation (Rees et al., 2011).

2.2.3 Exploration and energy resource

The different formation mechanisms of hydrates in natural sediments are still a subject of discussion today. This is why the exploration of natural gas hydrates around the globe has increased significantly with the development of national projects such as the National Science Foundation's Deep Sea Drilling Project (DSDP) in the United States, a seabed exploration programme conducted from 1968 to 1983, followed by the international Ocean Drilling Program (ODP) from 1985 to 2003, finally transformed into the current Integrated Ocean Drilling Program (IODP) in 2004. Canada has funded gas hydrate research with the Geological Survey of Canada for several years, carrying out several gas production tests in the Mackenzie Delta of the Arctic permafrost region in partnership with Japan and other countries. After the discovery of gas hydrates in the sedimentary layers of the Nankai Trough, Japan launched one of the very first research and development projects on methane hydrates in 2001; the MH 21 Research Consortium. The aim of this project is to develop technologies and the production of natural gas from hydrates in order to guarantee a clean resource for the country which currently imports $80\,\%$ of its energy (Oyama and Masutani, 2017). Two offshore production trials were conducted at the Nankai Trough in 2013 and 2017. India also launched the National Gas Hydrate Program (NGHP) in 1997 to assess the country's ocean gas hydrate energy resource. Other countries such as China and South Korea have initiated exploration programs, with China even conducting its first offshore production trial in 2017 (Li et al., 2018). Some of the main natural gas hydrate exploration sites include: Mallik (Canada, permafrost) in the Mackenzie River Delta, Joint Industry Project Legs I and II (JIP, USA, ocean sediments) in the Gulf of Mexico and Nankai Trough (Japan, ocean sediments). They are represented along with other major sites in Fig. 2.9.

As gas hydrate exploration around the globe progresses, scientists have attempted to estimate the exact amount of this natural gas resource based on the following characteristics: surface area of the hydrate zone, thickness of the hydrate layer, average porosity of the layer, average pore volume fraction occupied by the hydrates and hydration number of hydrates present in the area. While the figures may vary by up to three orders of magnitude from one publication to another, the results of these estimates tends to decrease over time while the minimum order of magnitude remains $1 \times 10^{15}\,\mathrm{m}^3$, even with the most conservative calculation methods (Fig. 2.10). To date, it should be noted that more than $90\,\%$ of this resource has been located at sea with the remainder at the permafrost level (Collett et al., 2015; Makogon, 2010).

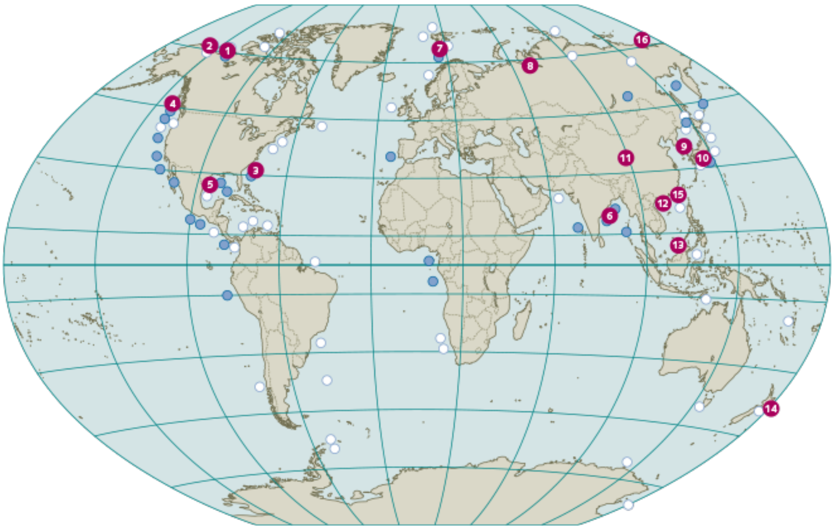

Fig. 2.9: Worldwide distribution of the main natural gas hydrate sites. The white dots represent sites for which the presence of gas hydrates has been suggested by geophysical data, and the blue dots represent those for which it has been attested (taken from Jan Lehmköster et al. (2014), from U.S. Department of Energy).
1 MALLIK (Canada, permafrost); 2 NORTH SLOPE (Alaska, United States, permafrost), Mount Elbert; 3 BLAKE RIDGE (United States, ocean); 4 CASCADIA CONTINENTAL MARGIN (United States and Canada, ocean); 5 GULF OF MEXICO (United States, ocean); 6 KRISHNA GODAVARI BASIN (India, ocean); 7 SVALBARD (Norway,ocean); 8 MESSOYAKHA (Siberia, Russia, permafrost); 9 ULLEUNG BASIN (South Korea, ocean); 10 NANKAI TROUGH (Japan, ocean); 11 QILIAN MOUNTAINS (China, permafrost); 12 SHENHU BASIN (China, ocaan); 13 GUMUSUT-KAKAP (Malaysia, ocean); 14 NEW-ZEALAND (New-Zealand, ocean); 15 TAIWAN (Taiwan, ocean); 16 SIBERIAN SHELF (Siberia, Russia, permafrost)

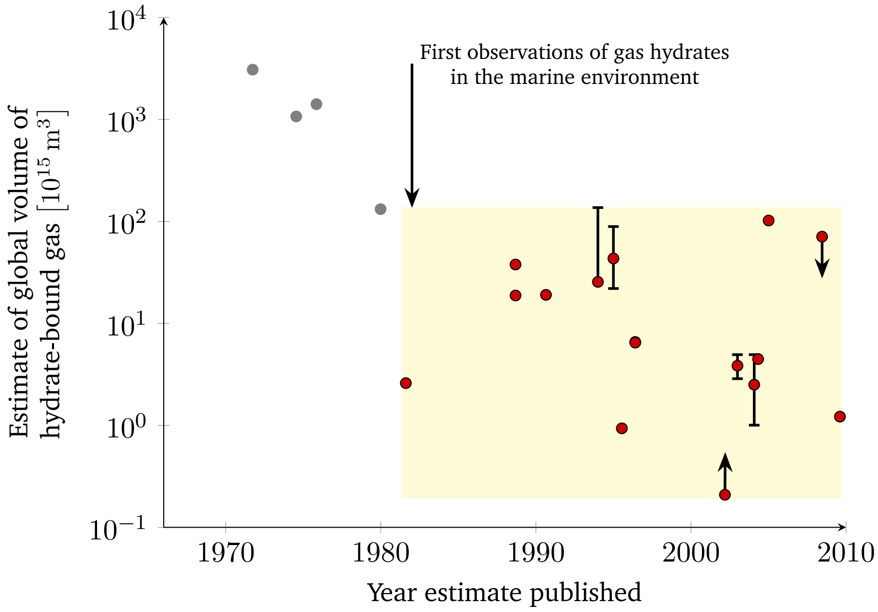

Fig. 2.10: Evolution of published estimates of the global volume of natural gas contained in gas hydrates (Boswell and Collett, 2011).

Research has expanded beyond the scientific aspect in recent years, moving towards a more in-depth study of the feasibility and performance of future gas hydrate exploitation. Three main methods are possible to dissociate the gas hydrates and recover methane gas from it: either by thermal stimulation or depressurisation or by injection of inhibitors. Likewise carbon dioxide injections are also being considered. In this process, methane would be substituted by carbon dioxyde as the guest phase in hydrates, thus reducing the impact of methane production from hydrates in terms of greenhouse gas emissions. Nevertheless, it should be borne in mind that current experiments involving gas hydrates, whether at the level of boreholes, operating level and also in gas pipelines show that serious incidents can occur if these compounds are not controlled (Sloan and Koh, 2007).

2.2.4 Environmental risks

The environmental impact of gas recovery is also to be considered in the event that the industry begins to exploit hydrates. With methane being a greenhouse gas, hydrates could still play a role in climate change that is difficult to correctly assess according to some scientists (Glasby, 2003; Archer, 2007; Maslin et al., 2010). In particular, there is a theory (Kennett et al., 2003) according to which methane gas released by hydrates would have been at the origin of a significant global warming at the end of the Quaternary period. Several research projects have been launched in recent years in parallel with environmental research on gas recovery technologies in order to assess the viability of these natural resources. However, concern is not limited to global warming; considerable landslides on the seabed are associated with hydrates. Several researchers have described such past events as having been triggered by the dissociation of hydrates (Kayen and Lee, 1991; Macdonald et al., 1994; Sultan et al., 2004a; Sultan et al., 2004b). But the risk could also concern the structural foundations linked to current oil activities, for example (Briaud and Chaouch, 1997). It is therefore becoming imperative to be able to predict the behaviour of gas hydrate bearing sediments, and recent publications are addressing this issue.

2.3 Properties of gas hydrate bearing soils

2.3.1 Experimental methods

Several investigation and characterisation methods have emerged with the development of research on natural gas hydrates. They can be divided into three main categories: indirect or remote measurement techniques, in situ exploration methods, and laboratory tests. It is important to understand the scope and limitations of these techniques in order to better understand all the experimental data acquired to date concerning the behaviour of sediments containing gas hydrates and the issues related to their modelling.

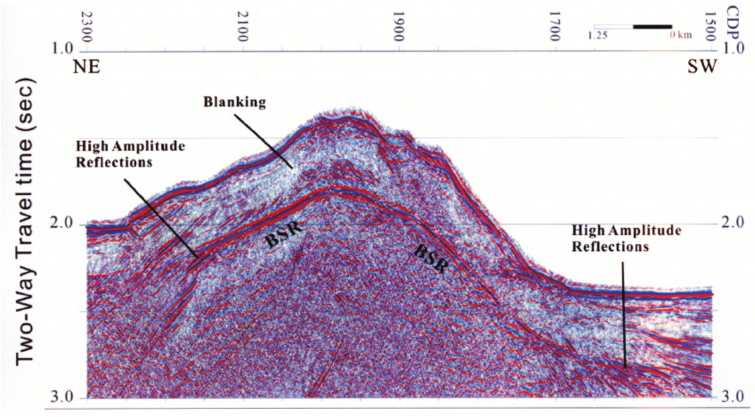

Fig. 2.11: Example of BSR (Bottom Simulating Reflector) logged at sea off the Taiwan coast (Liu et al., 2006).

Remote analysis methods have been developed for investigations at sea where hydrate-rich layers are surmounted by several hundreds or even thousands of metres of water. The measurements are based on the detection of changes in the electrical, chemical or seismic properties of the soil due to the presence of gas hydrates (Weitemeyer et al., 2006). In particular, seismic reflection methods detect the BSR (Fig. 2.11), a result of an impedance variation that may be due to the presence of free gas just below the hydrate stability zone (Sloan and Koh, 2007; Pecher et al., 1998). As these techniques are relatively inexpensive, they have led to major advances in the identification of sites containing gas hydrates. However, their accuracy is rather low, the presence of a BSR can be linked to other types of compounds than hydrates and for some natural hydrate bearing sites such as in the Gulf of Mexico, only anomalies have been detected. This is very different from the classical BSR (Pecher et al., 1998; Shedd et al., 2012). In situ measurements are therefore becoming essential in the exploration of hydrate-bearing soils and the characterisation of their physical properties.

In situ exploration tests and techniques have been developed over the past twenty years. Offshore exploratory drilling, coring and penetrometer tests have produced more tangible and usable data for the scientific community (Taleb et al., 2018). However, sediment samples naturally containing gas hydrates are difficult to recover due to hydrates instability under atmospheric pressure and ambient temperature conditions. In conventional coring, samples are depressurised and heated, triggering the dissociation process before they even reach the surface. Recent pressure cores have addressed these problems and allowed the recovery of sediment cores containing hydrates without major disturbances or changes in in situ conditions (Santamarina et al., 2012). Several tests could then be carried out while keeping these samples intact. Nevertheless, the resources and costs of these tests are still quite high today, and are only within the reach of a very small number of research teams. Moreover, it is not possible to completely avoid the disturbance of samples and changes in the in situ conditions even with pressure coring. Among other things, in clayey sediment layers such as the Krishna-Godavari Basin sampling is similar to undrained loading conditions due to the low permeability of the layers and can lead to a reduction in pore pressure and therefore a dissociation of the hydrates in place (Dai and Santamarina, 2014).

Laboratories are therefore forced to develop procedures to synthesise the samples and also to carry out the tests under pressure and temperature conditions that are as close as possible to in situ conditions at the seabed (Winters et al., 1999; Masui et al., 2005; Hyodo et al., 2005; Miyazaki et al., 2008). The tests performed are mainly triaxial compression tests allowing the strength of the samples to be studied, or wave velocity measurements to determine their composition and elastic mechanical properties (Guerin et al., 1999). It should be noted that the synthesis of soil samples containing gas hydrates requires a lot of work. In order to obtain the most reliable test results the formation conditions but also the characteristics of the soil matrix used in the laboratory play a crucial role. In addition, the pore occupancy patterns of gas hydrates are sensitive to the formation conditions (Malagar et al., 2019), and can significantly modify the results obtained (Masui et al., 2005; Ebinuma et al., 2005). While few researchers were able to test natural samples from coring, such as Winters et al. (1999) with samples from the Mallik 2L-38 well (Mackenzie Delta, permafrost) or Masui et al. (2006) and Yoneda et al. (2015) with cores from the Nankai Trough, most of the tests that exist in the literature have been conducted on artificial samples. The preservation of hydrates in sediments during the transport of cores is delicate, but it is possible to study the different types of sediments that host them. Based in particular on their grain size, laboratories that synthesise samples of gas hydrate bearing soils can choose a soil matrix that is closest to that of the seabed (Fig. 2.12). Japanese researchers, for example, mainly use Toyoura sand for their tests (Masui et al., 2005; Miyazaki et al., 2011; Hyodo et al., 2013) with a particle size distribution comparable to the one of Nankai Trough sandy sediments. The devices used generally consist of a high-pressure cell (up to 30 MPa for Hyodo et al., 2013) placed inside an external temperature-controlled cell (Fig. 2.13).

Methane hydrate is assumed to form naturally by the reaction in the aqueous phase between dissolved gas and water saturating ocean sediments and the influx of natural gas not being sufficient to enable free gas to be present (Buffett and Zatsepina, 2000). It is however difficult to reproduce this reaction within a reasonable time in the laboratory due to the very low solubility of methane in water, which is why current methods of synthesis have been based on the use of excess free gas methane, reacting more quickly with water in porous media. The protocols for making hydrates and synthetic samples used by researchers have evolved in recent years, and two techniques are most often used.

The first protocol is the excess gas method in a porous medium partially saturated with water (Waite et al., 2004; Winters et al., 2004). The method consists in preparing a soil sample with a given porosity and water content. The method differs from one author to another as seen in the protocols followed by Clayton et al. (2005), and Miyazaki et al. (2008). After methane gas is percolated under a pressure of 8 to 12 MPa in the sample placed into the internal triaxial cell. Once the methane flows through the sample, it is placed under

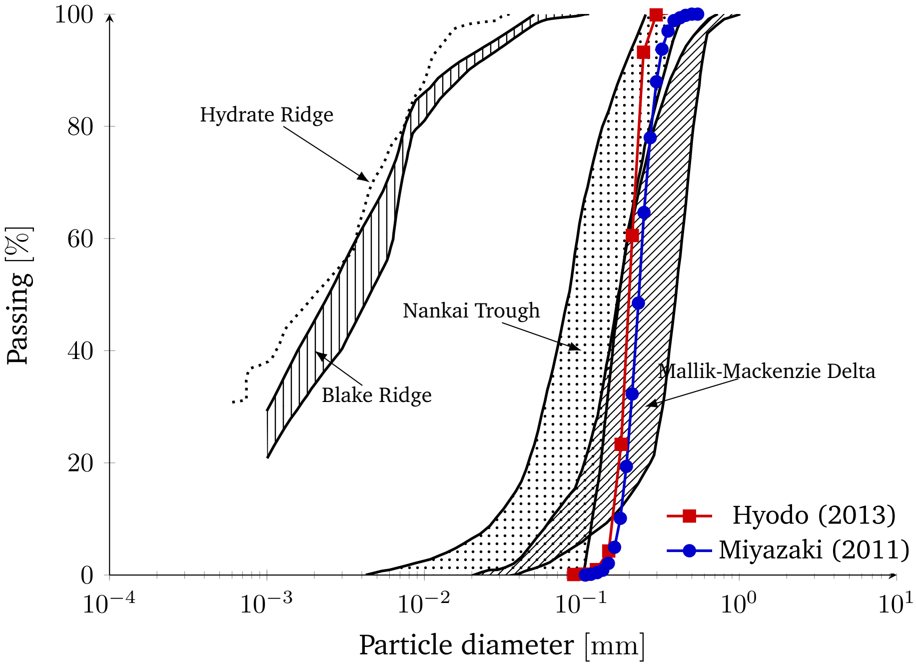

Fig. 2.12: Particle size distribution of different sediments from exploration sites containing gas hydrates (from Soga et al., 2006).

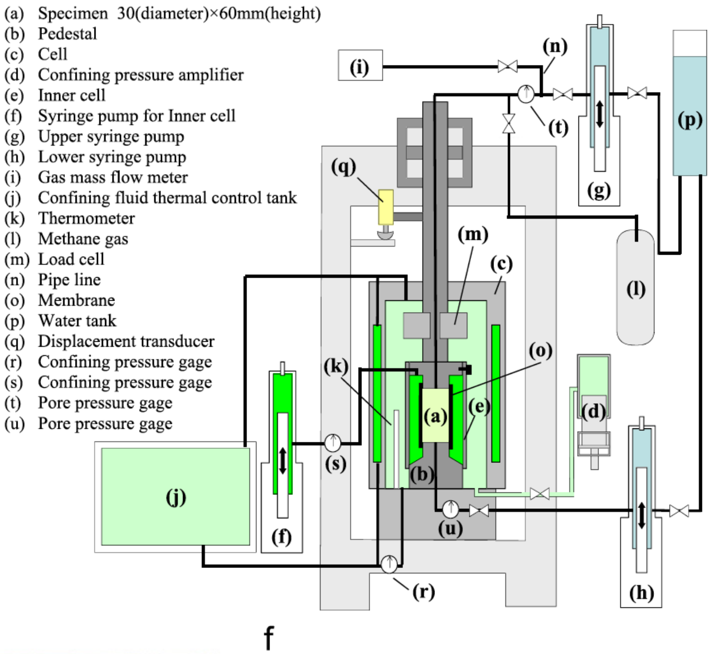

Fig. 2.13: Apparatus schematic for testing samples with gas hydrates (from Hyodo et al., 2013).

conditions conducive to hydrate formation such as increased confining pressure, and/or lower cell temperatures. Finally, in the excess gas method, the non reacting gas can be flushed away by circulating water in the sample. In some tests (Hyodo et al., 2013) authors saturate the pores of the sample free from hydrates with water, and in others (Clayton et al., 2005) a gas pressure is maintained after hydrate formation, the pores being filled with hydrates, gas and sometimes water.

Then there is "ice-seeding" method, pioneered by Stern et al. (1998). This consists of forming methane hydrates by reaction between pressurised free gas and ice. This is achieved by injecting methane under pressure into a mixture of sieved ice aggregates (obtained by crushing ice) and soil at a temperature below $0\,^{\circ}\mathrm{C}$. The temperature is increased to melt the ice while maintaining sufficient pressure to remain in the hydrate formation domain. Once the reaction is complete, the sample is then cooled to the desired temperature. Several studies have used this technique to compare its effects with those of the previous method on the properties of the resulting samples (Masui et al., 2005; Ebinuma et al., 2005).

Other methods exist, including the dissolved gas method, which remains the closest to the way gas hydrates are formed in natural reservoirs. Here, water with the dissolved hydrocarbon gas circulates through the pores of the sample at the pressure and temperature required for the hydrate formation reaction. Unfortunately, the formation times are very long in the case of methane, particularly because of its very low solubility in water. Therefore, existing studies using this synthesis method use carbon dioxide instead (Zatsepina and Buffett, 2001).

2.3.2 Mechanical properties

The physical properties of sediments containing gas hydrates must be studied in order to model their behaviour and to predict possible mechanical failures during their exploitation. In addition, the known couplings between the mechanical, hydraulic and thermal properties of soils require the study of the mechanical characteristics of gas hydrate bearing sediments also for their impact on the gas recovery efficiency, and for a more reliable estimation of the performance of existing reservoirs. This has led to numerous publications of experimental tests such as those mentioned above. The majority of these tests have been conducted on granular soils, and at present it is difficult to find tests on fine soils (Waite et al., 2009). This is mainly due to the lower interest in exploiting hydrate reservoirs in this type of soil and the difficulty of forming hydrates in this environment because formation times are very long. The low permeability limits fluid circulation and therefore limits the reaction surfaces (Malagar et al., 2019; Waite et al., 2009). However, some authors have published results of tests on fine soils with inclusions of THF hydrates synthesised in the laboratory (Yun et al., 2007; Santamarina and Ruppel, 2008), THF hydrate being miscible in water and being formed under less extreme conditions than methane hydrate. Still others (Yu et al., 2011a) were able to form and test methane hydrates in clays in the laboratory, using the crushed ice method.

To date, different types of mechanical tests have been carried out on granular soils with methane hydrate inclusions, of natural or synthetic origin:

- resonant column tests (Clayton et al., 2005),
- triaxial shear tests under drained conditions (Masui et al., 2005; Masui et al., 2006; Ebinuma et al., 2005; Miyazaki et al., 2011; Hyodo et al., 2013; Yoneda et al., 2015),
- triaxial shear tests under undrained conditions (Winters et al., 1999; Winters et al., 2002; Zhang et al., 2012; Ghiassian and Grozic, 2013),
- plane strain compression tests (Yoneda et al., 2013; Kato et al., 2016).

Measurements of compression and shear wave propagation rates are sometimes coupled with the last three of these tests with several objectives: to confirm the presence of hydrate inclusions in the sample, to monitor the formation of hydrates during their synthesis in the laboratory, and to study the elastic parameters of these composite soils.

Granular soils:

All studies show that methane hydrates have a significant impact on granular sediments. The drained triaxial test curves obtained show elastoplastic behaviour with rigidity, strength and dilating tendencies that evolve according to the volume fraction of methane hydrates occupying the pores commonly referred to as methane hydrate saturation and noted as S_H of the samples (Fig. 2.14). These tests made it possible to observe that the presence of hydrates in a soil led to an dilatant volumetric behaviour and a strain hardening phenomenon with occasional strain softening after the peak deviator stress (Fig. 2.14). The fact that for the same conditions of realisation the results vary from one study to another is that the test conditions and the microstructure of the sample play a major role in the mechanical response. It can nevertheless be noted that for the same study (Masui et al., 2006) samples containing methane hydrates have a higher strength, rigidity and dilatancy than the same soils without hydrates. The same trends can be observed for the results of undrained triaxial tests (Fig. 2.15) and in plane strain.

The pore volume fraction occupied by gas hydrates S_H quickly appears as an influential parameter. In particular, it was found that the more significant this parameter is, the more

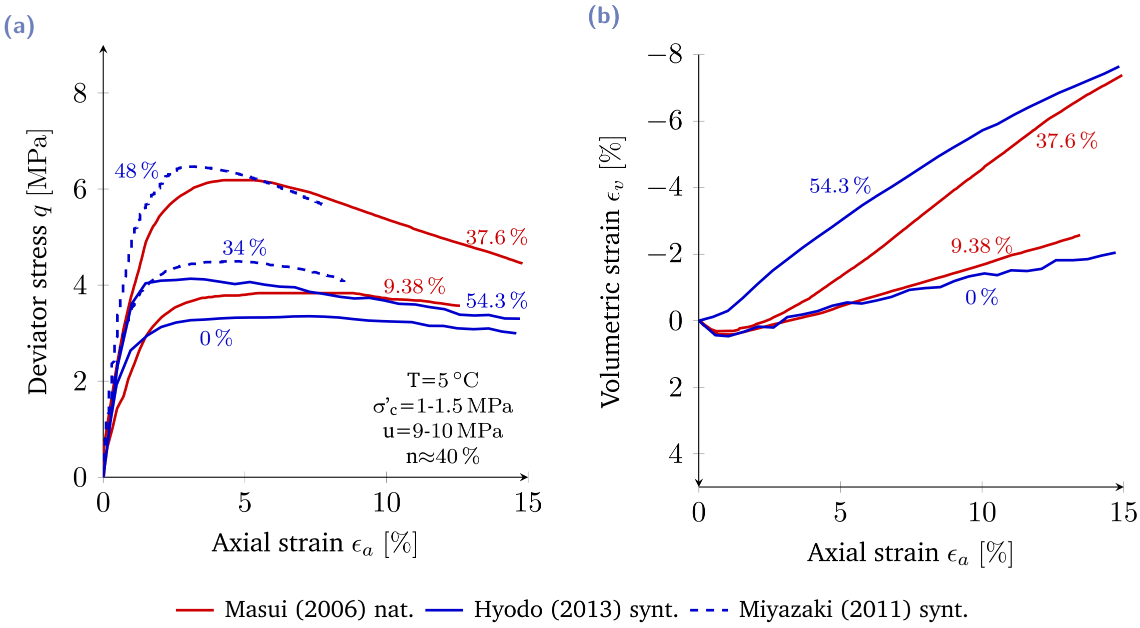

Fig. 2.14: Results of drained triaxial tests on natural and synthetic samples containing different volume fractions of hydrates in the pores. In red are the results on natural samples, and in blue on synthetic samples.

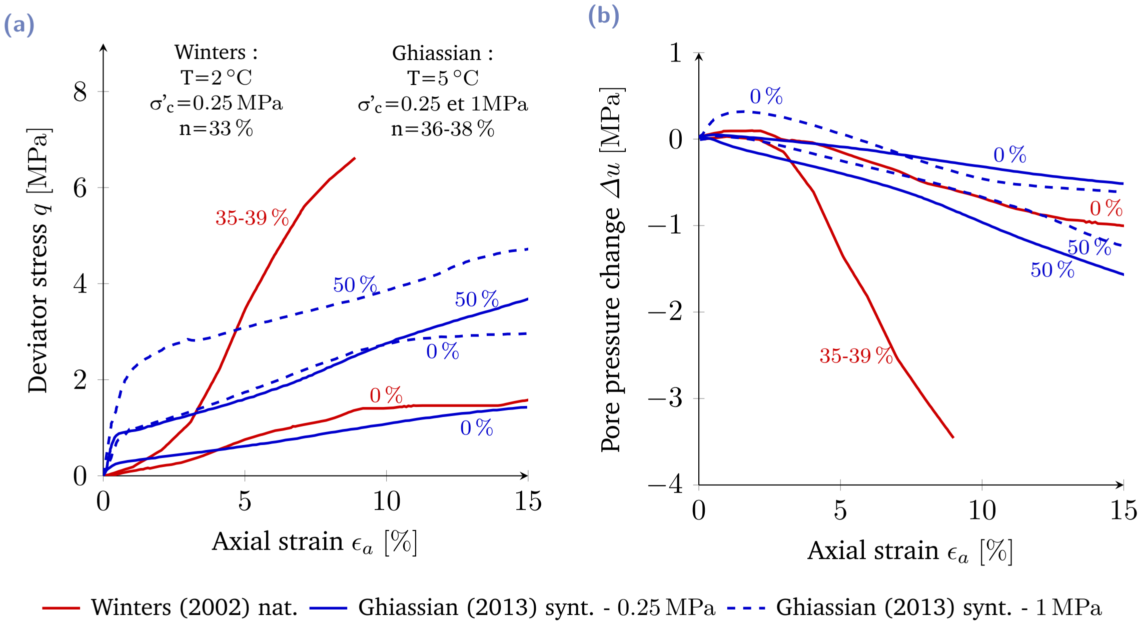

Fig. 2.15: Results of undrained triaxial tests on natural and synthetic samples containing different volume fractions of hydrates in the pores. In red are the results on natural samples, and in blue on synthetic samples. Ghiassian and Grozic (2013) saturated their samples with gas, whereas Winters et al. (2002) used water.

the Young's modulus, cohesion, and dilatance of the material increase. However, the effect of this amount of hydrates on the friction angle and the Poisson's ratio remains rather unclear.

On the other hand, the heterogeneous structure of the gas hydrate bearing soils gives rise to various couplings and makes it more complex to study the parameters influencing their response from a mechanical point of view alone. This is why some authors have investigated the effect of other parameters than S_H such as:

- the effective confining pressure,
- the temperature,
- the strain rates,
- the properties of the soil (grain size, percentage of fines added),
- the pore habits of hydrates (cementing of grains or pore filling).

Just as for pure hydrates, it was thus highlighted that the greater the confining stress, the greater the strength is for the same gas hydrates saturation in the samples (Fig. 2.16). Similarly, Hyodo et al. (2013) recorded a difference in the shear response of samples of the same gas hydrate saturation and porosity but subjected to different test temperatures (Fig. 2.17) consistent with the results obtained for pure hydrates. Fig. 2.17 shows that samples subjected to lower temperatures have increased stiffness, strength and dilatancy. Finally, some authors such as Masui et al. (2005) and Ebinuma et al. (2005) have focused on synthesising different types of hydrates, i.e. hydrates occupying the porous space in different ways either by cementing grains, or by filling the pores. The comparative results between the two methods of hydrate synthesis in the sheared samples from triaxial drained tests showed that the hydrate pore occupancy pattern also had a significant effect on soil mechanical response (Fig. 2.18). In Fig. 2.18 the weak and strong bonding terms refer to the bonding between methane hydrates and sand particles induced by the ice-seeding and the excess gas synthesis methods respectively.

Fine soils:

The number of laboratory studies on the synthesis of methane hydrates in fine soils is very limited. The main knowledge of the mechanical behaviour of these soils in the presence of gas hydrate inclusions is based on tests carried out on samples with THF hydrates (Yun et al., 2007). The effects of THF hydrates on these fine soil samples are similar to the previous

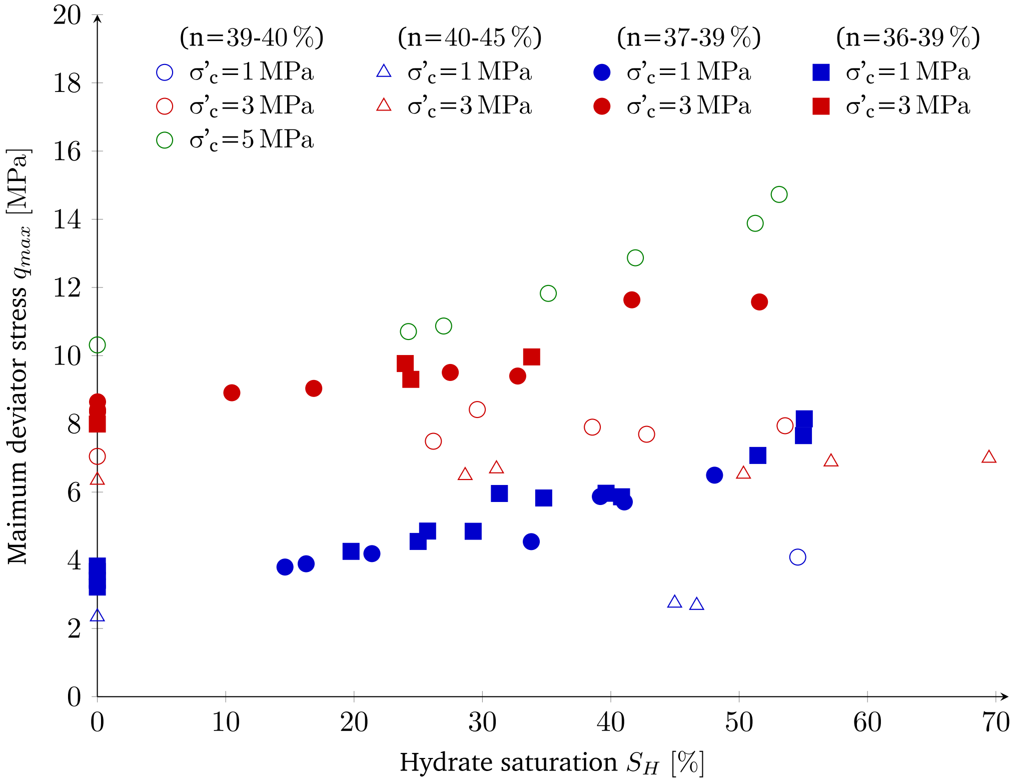

Fig. 2.16: Effect of hydrate saturation S_H and confining pressure (1 MPa, 3 MPa and 5 MPa), at fixed temperature (5 °C), on the strength of Toyoura sand samples with methane hydrates at different porosities: the empty markers correspond to the tests of Hyodo et al. (2013), the solid circles to those of Miyazaki et al. (2011), and the solid squares to those of Masui et al. (2005).

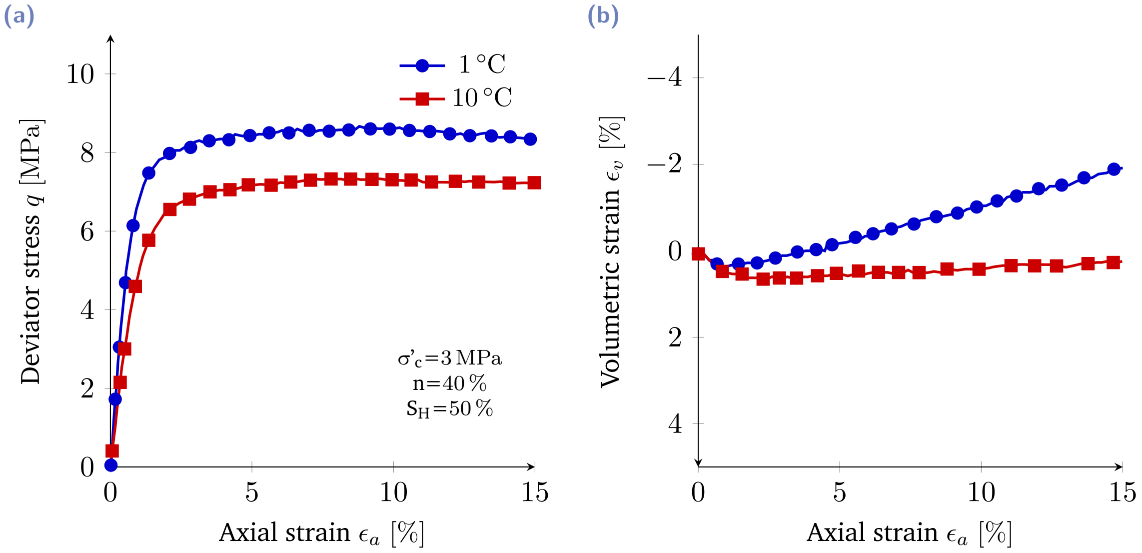

Fig. 2.17: Effect of temperature on the results of drained triaxial tests at fixed confining pressure (σ'_c=3 MPa) for samples with a hydrate saturation of about 50 % (Hyodo et al., 2013).

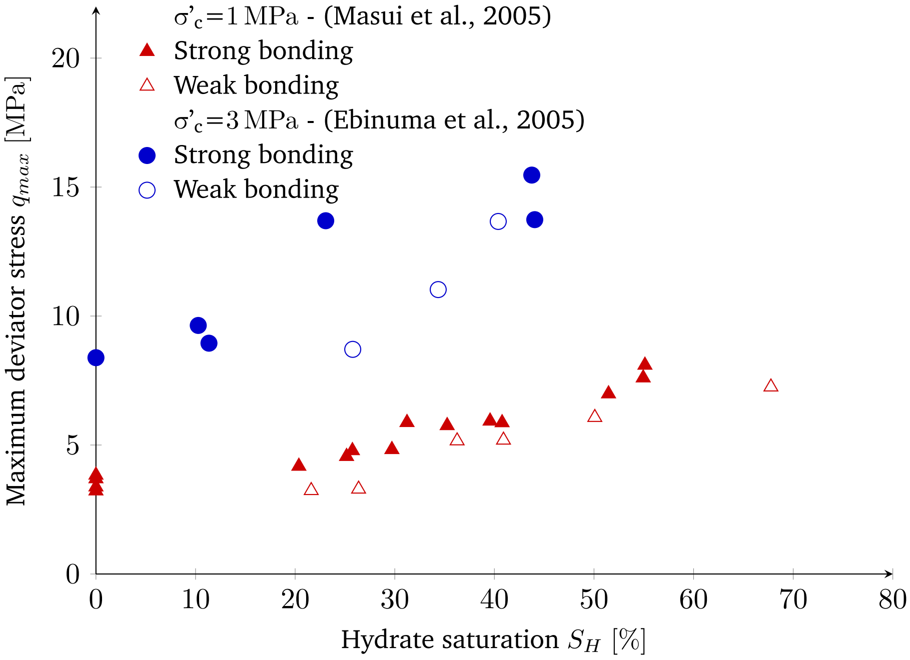

Fig. 2.18: Effect of the pore habit of methane hydrates, at fixed temperature (5 °C), on the strength of Toyoura sand samples at 1 MPa (Masui et al., 2005) and 3 MPa (Ebinuma et al., 2005) of confining pressure (after Soga et al., 2006).

remarks, as shown in Fig. 2.19: the higher the volume fraction of THF hydrates in the pores, the greater the maximum deviatoric stress and the stiffness. A confining pressure effect comparable to that observed for granular soils can also be seen, as well as the difference in sample response depending on the type of soil, kaolinite or silt.

2.3.3 Thermal properties

Studies on thermal properties have mainly focused on pure gas hydrates; relatively few studies exist on gas hydrates in the presence of porous sediments. In addition, the testing conditions of studies carried out on pure hydrates do not always correspond to natural conditions, especially since temperatures are often very low, which raises problems of ice formation and heterogeneity of the samples. Nonetheless, it is known that thermal data play a significant role in the mechanisms of gas hydrate formation and dissociation, including the thermal conductivity that governs thermal energy transfers. Sands have a higher conductivity (close to that of quartz) than clays for example; this plays a role in the apparent thermal conductivity of these soils and may be of interest for the gas recovery activities as the dissociation process is dominated by heat transfers.

The presence of different phases (sediments, pore liquid water, gas, ice and hydrates) and interfaces between these phases can greatly modify heat conduction modes compared to pure phases. Since the thermal conductivity of liquid water and hydrates are very similar,

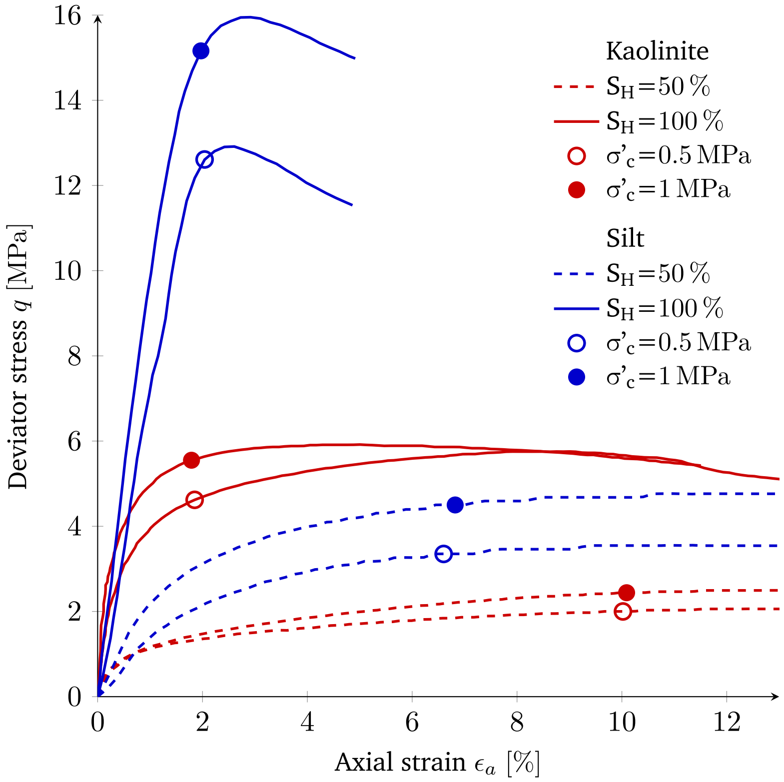

Fig. 2.19: Results of undrained triaxial tests on samples of fine soils containing tetrahydrofuran hydrates at different hydrate saturations, and different confining pressures (from Yun et al., 2007).

conventional two-phase models for sediments with water-saturated gas hydrates often provide suitable boundaries for the apparent conductivity of the material (Waite et al., 2009; Dai et al., 2015). However, the addition of a gas phase to the system can greatly modify the thermal behaviour of sediments with gas hydrates (Waite et al., 2009; Cortes et al., 2009). When the sample is unsaturated or saturated with gas, the behaviours differ from a simple phase mixing model, and the thermal conductivity varies from that of the saturated sample, as it has been shown for granular and fine soils containing THF hydrates (Cortes et al., 2009). Dai et al. (2015) demonstrated that for unsaturated sand systems with methane hydrates when the hydrate phase is less than $20\,\%$ of the pore volume, the measurements follow the arithmetic mean model for three phases. Beyond this value the thermal conductivity increases more rapidly than the conventional model for example. In addition to the effect of the interstitial liquid, the actual effective stress state influences conduction as does the porosity of the medium (Cortes et al., 2009).

The evolution of thermal conductivity during the formation and dissociation of gas hydrates in a soil sample has been observed for methane and THF (Cortes et al., 2009; Dai et al., 2015). The results agree that the appearance of gas hydrates in pores tends to increase thermal conductivitendty, compared to a non-frozen saturated sample, which remains difficult to explain because the liquid water and hydrate phases have about the same conductivity. In Dai et al. (2015) a decrease in conductivity is measured after methane hydrate dissociation in the sample. It is believed that this may have an impact on natural gas hydrate reservoir operations.

2.3.4 Flow properties

Permeability is a parameter related to Darcy's law that expresses the steady-state flow of an incompressible fluid through a porous medium, generated by a pressure gradient. It is an essential parameter that controls advective mass transport and heat transport of species in gas hydrate bearing sediments. Permeability has an influence on the flow of methane and therefore on the distribution and accumulation of gas hydrates and on the production of gas in reservoirs (Waite et al., 2009; Dai and Santamarina, 2014). However, like other characteristics of these sediments, it is quite difficult to assess permeability in the laboratory or in situ because of hydrate stability conditions and the dissociation/reformation effects of hydrates that can occur when circulating a fluid in a sample. The complexity of the analysis also lies in the fact that fluid flows are multiphase in soils with gas hydrates and involve the concepts of water and gas relative permeability.

Few studies exist on the permeability of soils with gas hydrates where most have been carried out in laboratories on synthetic samples (Minagawa et al., 2008; Kneafsey et al., 2011; Seol and Kneafsey, 2011; Konno et al., 2013) and few concern measurements on natural samples (Uchida and Tsuji, 2004; Li et al., 2014; Konno et al., 2015). These studies show that the formation of gas hydrates in sediments reduces pore size and thus increases capillary pressure, reduces permeability and increases tortuosity (Konno et al., 2015; Soga et al., 2006). These studies agree on the fact that the growth of hydrates and the way they occupy pores affect pore geometry and size. For the same hydrate saturation of the pore, different permeability values can be observed, for example. Permeability measurements for gas hydrate-rich soils have mostly been performed on granular soils. For this type of soils, the intrinsic permeability values are often higher (Konno et al., 2015) and the distribution of gas hydrates is more uniform, which is not the case for fine soils. Effective permeability values vary widely depending on sediment type, grain size, porosity, hydrate saturation and hydrate pore occupancy. Konno et al. (2015) give an effective permeability value $4.5 \times 10^{-14}\,\mathrm{m}^2$ for a natural sample of sandy sediments containing $70\,\%$ gas hydrates while the absolute permeability is estimated at:

- a few tens of $1 \times 10^{-18}\,\mathrm{m}^2$ for clayey sediments,
- a few tens of $1 \times 10^{-15}\,\mathrm{m}^2$ for silty sediments,
- about $1.5 \times 10^{-12}\,\mathrm{m}^2$ for sandy sediments.

2.4 Modelling of gas hydrate bearing soils

The environmental and energy challenges represented by natural gas hydrates have led to the development of different models. Controlling the risks associated with hydrate dissociation in sedimentary layers, as well as evaluating the performance of hydrate reservoirs, requires more accurate simulation of the behaviour of these soils. The first models were developed as a part of the assessment of the production capacities of the first known natural reservoirs, based on heat and mass transfers and considering a non-deformable solid phase. Publications of in situ mechanical tests and measurements quickly showed that the poor consolidation of sediments in reservoirs and the effect of gas hydrate dissociation on their mechanical behaviour should be taken into account. The deformations of the soil matrix influence, among other things, the porosity of the medium and therefore the flow characteristics of fluids and heat. Couplings between mechanics, hydraulics, thermal and medium chemistry are therefore important for predicting the behaviour of gas hydrate bearing sediments.

2.4.1 Fluid flow and thermal modelling

The first modelling efforts for the natural hydrate reservoirs were significant and resulted in fairly complete multi-physical numerical models such as TOUGH+HYDRATE (Moridis, 2003; Moridis, 2014), MH21 HYDRES (Kurihara et al., 2005), STOMP-HYD (White and Oostrom, 2006; White and Mcgrail, 2008). Collaborative work to compare these reservoir simulators also made it possible to validate and correct these numerical models in the absence of experimental data in 2008 (Wilder et al., 2008).

These models generally take into account:

- multiple phases (liquid, gas, ice, hydrate);
- multiple species (water, methane and other hydrocarbons, salts, inhibitors);
- phase equilibria for pure methane hydrate but also for composite hydrates, in the presence of salts and inhibitors;
- mass and heat transport equations for several fluids (gas, liquid), with advection, diffusion and conduction phenomena;
- the solubility of species in water, and water in the vapour phase;
- the effects of phase changes (formation/dissociation of hydrates, ice formation) in mass and heat balances.

Some parts of the models such as hydrate dissociation/formation or thermal conduction, lack reliable data and studies and are most often limited to conventional but effective models such as first-order kinetics for hydrate dissociation (Kim et al., 1987) and parallel, serial or geometric mean models for thermal conductivity. One of the main limitations of these theories remains the fact that the sedimentary matrix is considered non-deformable and does not affect fluid flows, for example during simulations at the reservoir scale.

2.4.2 Coupled models

Several models combining hydraulics, thermodynamics, and chemistry, with sediment mechanics have consequently been published in recent years (Rutqvist and Moridis, 2007; Rutqvist and Moridis, 2009; Klar et al., 2013; Sánchez et al., 2018; Gupta et al., 2016; Kimoto et al., 2010a; Freij-ayoub et al., 2007). The HYDRATE module of the TOUGH+ finite difference software (Lawrence Berkeley National Laboratory, Moridis, 2014) has for example been coupled to a mechanical FLAC 3D model (Rutqvist and Moridis, 2007; Rutqvist and Moridis, 2009) in an implicit sequential scheme. Different coupling strategies for multi-physical models simulating the behaviour of gas hydrate-rich soils have been adopted, most of them being partially coupled (Rutqvist and Moridis, 2007; Rutqvist and Moridis, 2009; Klar et al., 2010; Klar et al., 2013; Gupta et al., 2015; Gupta et al., 2016).

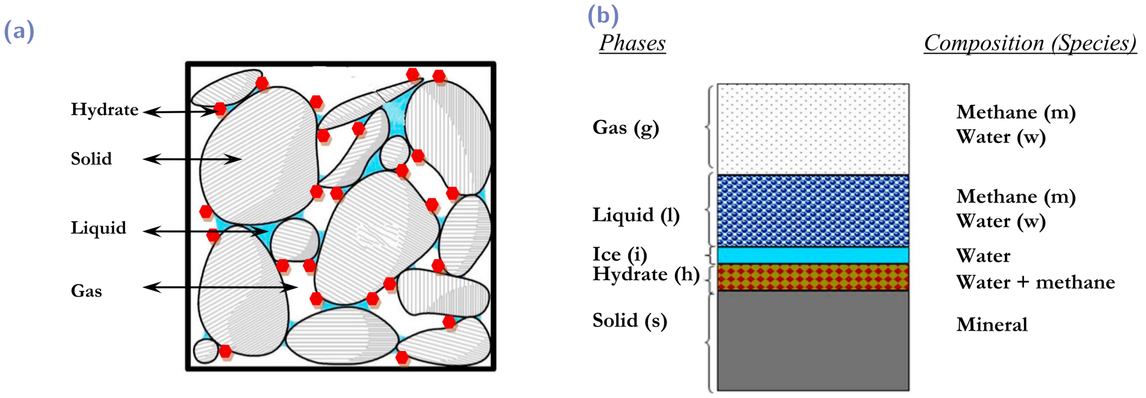

Fig. 2.20: (a) Diagram of the components of the Sánchez et al. (2018) model and (b) their distribution into phases and species.

One of the most advanced models is the fully coupled Sánchez et al. (2018) thermo-hydro-mechanical (THM) model, implemented within the CODE-BRIGHT finite element simulation software. The model involves 5 phases, composed of 3 different species (Fig. 2.20), and has been validated by comparison with a laboratory gas production test on a natural sample and by comparison with an analytical cylindrical reservoir model. The mechanical part is based on an elastoplastic critical state model, one of the main options included in the literature for constitutive modeling of soils containing gas hydrates.

2.4.3 Constitutive mechanical models

As mentioned above, the mechanical behaviour of gas hydrate bearing soils is complex and depends on many parameters. This is why at the moment, it is difficult to find a constitutive model that is perfectly in accordance with the characteristics of these soils and that is consensual. Several adaptations of existing models and theories had to be made in the literature to try to reproduce their macroscopic behaviour. In the literature, this behaviour has often been compared to the behaviour of dense soils or cemented materials for granular sediments (Uchida et al., 2012). The lack of experimental data for fine soils has also led to developments that are adapted to granular soils.

Most studies offer elastic-perfectly plastic models with Mohr-Coulomb criterion (Freij-ayoub et al., 2007; Klar et al., 2010; Miyazaki et al., 2012; Pinkert and Grozic, 2014) which only reflect the evolution of rigidity, shear strength and dilatancy as a function of hydrate saturation. Others are based on more complex elastoplastic critical state models with hardening (Sultan and Garziglia, 2011; Uchida et al., 2012; Lin et al., 2015; Sánchez et al., 2017), or visco-plastic models (Kimoto et al., 2010b) and even take into account the degradation of mechanical properties due to the dissociation of hydrates in the soil.

In order to reproduce as accurately as possible the effect of hydrates on the mechanical response, several authors introduce hardening parameters based on hydrate saturation, damage coefficients depending on plastic strains and modifying the contribution of hydrates to the mechanical behaviour. The concept of "subloading surfaces" is also introduced in several articles to help in the transition from the elastic to plastic regime (Uchida et al., 2012; Lin et al., 2015; Sánchez et al., 2017). While the latter models are better fitted to reproduce the main characteristics of soil behaviour with gas hydrates. This requires the introduction of many input parameters, up to 14 in the case of the Uchida et al. (2012) and 18 for the Sánchez et al. (2017) constitutive models. In addition, the "pore-habit" is rarely taken into account in these models. The addition of parameters in damage models and the fitting of calculation results on experimental curves is sometimes used as a means of calibrating parameter sets specific to each hydrate morphology. Unfortunately these parameters are not often validated afterwards. However, as discussed in the previous sections, hydrates can occupy pores in different forms at once in a single sample, making it difficult to generalise the introduction of parameters that are specific to each type of hydrate morphology.

2.5 Conclusion

Gas hydrates are naturally found around the globe in marine sediments or permafrost. Several countries have launched research programs due to the energy potential of hydrates and the environmental impact on submarine slope stability. Unfortunately, the instability of these compounds makes it difficult to characterise their physical properties, even more so in sedimentary environments. Several sophisticated models including multi-physical couplings have been developed to predict the behaviour of soils containing with gas hydrates. The consideration of mechanical behaviour laws in these models is quite recent, but the limited experimental data complicates the validation of these laws. In addition, observations of soil microstructures containing hydrates and shear test results on soils synthesised with different methods show a strong influence of the morphology of gas hydrates in the pores. The effect of microstructural heterogeneities on the behaviour of gas hydrate bearing soils is an important issue that must be taken into account. In addition to hydrate morphology, their specific mechanical behaviour also has an effect on the macroscopic response of soils. We have seen that the formation conditions of gas hydrates can influence their mechanical behaviour, especially through the influence these conditions can have on the crystal structure of the gas hydrates. The problem is that too little is known about the mechanical behaviour of pure gas hydrates.

3

Analytical homogenisation of elastic properties of GHBS

3.1 Introduction

As seen in the previous chapter, the elastic behaviour of a gas hydrate bearing soil depends strongly on multiple features of its microstructure. The elastic moduli in particular, depend on the volume fraction of the gas hydrates. The governing law of this behaviour was therefore determined by a homogenisation method. The principle of such method is to determine the behaviour of a representative elementary volume (REV) of a material, which is considered to be homogeneous at a macroscopic scale, from the characteristics of its heterogeneous microscopic structure. In order to do this, upscaling mathematical calculations are used (Dormieux et al., 2006).

Two approaches to homogenisation calculation are used in this chapter: Mori-Tanaka's and the so-called Self-Consistent approach. Mori-Tanaka's approach is based on an Eshelby problem in which pores or inclusions are integrated into a larger medium acting as a solid matrix, while the Self-Consistent approach applies to disordered heterogeneous microscopic configurations for which no matrix can be distinguished (Dormieux et al., 2006).

It is recalled that microscopic strains ϵ are related to macroscopic strains $\mathbf{E}$ at any point z of a volume V by the fourth-order strain localisation tensor $\mathbb{A}(z)$: $\epsilon = \mathbb{A} : \mathbf{E}$. The fourth-order stiffness tensor $\mathbb{C}$ links the microscopic strain to the microscopic stress tensor σ according to: $\sigma = \mathbb{C} : \epsilon$.
The unit tensor of order 4 $\mathbb{I}$ consists of its volumetric $\mathbb{J}$ and deviatoric $\mathbb{K}$ part: $\mathbb{I} = \mathbb{J} + \mathbb{K}$. The following rules are known and demonstrable (Dormieux et al., 2006): $\mathbb{J} : \mathbb{J} = \mathbb{J}$, $\mathbb{K} : \mathbb{K} = \mathbb{K}$, $\mathbb{J} : \mathbb{K} = \mathbb{K} : \mathbb{J}$ =0.

3.2 Homogenisation method in elasticity

The diagram of the REV for the considered material is represented on the figure 3.1. The same morphology as that of the Eschelby problem is used, i.e., a spherical inclusion in a

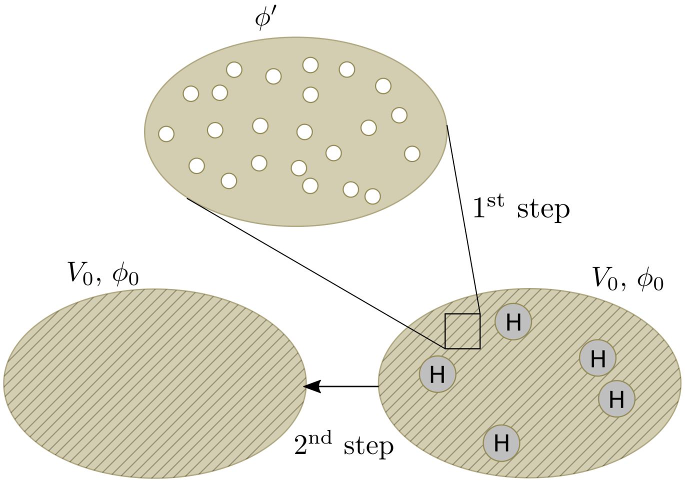

Fig. 3.1: Schematic representation of the material for the homogenisation calculations.

reference soil matrix. Moreover, all of the constituents of the REV are considered isotropic, which implies stiffness tensors of the following simple form for any element i:

$$\mathbb{C}_i = 3k_i\mathbb{J} + 2g_i\mathbb{K} \tag{3.1}$$

with $\mathbb{J}_{ijkl} = \frac{1}{3}\delta_{ij}\delta_{kl}$ the volumetric part of the 4th order identity tensor $\mathbb{I}$ and $\mathbb{K} = \mathbb{I} - \mathbb{J}$ the deviatoric part; and finally k_i and g_i the bulk and shear moduli of the component i.

A first homogenisation calculation considering a soil matrix with spherical inclusions of gas hydrates was considered, but this calculation implied that for each value of S_H (the pore volume fraction of gas hydrates) a part of the soil was replaced by hydrates. The volume fraction of the soil phase would change with the hydrate phase. With no modification of the initial elastic properties of the soil, this would be very far from reality. Indeed, the moduli k and g depend on the porosity of the material. As it can be seen in Fig. 3.1, finally a double homogenisation calculation for REV's of different scales of the same material has been chosen. Hydrates occupy the largest pores of the soil matrix, while the small ones are considered empty. The first homogenisation step consists then in determining the elastic characteristics of the medium formed by the soil and the empty inclusions of the small pores. For this calculation, we consider a porosity different from the initial one ϕ_0. We therefore have a volume which corresponds to the total volume V_0 minus the volume of the pores filled with hydrates V_H, and a corresponding porosity ϕ':

$$\phi' = \frac{V_\mu}{V_0 - V_H} = \frac{(1 - S_H)\phi_0}{1 - S_H\phi_0} \tag{3.2}$$

$$\text{knowing that} \quad \phi_0 = \frac{V_\mu + V_H}{V_0} \quad \text{and} \quad S_H = \frac{V_H}{V_\mu + V_H} \tag{3.3}$$

where ϕ_0 is the porosity of the REV with hydrates, and V_μ is the total volume of the empty pores. The respective elastic moduli of the soil matrix (s) and hydrates (h) are called k_s, g_s, k_h, and g_h for the following parts.

The first homogenisation step uses the Self-Consistent approach since it involves a solid phase distribution and empty spaces without a real matrix (Fig. 3.1). The second step is based on the Mori-Tanaka's approach with gas hydrates as inclusions and the homogenised medium from the first calculation as the solid matrix, whose elastic moduli will be noted as k_{sc} and g_{sc}.

3.2.1 First homogenisation step

In the book entitled *Microporomechanics*, Dormieux et al. (2006) detail the homogenisation calculation of a linear microporoelasticity problem based on the Mori-Tanaka approach and the Self-Consistent approach, in the particular case of a soil containing empty pores, whose rigidity is considered zero ($\mathbb{C}^p = 0$). Their calculations use the solution of the Eshelby inhomogeneity problem to determine the microscopic mean strains of the pores $\bar{\epsilon}^p$ and the solid $\bar{\epsilon}^s$. The use of the symbol $\bar{\cdot}$ represents the spatial average over the whole material volume; $\bar{\cdot}^p$ represents the spatial average over the pore volume and $\bar{\cdot}^s$ represents the spatial average over the solid volume. In the case of the Self-Consistent approach, the idea is to consider that each element of a phase (solid or pore) reacts as if it were included in a matrix formed by the homogenised medium whose characteristics are sought. Eshelby's results (Eshelby, 1957) can then be used by introducing $\mathbb{C}^{sc}$ the stiffness matrix of the homogenised medium:

$$\bar{\epsilon}^p = (\mathbb{I} + \mathbb{P}^{sc} : (\mathbb{C}^p - \mathbb{C}^{sc}))^{-1} : \mathbf{E}_0 = (\mathbb{I} - \mathbb{P}^{sc} : \mathbb{C}^{sc})^{-1} : \mathbf{E}_0 \tag{3.4}$$

$$\bar{\epsilon}^s = (\mathbb{I} + \mathbb{P}^{sc} : (\mathbb{C}^s - \mathbb{C}^{sc}))^{-1} : \mathbf{E}_0 \tag{3.5}$$

where $\mathbb{P}^{sc} = \mathbb{S} : (\mathbb{C}^{sc})^{-1}$, $\mathbb{S}$ being the Eshelby tensor of order 4, and where $\mathbf{E}_0$ is the limit of macroscopic strains at infinity.

The following mean strain condition, linking microscopic and macroscopic deformations: $\bar{\epsilon} = \mathbf{E}$ which is also written: $\phi_0\, \bar{\epsilon}^p + (1 - \phi_0)\, \bar{\epsilon}^s = \mathbf{E}$, allows to determine the relationship between $\mathbf{E}_0$ and $\mathbf{E}$, and finally get the average strain localisation tensors $\bar{\mathbb{A}}^p$ and $\bar{\mathbb{A}}^s$ (with $\alpha = s$ or p):

$$\bar{\mathbb{A}}^\alpha = (\mathbb{I} + \mathbb{P}^{sc} : (\mathbb{C}^\alpha - \mathbb{C}^{sc}))^{-1} : \overline{(\mathbb{I} + \mathbb{P}^{sc} : (\mathbb{C}^\alpha - \mathbb{C}^{sc}))^{-1}}^{-1} \tag{3.6}$$

Finally, the general expression of the homogenised stiffness matrix (Dormieux et al., 2006),

$$\mathbb{C}^{hom} = \overline{\mathbb{C} : \mathbb{A}} \tag{3.7}$$

(from the mean stress condition $\bar{\sigma} = \Sigma$, Σ being the macroscopic stress tensor) allows to deduct $\mathbb{C}^{sc}$:

$$\mathbb{C}^{sc} = \overline{\mathbb{C} : (\mathbb{I} + \mathbb{P}^{sc} : (\mathbb{C} - \mathbb{C}^{sc}))^{-1}} \tag{3.8}$$

The average over a volume V composed of a set of pores V_p and a volume of solid V_s gives the following development (knowing that $\mathbb{C}$ is equal to $\mathbb{C}^s$ over V_s and to zero over V_p):

$$\mathbb{C}^{sc} = (1 - \phi_0)(\mathbb{C}^s : (\mathbb{I} + \mathbb{P}^{sc} : (\mathbb{C}^s - \mathbb{C}^{sc}))^{-1}) \tag{3.9}$$

If we break down the tensors $\mathbb{C}^s$, $\mathbb{C}^{sc}$, and $\mathbb{P}^{sc}$ into their volumetric and deviatoric parts, for an isotropic material and assumed spherical inclusions:

$$\mathbb{C}^s = 3k^s\mathbb{J} + 2g^s\mathbb{K} \tag{3.10}$$

$$\mathbb{C}^{sc} = 3k^{sc}\mathbb{J} + 2g^{sc}\mathbb{K} \tag{3.11}$$

$$\mathbb{P}^{sc} = \frac{\alpha^{sc}}{3k^{sc}}\mathbb{J} + \frac{\beta^{sc}}{2g^{sc}}\mathbb{K} \tag{3.12}$$

with: $\alpha^{sc} = \dfrac{3k^{sc}}{3k^{sc} + 4g^{sc}}$ and $\beta^{sc} = \dfrac{6(k^{sc} + 2g^{sc})}{5(3k^{sc} + 4g^{sc})}$, we can replace them in the equation 3.9 and find the expressions of the elastic moduli k^{sc} and g^{sc}:

$$k_{sc} = (1 - \phi')\frac{k_s}{1 + \alpha_{sc}(k_s - k_{sc})/k_{sc}} \tag{3.13}$$

$$g_{sc} = (1 - \phi')\frac{g_s}{1 + \beta_{sc}(g_s - g_{sc})/g_{sc}} \tag{3.14}$$

where α_{sc} and β_{sc} are the coefficients of the volumetric and deviatoric parts of the Eshelby fourth-order tensor respectively of the homogenised medium, in the case of spherical inclusions: $\mathbb{S}_{sc} = \alpha_{sc}\mathbb{J} + \beta_{sc}\mathbb{K}$. These equations are coupled and can be solved with an iterative method. The tensor $\mathbb{S}_{sc}$ is used to estimate the average of the strain localisation tensor $\mathbb{A}$ (Ulm et al., 2004), and the coefficients are:

$$\alpha_{sc} = \frac{3k_{sc}}{3k_{sc} + 4g_{sc}} \tag{3.15}$$

$$\beta_{sc} = \frac{6(k_{sc} + 2g_{sc})}{5(3k_{sc} + 4g_{sc})} \tag{3.16}$$

By solving the system of coupled equations numerically (Newton-Raphson method, for example), we obtain the homogenised elastic moduli of the material {soil + empty pores} for the given porosity ϕ'. However, it is not easy to know the values of k_s and g_s of a soil, especially in the case of fine-grained soils for which the solid phase can be made up of various minerals for instance. Moreover, the solid phase can be damaged, if we think of the presence of cracks in coarse grains, and the elastic moduli can be different from their theoretical values. The literature gives values of moduli k_s and g_s of generally a few dozens GPa (example of quartz: k_s is about $36\,\mathrm{GPa}$). The elastic characteristics of a soil are most often available at a non-zero reference porosity of ϕ_r. In this case, it is sufficient to draw

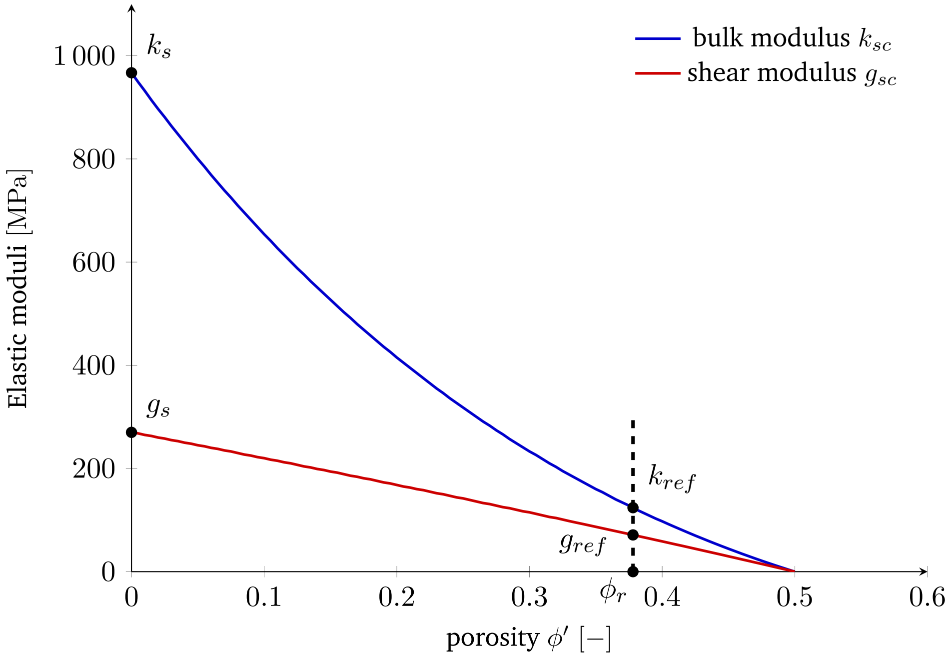

Fig. 3.2: Bulk k_{sc} and shear g_{sc} moduli of a soil as a function of porosity. Reference data: Toyoura sand, $\phi_r = 0.378$, $k_{ref} = 123.9\,\mathrm{MPa}$, $g_{ref} = 71.2\,\mathrm{MPa}$ (Miyazaki et al., 2011).

the curves of k_{sc} and g_{sc} according to porosity and to find the values of k_s and g_s which allow to reach the measured moduli at porosity ϕ_r, as in the figure 3.2, where we obtain $k_s = 967\,\mathrm{MPa}$ and $g_s = 270\,\mathrm{MPa}$.

The values of k_s and g_s obtained do not exceed one GPa, which seems low. It is worth noting that reference values for quartz moduli are measured under small-strain conditions, using methods such as resonant column or seismic velocities, and are intrinsically high values compared to measurements at larger strains. It could also be explained by the fact that the confining pressure can have a significant influence on the reference values. Furthermore, this first homogenisation method is not optimal in the case of coarse-grained soils, where considering a solid matrix may ultimately seem a little out of touch in reality.

3.2.2 Second homogenisation step

For this second homogenisation calculation, by using the general expression of the homogenised stiffness tensor $\mathbb{C}^{hom}$ (Eq. 3.7) and developing its average, according to the constituting elements of the considered medium (homogenised matrix {solids + pores} and hydrate inclusions):

$$\mathbb{C}^{mt} = \overline{\mathbb{C} : \mathbb{A}} = S_H \phi_0 \mathbb{C}^h \bar{\mathbb{A}}_h + (1 - S_H \phi_0) \mathbb{C}^{sc} \bar{\mathbb{A}}_{sc} \tag{3.17}$$

The localisation tensors are decomposed, in the isotropic case, according to the following expression (with $\alpha = sc$ or h): $\bar{\mathbb{A}}_\alpha = \bar{\mathbb{A}}^v_\alpha \mathbb{J} + \bar{\mathbb{A}}^d_\alpha \mathbb{K}$.

The estimation of these average localisation tensors is now based on an article by Ulm et al. (2004), which gives:

$$\bar{\mathbb{A}}_{\alpha}^{est} = (\mathbb{I} + \mathbb{S}_{\alpha} : ((\mathbb{C}^{sc})^{-1} : \mathbb{C}^{\alpha} - \mathbb{I}))^{-1} : \overline{(\mathbb{I} + \mathbb{S}_{\alpha} : ((\mathbb{C}^{sc})^{-1} : \mathbb{C}^{\alpha} - \mathbb{I}))^{-1}}^{-1} \tag{3.18}$$

So by replacing $\mathbb{C}^h$, $\mathbb{C}^{sc}$, $\mathbb{S}_h$, $\mathbb{S}_{sc}$, with their expressions below:

$$\mathbb{C}^h = 3k^h\mathbb{J} + 2g^h\mathbb{K} \tag{3.19}$$

$$\mathbb{C}^{sc} = 3k^{sc}\mathbb{J} + 2g^{sc}\mathbb{K} \tag{3.20}$$

$$\mathbb{S}_h = \alpha_h\mathbb{J} + \beta_h\mathbb{K} \tag{3.21}$$

$$\mathbb{S}_{sc} = \alpha_{sc}\mathbb{J} + \beta_{sc}\mathbb{K} \tag{3.22}$$

we get:

$$A_h^v = \frac{1}{1 + \alpha_{sc}(\frac{k^h}{k^{sc}} - 1)} \left[\frac{S_H\phi_0}{1 + \alpha_{sc}(\frac{k^h}{k^{sc}} - 1)} + (1 - S_H\phi_0) \right]^{-1} \tag{3.23}$$

$$A_h^d = \frac{1}{1 + \beta_{sc}(\frac{g^h}{g^{sc}} - 1)} \left[\frac{S_H\phi_0}{1 + \beta_{sc}(\frac{g^h}{g^{sc}} - 1)} + (1 - S_H\phi_0) \right]^{-1} \tag{3.24}$$

$$A_{sc}^v = \left[\frac{S_H\phi_0}{1 + \alpha_{sc}(\frac{k^h}{k^{sc}} - 1)} + (1 - S_H\phi_0) \right]^{-1} \tag{3.25}$$

$$A_{sc}^d = \left[\frac{S_H\phi_0}{1 + \beta_{sc}(\frac{g^h}{g^{sc}} - 1)} + (1 - S_H\phi_0) \right]^{-1} \tag{3.26}$$

and we deduce the complete expression of k_{mt} and g_{mt} via the equation 3.17 (with a relationship of the type 3.10):

$$k_{mt} = \sum_{i=0}^{n} f_i k_i A_i^v = S_H\phi_0 k_h A_h^v + (1 - S_H\phi_0) k_{sc} A_{sc}^v \tag{3.27}$$

$$g_{mt} = \sum_{i=0}^{n} f_i g_i A_i^d = S_H\phi_0 g_h A_h^d + (1 - S_H\phi_0) g_{sc} A_{sc}^d \tag{3.28}$$

where A_i^v and A_i^d are the volumetric and deviatoric parts of the estimate of the average of the strain localisation tensor $\mathbb{A}_i$ for each component i of the heterogeneous microscopic medium (Ulm et al., 2004), which can be written:

$$< \mathbb{A}_i >_{V_i}^{est} = A_i^v\mathbb{J} + A_i^d\mathbb{K}.$$

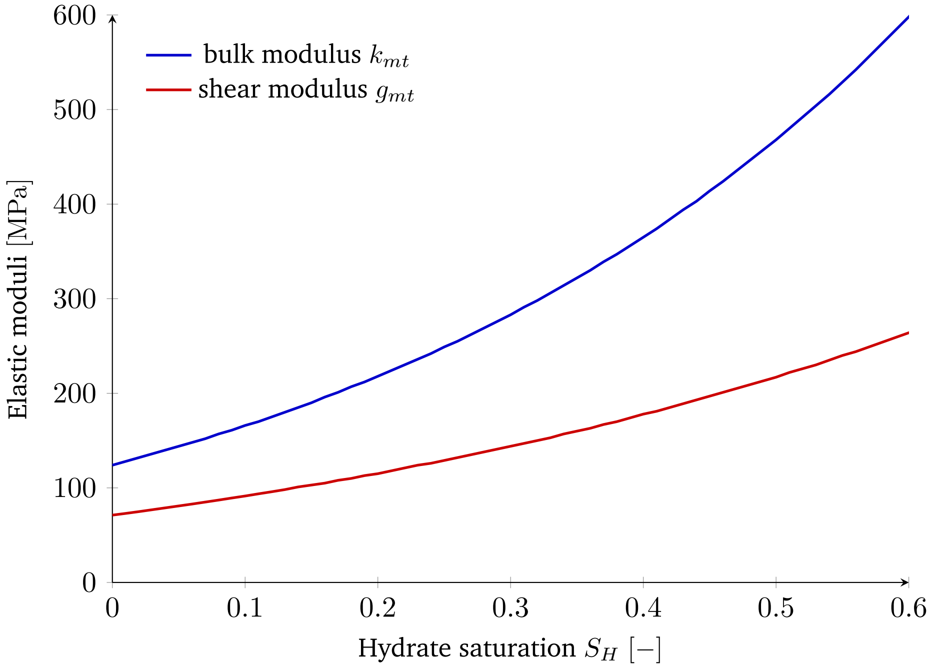

Fig. 3.3: Elastic moduli of compressibility k_{mt} and shear g_{mt} of a soil sample as a function of hydrate saturation.

The resolution of the calculations by the Mori-Tanaka approach is more straightforward since the expressions of the homogenised moduli, noted k_{mt} and g_{mt}, are not coupled. They depend on the characteristics of the matrix phase (k_s and g_s), of the methane hydrate phase (k_h and g_h), and on the volume fraction of the hydrates, i.e. the product $\phi_0 S_H$. Finally, using the example of the data in Fig. 3.2, for a given porosity ϕ_r of 0.378, and for $k_h = 8.76\,\mathrm{GPa}$ and $g_h = 3.57\,\mathrm{GPa}$ (Sloan and Koh, 2007) we obtain the curves in Fig. 3.3.

3.3 Comparison with experimental data

Miyazaki et al. (2011) conducted a series of drained triaxial compression tests on samples with different hydrate saturations and different confining pressures. Three types of sand were used during the tests to make the specimens in the laboratory: Toyoura sand, silica sand 7 and silica sand 8. The authors were particularly interested in the secant Young's modulus and the secant Poisson's ratio, as they are easier to assess from the experimental curves than the initial tangent ones.

The secant Young's modulus and Poisson's ratio were also measured for water saturated samples, with no hydrate formation. The average of these values (see Tab. 3.1) for each different testing confining pressure were used as reference parameters for the Self-Consistent calculation at porosity $\phi'_{ref} = 0.38$. The elastic moduli of the hydrate phase were taken equal to the ones given by Sloan and Koh (2007) (see Tab. 3.1).

Tab. 3.1: Parameters used for the comparative calculations with the experimental data from (Miyazaki et al., 2011) at different confining pressures for the Toyoura sand samples.

Parameters	confining pressures		
	$\sigma'_c = 1.0\,\mathrm{MPa}$	$\sigma'_c = 2.0\,\mathrm{MPa}$	$\sigma'_c = 3.0\,\mathrm{MPa}$
sand sample			
k_{ref} (MPa)	129	179	195
g_{ref} (MPa)	96	149	189
hydrate			
k_h (GPa)		8.76[a]	
g_h (GPa)		3.57[a]	

[a] from Sloan and Koh (2007)

By taking these results and deducting the elastic bulk modulus k and shear modulus g for various hydrate saturations, it was therefore possible to compare the experimental moduli with those calculated using the homogenisation method with spherical inclusions of hydrates. These comparative curves for Toyoura sand are shown in Fig. 3.4. It can be seen that the moduli calculated by homogenisation overestimate the experimental values. However, they do reflect the general trends in the elastic behaviour of the tested samples.

The same method was applied with the results of Masui et al. (2005), who performed the same kind of tests as Miyazaki et al. (2011), with Toyoura sand but for one confining pressure ($\sigma'_c = 1.0\,\mathrm{MPa}$) and two different methods of synthesising hydrates at two different initial porosities. The gas hydrates were created by percolating methane gas into ice-sand (type A) and water-sand prepared specimens at a temperature of $278\,\mathrm{K}$, a pore pressure of $8\,\mathrm{MPa}$ and a confining pressure of $9\,\mathrm{MPa}$. The authors also determined the secant Young's modulus and Poisson's ratio, and tested four water saturated samples without any hydrates, but the four results were too scattered. The best exponential regression of the data hence gave us the estimated reference values at zero hydrate saturation used for the calculations, and they can be found in Tab. 3.2.

The comparative results between the analytical homogenisation and experimental data from Masui et al. (2005) are represented in Fig. 3.5. If the homogenised elastic moduli seem to better fit the experimental curves for the tested specimens of Type A this time (Fig. 3.5), there is still an overestimation of the shear modulus at least for the specimens of Type B.

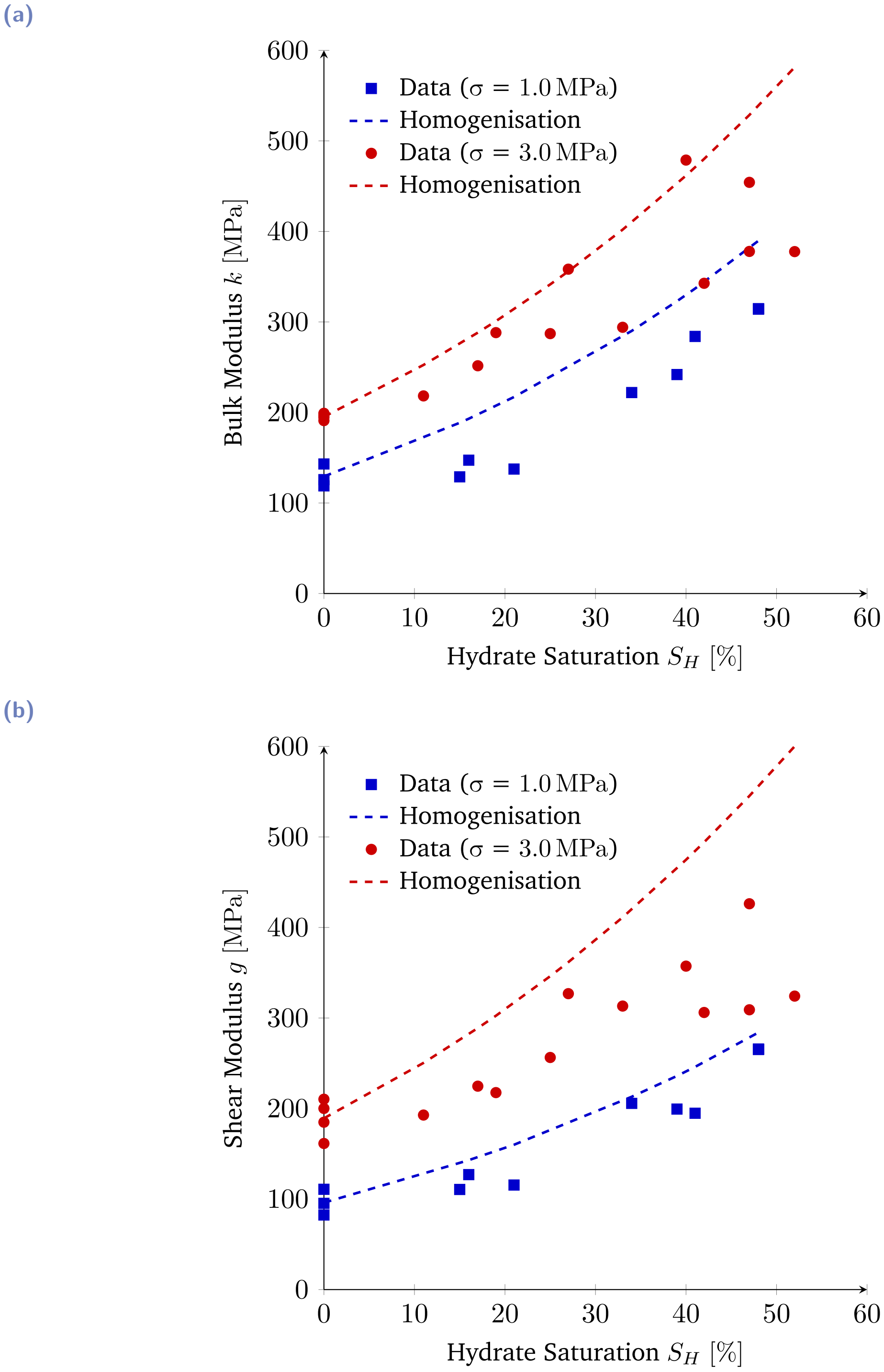

Fig. 3.4: Comparative curves between the experimental elastic moduli (a) k, and (b) g from Miyazaki et al. (2011) and those calculated by homogenisation at $1.0\,\mathrm{MPa}$ and $3.0\,\mathrm{MPa}$ of confining pressures.

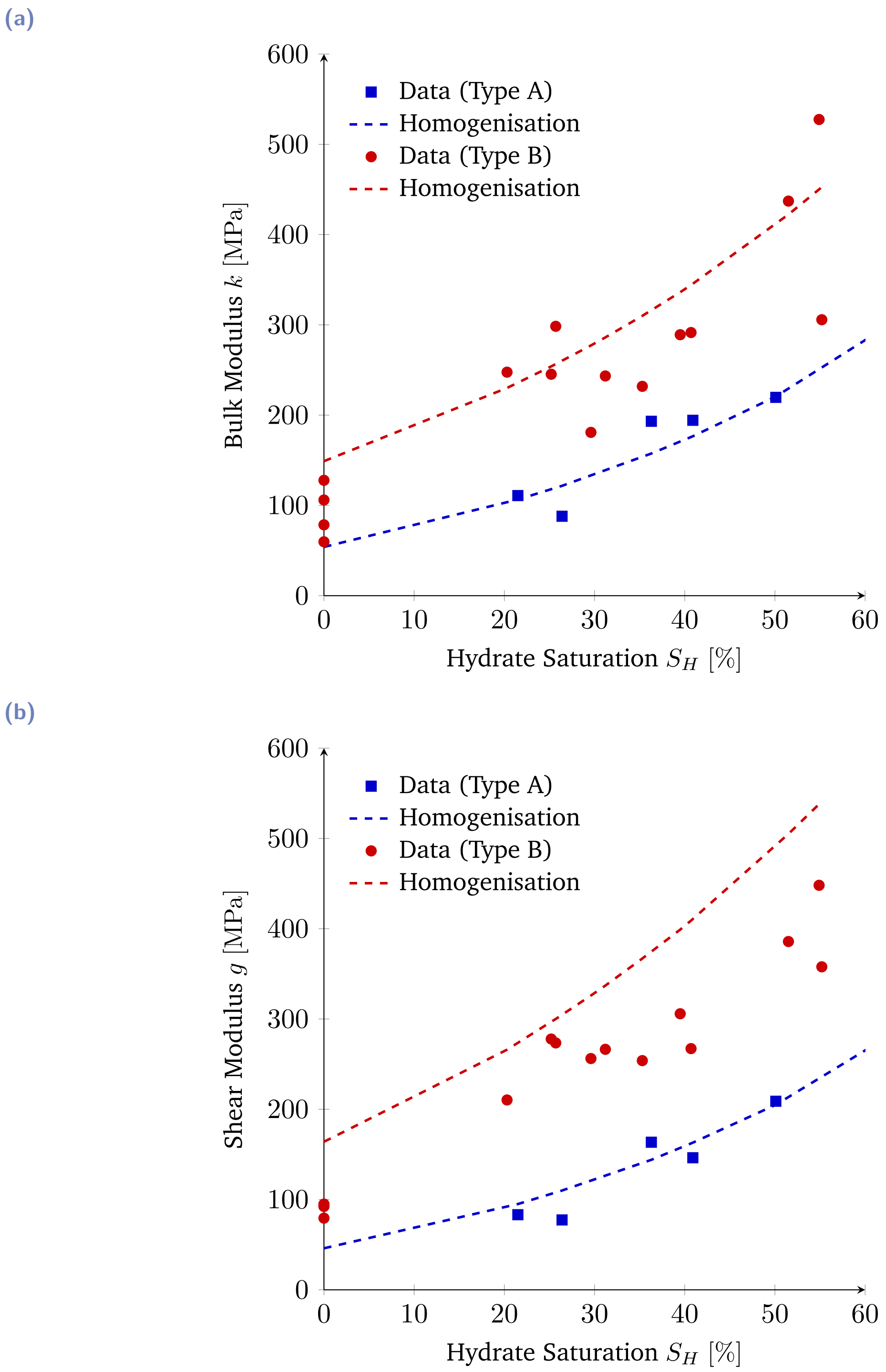

Fig. 3.5: Comparative curves between the experimental elastic moduli (a) k, and (b) g from Masui et al. (2005) and those calculated by homogenisation for tested specimens of Type A and Type B.

Tab. 3.2: Parameters used for the comparative calculations with the experimental data from (Masui et al., 2005) for different methods of synthesising hydrates.

Synthesis method	Type A	Type B
ϕ'_{ref}	0.42	0.37
$k_{ref}{}^{*}$ (MPa)	46	164
$g_{ref}{}^{*}$ (MPa)	54	149

* calculated from regression

3.4 Mechanical simulations

The calculations were performed using the finite element calculation software, for samples with fixed hydrate saturation; hydrate dissociation is not simulated. A plastic Drucker-Prager criterion is used. It was preferred to choose a simple model that takes into account the evolution of the material's stiffness as a function of methane hydrate saturation, but also the increase in apparent cohesion and dilatancy with the increase in this saturation. The evolution of the apparent cohesion allows to obtain an apparent hardening of the samples according to the hydrate saturation. The homogenisation calculation seen in the previous section was added to the calculation code for the elastic part of the behaviour.

Concerning the evolution of the stiffness parameters (cohesion, peak deviator stress, friction angle) and angle of dilation, two experimental data sets were studied: the results of the drained triaxial compression tests of Masui et al. (2005) and Hyodo et al. (2013) carried out on Toyoura sand samples with synthetic methane hydrates. The results of Masui et al. (2005) are given for a confining pressure of 1 MPa and a porosity of 0.37 while those of Hyodo et al. (2013) correspond to a confining pressure of 5 MPa and a porosity of 0.39. In their paper Hyodo et al. (2013) also performed tests for a confining pressure of 1 MPa, but only the maximum deviator stress and Young's modulus were provided, no curve was available to test the mechanical part of the model described previously. Based on the results of the samples tested by Masui et al. (2005), Uchida et al. (2012) gave the following relationships:

$$\varphi' = 33.9° \tag{3.29}$$

$$c' = 10S_H^3 + 0.15 \quad (\mathrm{MPa}) \tag{3.30}$$

$$\psi = 24S_H^{0.6} \quad (°) \tag{3.31}$$

where S_H, φ' and ψ refers to the methane hydrate saturation, the friction angle and the angle of dilation respectively. These are the relationships that have been added to the simulation code for Masui test modeling. The assumption was made that the friction angle was independent of the gas hydrate saturation. By keeping the same assumption for Hyodo's data, we can obtain the value of the resistance parameters (cohesion and friction). In particular, there is a friction angle of 30.08°, and the cohesion is deduced from the value

Tab. 3.3: Results of Hyodo et al. (2013) triaxial tests for a confining pressure of 5 MPa.

Porosity φ' (%)	Hydrate saturation S_H (%)	Maximum deviator stress $q_{\max}$ (MPa)	Cohesion c' (MPa)	Dilatancy ψ (°)
00.0	39.4	10.32	0.120	-6.82
24.2	39.6	10.71	0.191	-4.47
35.1	39.2	11.84	0.516	-1.91
53.1	40.1	14.74	1.352	5.27

of the maximum deviator stress for each sample, using the Drucker-Prager criterion. The dilation angle is also estimated from the curves giving the volumetric strain as a function of the axial strain provided by Hyodo et al. (2013). Tab. 3.3 summarises the results of the paper by Hyodo et al. (2013) for a confining pressure of 5 MPa, as well as the cohesion estimate and the dilation angle.

It should be noted that unlike Masui's results, which demonstrate dilatancy in the presence of methane hydrates, Hyodo samples remain contractant until a fairly high saturation of hydrates (around 40%) is reached. This could be due to the difference in confining pressure, but more results in the literature are needed to confirm this trend. Finally, these values of c' and ψ allow to obtain by correlation (Fig. 3.6) the modeling of the strength and dilatancy parameters:

$$\varphi' = 30.08° \tag{3.32}$$

$$c' = 8.5S_H^3 + 0.12 \quad (\mathrm{MPa}) \tag{3.33}$$

$$\psi = 4.6S_H^2 - 2.09S_H - 6.8 \quad (°) \tag{3.34}$$

For elastic moduli, Hyodo et al. (2013) gives the Young's modulus of pure Toyoura sand ($S_H = 0\%$) for a porosity of 0.39, which is 653 MPa. Taking this value, and a Poisson's ratio of 0.2, the reference curve of the elastic moduli as a function of porosity is deduced. From this curve we can determine our reference values for each of the Hyodo samples tested, but the porosity being almost the same in each case the input reference value remains around 650 MPa. For Masui's data the reference modulus is set from the elastic modulus values estimated from the curves of the deviator stress in function of the axial strain, which correspond to the value calculated at the end of homogenisation. We finally find a reference value of 200 MPa for a porosity of 0.37, which is lower. We notice that these values are quite distinct for tests thats have used identical sands. Indeed, Masui's results show significantly less rigidity than those of Hyodo. The relationships previously established for strength parameters and dilation angle are added to the Drucker-Prager model in Bil software, as well as the homogenisation calculations. The input parameters of the computation that interest us are therefore: porosity φ, hydrate saturation S_H, reference Young's modulus (for the given porosity) E_{ref}, reference Poisson's ratio ν_{ref}, hydrate Young's modulus E_h, and the Poisson's ratio ν_h (Tab. 3.4).

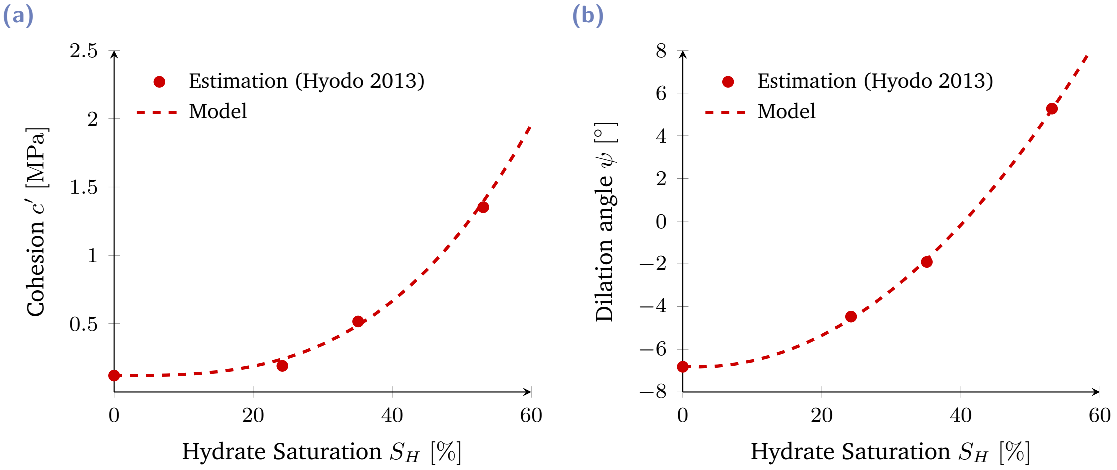

Fig. 3.6: Cohesion (a) and dilation angle (b) as a function of hydrate saturation: fitting of models on the data of Hyodo et al. (2013)

Tab. 3.4: Paramètres d'entrée pour les calculs aux éléments finis.

Data reference	Masui et al., 2005	Hyodo et al., 2013
ϕ (%)	0.37	0.39
S_H (%)	7.7, 37.6	0.0, 24.2, 35.1, 53.1
E_{ref} (MPa)	200	650
ν_{ref} (-)	0.2	0.2
E_h (GPa)	9.44[a]	
ν_h (-)	0.32[a]	

[a] from k_h and g_h values in Sloan and Koh (2007)

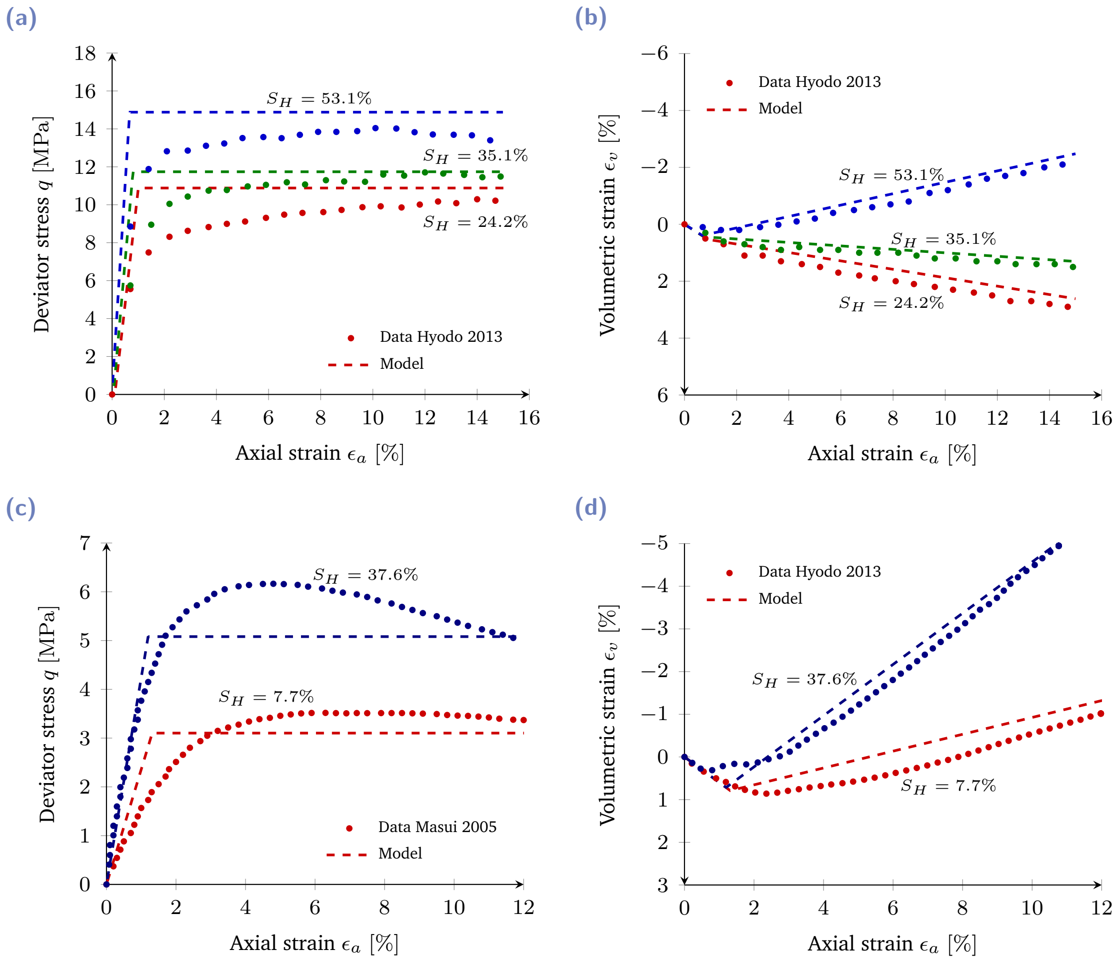

Fig. 3.7: Comparison between the model and the experimental results of (a), (b) Hyodo et al. (2013) and (c), (d) Masui et al. (2005). (a), (c) deviator stress curve and (b), (d) volumetric strain curve as functions of axial strain.

The curves obtained are shown in Fig. 3.7. The results for the elastic part, and the evolution of the moduli as a function of S_H are quite satisfactory. As the models for the strength and dilatancy parameters have been based on experimental observations, it is not surprising to obtain calculation curves that correspond to the experimental data. However, it is interesting to note that the expression of cohesion as a function of S_H remains relatively close from one dataset to another, while the phenomenon of dilatancy is not the same at all between Hyodo et al. (2013) and Masui et al. (2005).

Tests carried out on hydrates are still limited in the literature, and use for the vast majority of them samples synthesised in the laboratory from granular soils. It is therefore still quite difficult to describe the influence of methane hydrates on the mechanical properties of sediments, although trends are emerging: increased rigidity and cohesion with S_H in drained triaxial tests. It seems difficult to comment on the evolution of the angle of friction and dilatance as a function of S_H. Indeed, we have seen that the confining pressure could perhaps have a role to play. The calculations in this section were limited to a model that was perfectly plastic and samples with constant hydrate saturation. The development of more complex mechanical models would imply more input parameters and sometimes non realistic ones though. Numerical homogenisation and multiscale approaches can represent an other method to take into acount the complexity of such soils.

3.5 Conclusion

The analytical homogenisation results represent a practical method to calculate the elastic moduli of gas hydrate bearing sediments as they can easily be used in a more advanced multi-physical model such as the ones described in section 2.4. The method we chose gave good trends of the stiffening of specimens with the gas hydrate saturation, but with an overestimation of the values of the bulk and shear moduli. Moreover there is no explicit dependency of the homogenised elastic parameters with the confining pressure or with the pore-habit of hydrates in the granular host sand, in these calculations.

The analytical homogenisation may be too limited to capture the complex morphologies of gas hydrates in the voided space of different types of soils. We know that there are more than one type of pore-habit for hydrates occurring in granular soils, and if they can be well represented with simple geometrical shapes of inclusions, it is not the case for gas hydrates in fine soils. Indeed, they form under various complex shapes like veins. One problem with this kind of calculation is also the lack of reference values for the elastic properties of each phases of the gas hydrate soils, and of the gas hydrate bearing soils themselves. We only have acces to mechanical tests results concerning granular soils for now, with only conjectures based on seismic velocity measurements of the mode of occupation of the pores by the synthesised gas hydrates.

The numerical homogenisation methods appear as a good way to overcome these limitations and capture the effect of microstructural heterogeneities and non-linearities of the constituent phases as more complex images or meshes can be used for instance. This is the subject of the next chapter.

4

Numerical homogenisation in elasticity and plasticity

4.1 Introduction

This chapter presents the periodic mechanical homogenisation method adopted during this thesis. The computation of the homogenised elastic properties of a REV using a numerical approach is less restrictive on the choice of the microstructure geometry and can be very useful for the modelling of a constitutive behaviour. Indeed, these approaches could be used in the development of a numerical mechanical model for gas hydrate bearing sediments including inelastic behaviour of a constituting phase at the microstructural level.

4.2 Principle of periodic mechanical homogenisation

The principle of the periodic mechanical homogenisation adopted here is based on the resolution of the local mechanical problem, i.e. at the scale of the microstructure, defined for an elementary periodic cell subjected to a macroscopic uniform strain loading $\boldsymbol{E}$. The first step of the method is to define a periodic unit cell, the REV $\varOmega$, with symmetric opposite surface elements constituted by different phases with independent properties. The periodic replication of this elementary geometry results in a generalised composite medium to homogenise. Over this periodic elementary cell, the displacement u and strain $\boldsymbol{\epsilon}$ fields are split into the following components:

$$\boldsymbol{\epsilon}(x) = \boldsymbol{E} + \boldsymbol{\epsilon}(u'(x)) = \boldsymbol{E} + \boldsymbol{\epsilon}'(x) \tag{4.1}$$

$$u(x) = \boldsymbol{E} \cdot x + u'(x) \tag{4.2}$$

where $\boldsymbol{E}$ is the macroscopic strain applied to the REV and corresponds to the strain average over the entire cell: $\langle \boldsymbol{\epsilon} \rangle = \boldsymbol{E}$. This means that $\boldsymbol{\epsilon}'$ and u' are the local fluctuating strains and

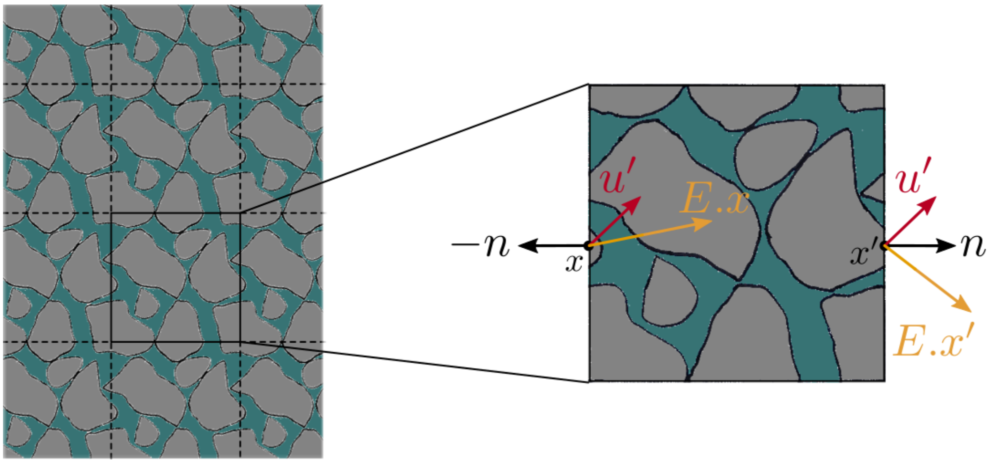

Fig. 4.1: Boundary conditions for periodic homogenisation.

displacements of the REV, and that they are periodic functions of space with a null average value over the REV. The local mechanical problem to solve over the REV is then:

$$\begin{cases} \mathrm{div}(\boldsymbol{\sigma}(x)) = 0 & (\Omega) \\ \boldsymbol{\sigma}(x) = \mathbb{C}(x) : \boldsymbol{\epsilon}(x) & (\Omega) \\ 2\boldsymbol{\epsilon}(x) = \Big(\nabla u(x) + \nabla^{\mathrm{T}} u(x)\Big) & (\Omega) \\ u'(x) \quad \text{periodic} & \text{(opposite boundaries)} \\ \boldsymbol{\sigma} \cdot n \quad \text{antiperiodic} & \text{(opposite boundaries)} \end{cases} \tag{4.3}$$

The first three lines represent respectively the equilibrium equations, the constitutive equations, the compatibility equations, and the last two lines the periodic boundary conditions that assume periodic displacements u' and anti-periodic tractions $\boldsymbol{\sigma} \cdot n$. The solution of this problem subsequently enables the macroscopic properties of the medium to be obtained. The macroscopic stresses $\boldsymbol{\Sigma}$ for example are computed from the spatial average of the local stress field, $\langle \boldsymbol{\sigma} \rangle = \boldsymbol{\Sigma}$, which is necessary to obtain the homogenised (or effective) constitutive matrix defined by: $\boldsymbol{\Sigma} = \mathbb{C}^{\mathrm{hom}} : \boldsymbol{E}$.

Different numerical methods can therefore be applied to solve the local problem, the most popular being the finite element method (FEM). Another method based on Fast Fourier Transforms (FFT) has also been proposed and developped in the literature. In the next sections we present the periodic homogenisation in the framework of this latter approach.

4.3 Resolution based on Fast Fourier Transforms

4.3.1 The auxiliary problem

Moulinec and Suquet (1994) proposed to rewrite the local mechanical problem by introducing a homogeneous reference material, with an elastic stiffness tensor $\mathbb{C}^0$, and a polarisation tensor $\boldsymbol{\tau}$ as follows:

$$\begin{cases} \mathrm{div}(\boldsymbol{\sigma}(x)) = 0 & (\Omega) \\ \boldsymbol{\sigma}(x) = \mathbb{C}^0 : (\boldsymbol{\epsilon}(u'(x)) + \boldsymbol{E}) + \boldsymbol{\tau}(x) & (\Omega) \\ 2\boldsymbol{\epsilon}(x) = \Big(\nabla u(x) + \nabla^{\mathrm{T}} u(x)\Big) & (\Omega) \\ u' \# & (\partial\Omega) \\ \boldsymbol{\sigma} \cdot n - \# & (\partial\Omega) \end{cases} \tag{4.4}$$

with :

$$\boldsymbol{\tau}(x) = (\mathbb{C}(x) - \mathbb{C}^0) : \boldsymbol{\epsilon}(x) \tag{4.5}$$

$(\#)$ and $(-\#)$ are shortcuts for the periodic and antiperiodic conditions on opposite boundary surfaces.

4.3.2 The periodic Lippmann-Schwinger equation

Suquet (1990) showed that the solution to this auxiliary problem can be divided into two solutions if we assume that $\boldsymbol{\tau}$ is known, those of the same problems as Eq. 4.4 but with the following constitutive relations:

$$\boldsymbol{\sigma}(x) = \mathbb{C}^0 : (\boldsymbol{\epsilon}(u'(x)) + \boldsymbol{E}) \tag{4.6a}$$

$$\boldsymbol{\sigma}(x) = \mathbb{C}^0 : (\boldsymbol{\epsilon}(u'(x))) + \boldsymbol{\tau}(x) \tag{4.6b}$$

The solution to the first problem (Eq. 4.6a as constitutive equation) is straightforward: $u'(x) = 0$. The solution to the second problem is found by expressing it as Fourier series. The displacement field u' being periodic over Ω, like any periodic function it can be expressed as:

$$u'(x) = \sum_{n=-\infty}^{+\infty} \hat{u}'(\xi_n) e^{i\xi_n \cdot x} \tag{4.7}$$

where ξ_n is the frequency or wave-vector in Fourier space, and $\hat{u}'(\xi_n)$ the corresponding Fourier coefficient defined by:

$$\hat{u}'(\xi_n) = \frac{1}{|\Omega|} \int_\Omega u'(x) e^{-i\xi_n \cdot x} \tag{4.8}$$

Replacing Eq. 4.7 in the compatibility equation of the second problem, leads to the Fourier series of the strain components $\epsilon'_{kl}(x)$, with ξ_{nk} being the components of ξ_n:

$$\epsilon'_{kl}(x) = \sum_{n=-\infty}^{+\infty} \frac{i}{2} \left(\xi_{nl} \hat{u'}_k(\xi_n) + \xi_{nk} \hat{u'}_l(\xi_n) \right) e^{i\xi_n \cdot x} \tag{4.9}$$

The fluctuating strains $\boldsymbol{\epsilon}'$ are indeed periodic and their Fourier coefficients are a function of those of u':

$$\hat{\epsilon'}_{kl}(\xi_n) = \frac{i}{2} \left(\xi_{nl} \hat{u'}_k(\xi_n) + \xi_{nk} \hat{u'}_l(\xi_n) \right) \tag{4.10}$$

A similar development of the constitutive and the equilibrium equations gives the following relations between the Fourier coefficients of the components of $\boldsymbol{\sigma}$, u' and $\boldsymbol{\tau}$ (with simplifications due to the minor symmetries of $\mathbb{C}^0$):

$$\hat{\sigma}_{ij}(\xi_n) = iC^0_{ijkl} \xi_{nl} \hat{u'}_k(\xi_n) + \hat{\tau}_{ij}(\xi_n) \tag{4.11a}$$

$$i\xi_j \hat{\sigma}_{ij}(\xi_n) = 0 \tag{4.11b}$$

Replacing Eq. 4.11a into Eq. 4.11b and introducing the acoustic tensor $K_{ik}(\xi_n) = \xi_{nj} C^0_{ijkl} \xi_{nl}$ and its inverse $\boldsymbol{N}(\xi_n) = (\boldsymbol{K}(\xi_n))^{-1}$ in Fourier space leads to the Fourier coefficients of the solution u' of the second problem linked to Eq. 4.6b:

$$\hat{u'}_k(\xi_n) = iN_{ki}(\xi_n)\xi_{nj}\hat{\tau}_{ij}(\xi_n) = \frac{i}{2} \left(N_{ki}\xi_{nj} + N_{kj}\xi_{ni} \right) \hat{\tau}_{ij}(\xi_n) \tag{4.12}$$

Finally, using the Eq. 4.10 gives the Fourier coefficients of the fluctuating strains $\boldsymbol{\epsilon}'$ associated to the solution (with minor symmetrisation), and their Fourier series:

$$\begin{aligned} \hat{\epsilon'}_{kl}(\xi_n) &= -\frac{1}{4} \left(\xi_{nl} N_{ki}(\xi_n) \xi_{nj} + \xi_{nl} N_{kj}(\xi_n) \xi_{ni} + \xi_{nk} N_{li}(\xi_n) \xi_{nj} + \xi_{nk} N_{lj}(\xi_n) \xi_{ni} \right) \hat{\tau}_{ij}(\xi_n) \\ &= -\hat{\Gamma}_{klij}(\xi_n) \hat{\tau}_{ij}(\xi_n) \end{aligned} \tag{4.13}$$

$$\epsilon'_{kl}(x) = \sum_{n=-\infty}^{+\infty} -\hat{\Gamma}_{klij}(\xi_n) \hat{\tau}_{ij}(\xi_n) e^{i\xi_n \cdot x} \tag{4.14}$$

The solution to the auxiliary problem (Eq. 4.4) is therefore obtained by adding up the solutions of the two problems introduced by Eq. 4.6a and Eq. 4.6b: it is the periodic Lippmann-Schwinger (L.-S.) equation (Moulinec and Suquet, 1994; Moulinec and Suquet, 1998), which can be written both in real and Fourier space as:

$$\boldsymbol{\epsilon}(x) = -(\boldsymbol{\Gamma} * \boldsymbol{\tau})(x) + \boldsymbol{E} \qquad (x \in \Omega) \tag{4.15}$$

$$\hat{\boldsymbol{\epsilon}}(\xi_n) = -\hat{\boldsymbol{\Gamma}}(\xi_n) : \hat{\boldsymbol{\tau}}(\xi_n) \qquad (\forall \xi_n \neq 0, \quad \hat{\boldsymbol{\epsilon}}(0) = \boldsymbol{E}) \tag{4.16}$$

where $(*)$ is the convolution product, and $\boldsymbol{\Gamma}$ is the periodic Green operator (a 4th order tensor) associated with the reference material of stiffness tensor $\mathbb{C}^0$. This equation is conveniently computed in Fourier space where the convolution product becomes a local direct product, which is why Moulinec and Suquet (1994) suggested the use of Discrete Fourier Transforms (DFT) to solve it numerically.

4.3.3 Basic scheme of resolution and discretisation

Resolution method

The L.-S. equation is actually an implicit equation as $\boldsymbol{\tau}$ depends on $\boldsymbol{\epsilon}$,

$$\boldsymbol{\epsilon}(x) = -\left(\boldsymbol{\Gamma} * \left((\mathbb{C}(x) - \mathbb{C}^0) : \boldsymbol{\epsilon}(x)\right)\right)(x) + \boldsymbol{E} \quad (x \in \Omega) \tag{4.17}$$

$$\Leftrightarrow \boldsymbol{\epsilon}(x) = F(\boldsymbol{\epsilon}(x)) \quad (x \in \Omega) \tag{4.18}$$

and ϵ appears as a fixed point of the function F. Moulinec and Suquet (1994) therefore proposed in their method called 'Basic Scheme' to solve it with a fixed-point iteration method, in which for each iteration step k:

$$\boldsymbol{\epsilon}^0(x) = E \quad (x \in \Omega) \tag{4.19}$$

$$\boldsymbol{\epsilon}^k(x) = F(\boldsymbol{\epsilon}^{k-1}(x)) \quad (x \in \Omega) \tag{4.20}$$

The convergence criterion of the algorithm of Moulinec and Suquet (1994) corresponds to the stress equilibrium condition. It is generally used by other FFT-based algorithm and the definition of the error e^k reads in real and Fourier space:

$$e^k = \frac{\left(\langle \left\| \mathrm{div}\ \boldsymbol{\sigma}^k \right\|^2 \rangle\right)^{1/2}}{\|\langle \boldsymbol{\sigma}^k \rangle\|} = \frac{\left(\langle \left\| \xi_n \cdot \hat{\boldsymbol{\sigma}}^k(\xi_n) \right\|^2 \rangle\right)^{1/2}}{\left\| \hat{\boldsymbol{\sigma}}^k(0) \right\|} < \eta \tag{4.21}$$

with η a given tolerance. Back-and-forth in Fourier space are used to compute the convolution product included in $F(\boldsymbol{\epsilon}^{k-1}(x))$ using Eq. 4.16. A schematic overview of the algorithm of the Basic Scheme is given in Fig. 4.2.

Discretisation and Discrete Fourier Transforms

However, the solution presented in the previous section involves Fourier series whose sums are infinite. In order to solve the L.-S. implicit equation numerically, Moulinec and Suquet (1994) proposed to discretise the space (elementary cell) into a regular grid of 'pixels' (2D) or 'voxels' (3D), and use DFT (computed via Fast Fourier Transforms, FFT) which allow to approximate the Fourier coefficients of a periodic function through finite sums. This means that the field functions like $\boldsymbol{\epsilon}(x)$, $\boldsymbol{\tau}(x)$, $\mathbb{C}(x)$, $\boldsymbol{\sigma}(x)$ are sampled into $N_1 \times N_2$ (or $N_1 \times N_2 \times N_3$

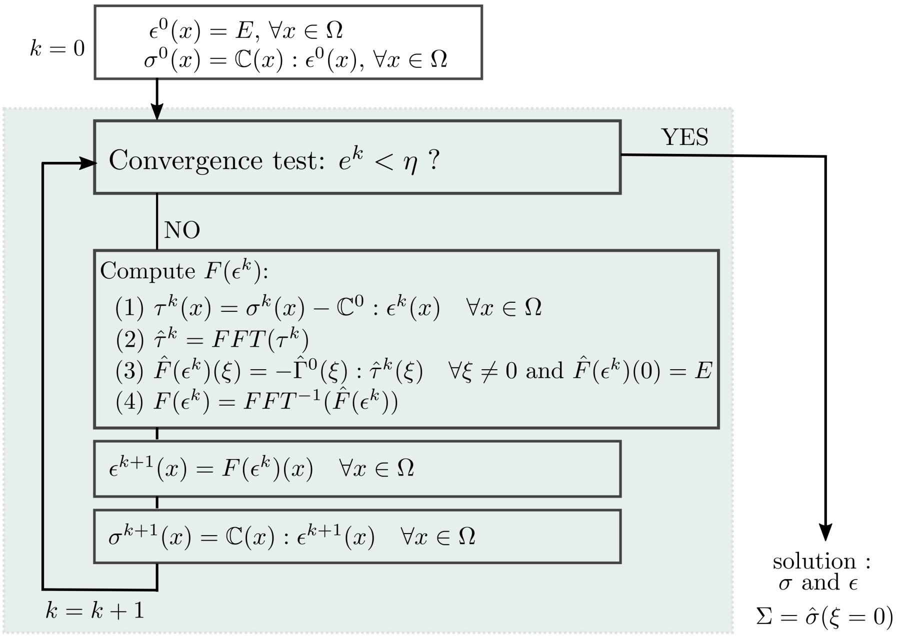

Fig. 4.2: Algorithm overview of the Basic Scheme homogenisation.

in 3D) constant values over the period $\Omega = [0, L_1] \times [0, L_2]$ (or $\Omega = [0, L_1] \times [0, L_2] \times [0, L_3]$ in 3D). The local constitutive tensor $\mathbb{C}(x)$ defines the local behaviour of each constituting phase so it is distributed over the unit cell in the range of the different material constitutive tensors of these phases (see Fig. 4.3). For example, in 2D the unit cell is discretised into $N_1 \times N_2$ pixels of size $\dfrac{L_1}{N_1} \times \dfrac{L_2}{N_2}$ whose real space coordinates are:

$$x_{ab} = \left(\frac{aL_1}{N_1}, \frac{bL_2}{N_2}\right) \qquad (a, b) \in [\![0; N_1[\![\times [\![0; N_2[\![\tag{4.22}$$

and the corresponding discrete frequencies in Fourier space are:

$$\xi_{AB} = \left(\frac{2\pi A}{L_1}, \frac{2\pi B}{L_2}\right) (A, B) \in \left]\!\!\left] \frac{-N_1}{2}; \frac{N_1}{2} \right]\!\!\right] \times \left]\!\!\left] \frac{-N_2}{2}; \frac{N_2}{2} \right]\!\!\right] \tag{4.23}$$

A sampled tensor $\boldsymbol{T}(x)$ is a pixel-wise constant tensor defined by:

$$\boldsymbol{T}(x) = \boldsymbol{T}_{ab} \quad \text{if} \begin{cases} \dfrac{aL_1}{N_1} \leqslant x \leqslant \dfrac{(a+1)L_1}{N_1} \\ \dfrac{bL_2}{N_2} \leqslant y \leqslant \dfrac{(b+1)L_2}{N_2} \end{cases} \qquad (a, b) \in [\![0; N_1[\![\times [\![0; N_2[\![\tag{4.24}$$

The real sequence $\{\boldsymbol{T}_{ab}\}_{(a,b) \in [\![0; N_1[\![\times [\![0; N_2[\![}$ is converted by the following DFT into a new one $\{\hat{\boldsymbol{T}}_{AB}\}_{(A,B) \in]\!] -\frac{N_1}{2}; \frac{N_1}{2}]\!] \times]\!] -\frac{N_2}{2}; \frac{N_2}{2}]\!]}$ in Fourier space:

$$\hat{\boldsymbol{T}}_{AB} = \sum_{a=0}^{N_1-1} \sum_{b=0}^{N_2-1} \boldsymbol{T}_{ab} \cdot e^{-i2\pi \left(\dfrac{aA}{N_1} + \dfrac{bB}{N_2}\right)} \tag{4.25}$$

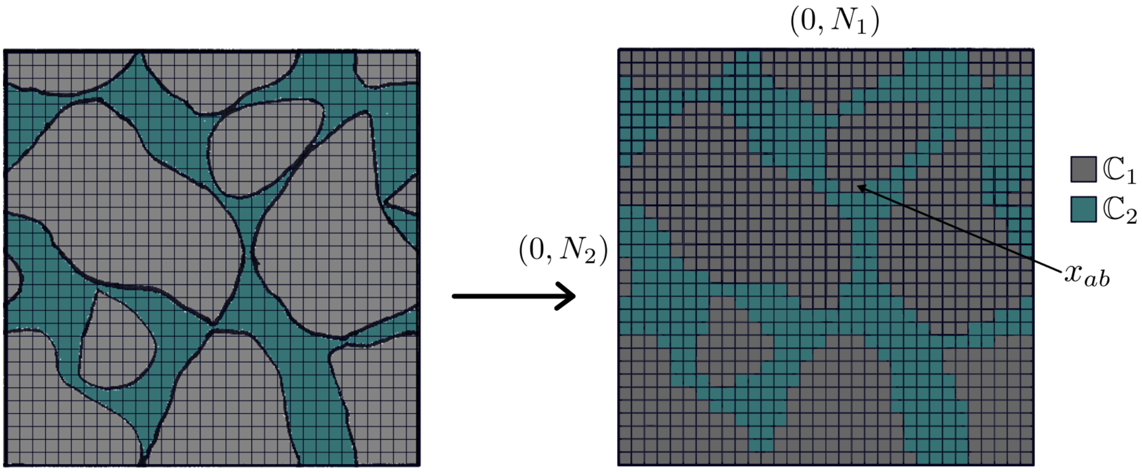

Fig. 4.3: Example of a 2D unit cell discretisation in $N_1 \times N_2$ pixels, with two independent constituting phases for FFT-based homogenisation.

The inverse DFT is also defined:

$$\boldsymbol{T}_{ab} = \frac{1}{N_1 N_2} \sum_{A=0}^{N_1-1} \sum_{B=0}^{N_2-1} \hat{\boldsymbol{T}}_{AB} \cdot e^{i2\pi\left(\frac{aA}{N_1}+\frac{bB}{N_2}\right)} \tag{4.26}$$

Moulinec and Suquet (1994) use the resulting components $\hat{\boldsymbol{T}}_{AB}$ of the DFT as an approximation of the Fourier coefficient of the continuous field $\boldsymbol{T}$: $\hat{\boldsymbol{T}}(\xi_{AB}) \simeq \hat{\boldsymbol{T}}_{AB}$. In the computation of $F(\boldsymbol{\epsilon}^{k-1}(x))$ the discrete polarisation tensor expression $\boldsymbol{\tau}^{k-1}_{ab} = (\mathbb{C}_{ab} - \mathbb{C}^0) : \boldsymbol{\epsilon}^{k-1}_{ab}$ is calculated in real space, then FFT algorithms are used to obtain $\hat{\boldsymbol{\tau}}^{k-1}_{AB}$ and evaluate

$$\hat{\boldsymbol{\epsilon}}^k_{AB} = -\hat{\boldsymbol{\Gamma}}(\xi_{AB}) : \hat{\boldsymbol{\tau}}^{k-1}_{AB} \quad (\forall \xi_{AB} \neq 0, \quad \hat{\boldsymbol{\epsilon}}(0)^k = \boldsymbol{E}) \tag{4.27}$$

Finally, Moulinec and Suquet (1994) compute the real sequence of strains

$$\{\boldsymbol{\epsilon}^k_{ab}\}_{(a,b)\in\llbracket 0;N_1\llbracket\times\llbracket 0;N_2\llbracket}$$

via the backward FFT of the sequence $\{\hat{\boldsymbol{\epsilon}}^k_{AB}\}_{(A,B)\in\rrbracket -\frac{N_1}{2};\frac{N_1}{2}\rrbracket\times\rrbracket -\frac{N_2}{2};\frac{N_2}{2}\rrbracket}$.

Periodic Green's operator for an isotropic linear elastic reference material

They use the case of an isotropic reference material, where $\mathbb{C}^0$ is defined by the Lamé coefficients λ^0 and μ^0 for example, and the expression of the Fourier coefficients of Green operator is (see Eq. 4.13):

$$\hat{\Gamma}^0_{ijkl}(\xi) = \frac{1}{4\mu^0\,|\xi|^2}\left(\delta_{ki}\xi_l\xi_j + \delta_{li}\xi_k\xi_j + \delta_{kj}\xi_l\xi_i + \delta_{lj}\xi_k\xi_i\right) - \frac{\lambda^0+\mu^0}{\mu^0\,(\lambda^0+2\mu^0)}\frac{\xi_i\xi_j\xi_k\xi_l}{|\xi|^4} \tag{4.28}$$

for $\xi \neq 0$. This expression is valid both in 2D and 3D. There is a special treatment at the highest frequencies (Moulinec and Suquet, 1998; Willot, 2015) when the number of pixels or voxels in one direction is even (N_1 and/or N_2 is even in 2D for example), if one of the components of ξ is $\xi_k = \pi$ ($A = \frac{N_1}{2}$, or $B = \frac{N_2}{2}$ in 2D for example), then:

$$\hat{\Gamma}^0(\xi) = (\mathbb{C}^0)^{-1} \tag{4.29}$$

4.3.4 FFT-based method for nonlinear behaviour

Different homogenisation methods have been developped based on the use of FFT and the discretisation introduced by Moulinec and Suquet (1994). The advantages of the basic scheme is the simplicity of the algorithm, the fact that no mesh is required and that images of complex microstructures can be used. However, the fixed point iteration method is not the fastest one, it does not converge for infinite contrast between phases of the microstructure and there is a strong dependency of the convergence on the choice of the reference material, more precisely on the choice of $\mathbb{C}^0$. This is why some authors have tried to improve the basic scheme with other approaches, among which we can cite the augmented lagrangian method (Michel et al., 2000), the accelerated scheme (Eyre and Milton, 1999), or FFT-based approaches accelerated by conjugate gradient methods proposed by Brisard and Dormieux (2010) and Zeman et al. (2010).

Iterative Conjugate Gradient (CG) methods

The principle of the CG methods is the following: solving linear equations like $\boldsymbol{A}x = b$, with $\boldsymbol{A}$ a symmetric and positive-definite matrix, is equivalent to minimising the function:

$$\phi(x) = \frac{1}{2}x^T\boldsymbol{A}x - b^Tx \tag{4.30}$$

as $\nabla\phi(x) = \boldsymbol{A}x - b$, and $\nabla^2\phi(x) = \boldsymbol{A}$ which (given the properties of $\boldsymbol{A}$) implies a unique minimiser. The classic gradient descent methods minimise functions by chosing a descent direction (vector $p^{(k)} \in \mathbb{R}^n$ such that $p^{(k)T} \cdot \nabla\phi(x^k) < 0$) to move closer to the solution x_* at each step k. The steepest slope at a given step point x^k is the opposite of the gradient $\nabla\phi(x^k)$ and corresponds to the residu $r^k = b - \boldsymbol{A}x^k$. The next step point x^{k+1} is obtained by minimising ϕ along the direction $p^{(k)}$ passing through x^k:

$$x^{k+1} = x^k + \alpha_k p^{(k)} \quad \text{with } \alpha_k \text{ such that: } \phi(x^{k+1}) = \min_{\alpha\in\mathbb{R}} \phi(x^k + \alpha_k p^{(k)}) \tag{4.31}$$

In the CG method $p^{(k)}$ depends on the previous descent directions

$$\{p^{(0)}, p^{(1)}, \ldots, p^{(k-1)}\}$$

and on the current residu r^k

$$p^{(k)} = \begin{cases} r^{(0)} & \text{if } k = 0 \\ r^{(k)} + \beta_k p^{(k-1)} & \text{if } k \geqslant 1 \end{cases}, \text{ with } \beta_k \text{ such that } p^{(k)T} \boldsymbol{A} p^{(k-1)} = 0 \tag{4.32}$$

The condition $p^{(k)T} \boldsymbol{A} p^{(k-1)} = 0$ means that $p^{(k)}$ and $p^{(k-1)}$ are conguate with respect to $\boldsymbol{A}$, so all the directions $p^{(k)}$ are conjugate directions. Moreover, as a starting point, the first direction is taken equal to the gradient $p^{(0)} = r^{(0)} = -\nabla\phi(x^0)$. Therefore, all the directions $p^{(k)}$ are conjugate to the gradient, which explains the name conjugate gradient method. In this condition, it can be shown that the expressions of the coefficients α_k and β_k are:

$$\alpha_k = \frac{r^{(k)T} p^{(k)}}{p^{(k)T} \boldsymbol{A} p^{(k)}} \tag{4.33}$$

$$\beta_k = \frac{r^{(k+1)T} r^{(k+1)}}{r^{(k)T} r^{(k)}} \tag{4.34}$$

It can be seen from the previous equations that in the conjugate gradient methods the matrix $\boldsymbol{A}$ never needs to be computed, or inverted, we only need the computation of the product $\boldsymbol{A} \cdot y$. This kind of iterative method is usually applied to large sparse systems as it is the case with FFT-based homogenisation schemes that involve images of high resolution, and large systems of equations to solve.

Combined Newton-Raphson and CG method

Moulinec and Suquet adapted their Basic Scheme algorithm to solve cases where the local constitutive laws are nonlinear ones, that is, nonlinear elastic laws, viscous or plastic incremental laws (Moulinec and Suquet, 1998). The loading path $\boldsymbol{E}$ is discretised with the time interval $[0;T]$ over which it is applied

$$[0;T] = \sum_{n=0}^{N-1} [t_n; t_{n+1}], \quad \{t_0 = 0, t_N = T\} \tag{4.35}$$

$$\boldsymbol{E} = \sum_{n=0}^{N-1} (\boldsymbol{E}_{n+1} - \boldsymbol{E}_n), \quad \{\boldsymbol{E}_0 = 0, \boldsymbol{E}_N = \boldsymbol{E}\} \tag{4.36}$$

with $\boldsymbol{E}_n = \boldsymbol{E}(t_n)$. The Basic Scheme is applied to find the values of strains $\boldsymbol{\epsilon}_{n+1}$ at each time step under the loading $\boldsymbol{E}_{n+1}$. For nonlinear local constitutive laws,

$$(\boldsymbol{\sigma}_{n+1}, p_{n+1}) = \mathrm{F}(\boldsymbol{\epsilon}_{n+1}, \boldsymbol{\sigma}_n, \boldsymbol{\epsilon}_n, p_n) \tag{4.37}$$

the stresses $\boldsymbol{\sigma}_{n+1}$ and internal variables p_{n+1} at t_{n+1} can be evaluated with the help of classic time integration approaches such as the return mapping or the substepping approach (Potts and Zdravkovic, 1999) whose principle are reminded in Fig. 4.4.

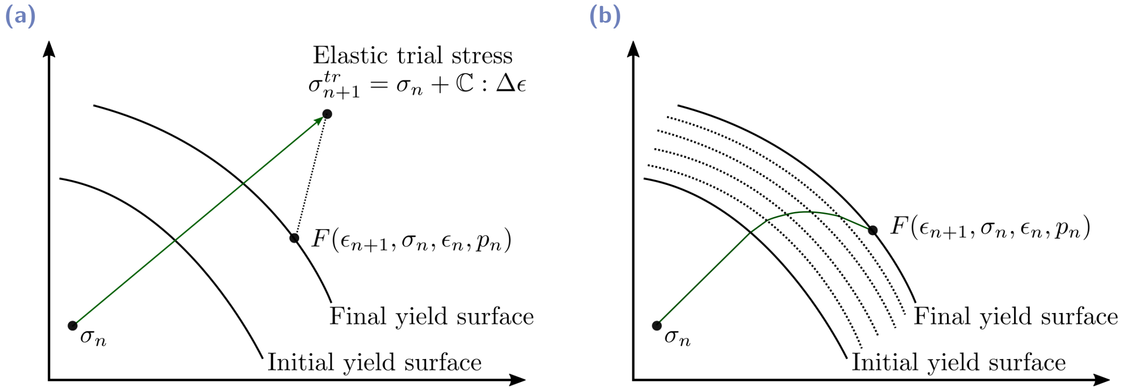

Fig. 4.4: Schematic Representation of the (a) return mapping and (b) substepping algorithms for stress integration (from Potts and Zdravkovic, 1999).

The method we chose to adopt here differs from Moulinec and Suquet original resolution scheme and has been developped by Gélébart and Mondon-Cancel (2013) who used conjugate gradient based solvers like Brisard and Dormieux (2010) and Zeman et al. (2010). It makes use of a general Newton-Raphson (NR) algorithm to solve the L.-S. equation (Eq. 4.17) with the following residu, t denoting the time variable:

$$\mathcal{G}(\boldsymbol{\epsilon}(t)) = \boldsymbol{\epsilon}(t) + \mathit{\Gamma} * (\boldsymbol{\sigma}(t) - \mathbb{C}^0 : \boldsymbol{\epsilon}(t)) - \boldsymbol{E}(t) \tag{4.38}$$

Non-linear constitutive laws can be distributed over the unit-cell, depending on the local constituents. The stresses and internal variables need to be integrated over time increments $\mathit{\Delta} t = t_n - t_{n-1}$, as functions of the previous state. The Jacobian matrix $\dfrac{\partial \mathcal{G}}{\partial \boldsymbol{\epsilon}}(\boldsymbol{\epsilon}(t_n))$ is not given since the residual differentiation includes a convolution product, but the linearised problem in the NR algorithm is fully expressed as follows:

$$\frac{\partial \mathcal{G}}{\partial \boldsymbol{\epsilon}}(\boldsymbol{\epsilon}(t_n)) : \delta\boldsymbol{\epsilon} = -\mathcal{G}(\boldsymbol{\epsilon}(t_n)) \Longleftrightarrow \delta\boldsymbol{\epsilon} + \mathit{\Gamma} * ((\mathbb{C}^* - \mathbb{C}^0) : \delta\boldsymbol{\epsilon}) = -\mathcal{G}(\boldsymbol{\epsilon}(t_n)) \tag{4.39}$$

$$\Longleftrightarrow \mathcal{B}_{\mathbb{C}^*}(\delta\boldsymbol{\epsilon}) = -\mathcal{G}(\boldsymbol{\epsilon}(t_n)) \tag{4.40}$$

and solved by a CG method to find $\delta\boldsymbol{\epsilon}$ and update the strains at iteration k:

$$\boldsymbol{\epsilon}(t_n)^k = \boldsymbol{\epsilon}(t_n)^{k-1} + \delta\boldsymbol{\epsilon} \tag{4.41}$$

$\mathbb{C}^*$ is the local 'tangent stiffness matrix':

$$\mathbb{C}^* = \frac{\partial \boldsymbol{\sigma}(t_n)}{\partial \boldsymbol{\epsilon}}(\boldsymbol{\epsilon}(t_n)) \tag{4.42}$$

and depends on the local constitutive law. The convergence criterion used in the NR algorithm is the stress equilibrium condition evaluated in Fourier space at each iteration

(Moulinec and Suquet, 1998; Gélébart and Mondon-Cancel, 2013), with an error $e(t_n)$ similar to the one of Eq. 4.21:

$$e(t_n) = \frac{(\langle \|\mathrm{div}(\boldsymbol{\sigma}(t_n))\|^2 \rangle)^{1/2}}{\|\langle \boldsymbol{\sigma}(t_n) \rangle\|} < \eta. \tag{4.43}$$

In our calculations the CG-based solver comes from the PETSc library (Balay et al., 2019), and the convergence criterion given by Eq. 4.44 is applied outside the framework of the library, in addition to its internal one. This internal criterion is the same equilibrium condition as the one given in equation 4.43 but evaluated for the tangential stresses that are extrapolated from the CG loop solution (Gélébart and Mondon-Cancel, 2013).

$$\boldsymbol{\sigma}^{CG} = \boldsymbol{\sigma}(t_{n-1}) + \mathbb{C}^* : \delta\boldsymbol{\epsilon} \tag{4.44}$$

The computation of the residual $-\mathcal{G}(\boldsymbol{\epsilon}(t_n))$ and the product $\frac{\partial \mathcal{G}}{\partial \boldsymbol{\epsilon}}(\boldsymbol{\epsilon}(t_n)) : \delta\boldsymbol{\epsilon}$ in Eq. 4.39 is based on the same principle of discretisation as presented for the Basic Scheme and the back-and-forth in Fourier space using FFT. The time dependent stresses and internal variables are also evaluated following classic time integration approaches (see Fig. 4.4). For each time step t_n the initial guess for the strain $\boldsymbol{\epsilon}_n$ is an extrapolation from the previous ones over the unit cell:

$$\boldsymbol{\epsilon}_n^0(x) = \boldsymbol{\epsilon}_{n-1}(x) + \frac{t_n - t_{n-1}}{t_{n-1} - t_{n-2}} (\boldsymbol{\epsilon}_{n-1}(x) - \boldsymbol{\epsilon}_{n-2}(x)) \tag{4.45}$$

Unlike the Basic Scheme, the combination of the NR and CG-based methods used by Gélébart and Mondon-Cancel (2013) to solve the L.-S. equation allows for infinite stiffness contrasts between constituting phases. This is particularly interesting for applications to the effective behaviour of gas hydrate bearing sediments as we saw in section 2 that these soils can be of granular nature and include voids. In these soils, gas hydrate crystals, quartz grains and voids thus have strongly contrasted stiffness moduli.

4.3.5 Green operator

The periodic Green operator $\hat{\Gamma}^0$ employed in the Basic Scheme and other methods is truncated to the low frequencies (Brisard and Dormieux, 2010). This has some consequences on the results of the FFT-based homogenisation algorithms, especially on the local mechanical fields accuracy (Willot and Pellegrini, 2008; Willot, 2015). Other Green operators have also been introduced by authors like Brisard and Dormieux (2010) and Willot and Pellegrini (2008) in order to improve the numerical resolution.

In addition to the Green operator proposed by Moulinec and Suquet (1994) in the Basic Scheme, three other ones were proposed by Willot (2015). These operators are developped

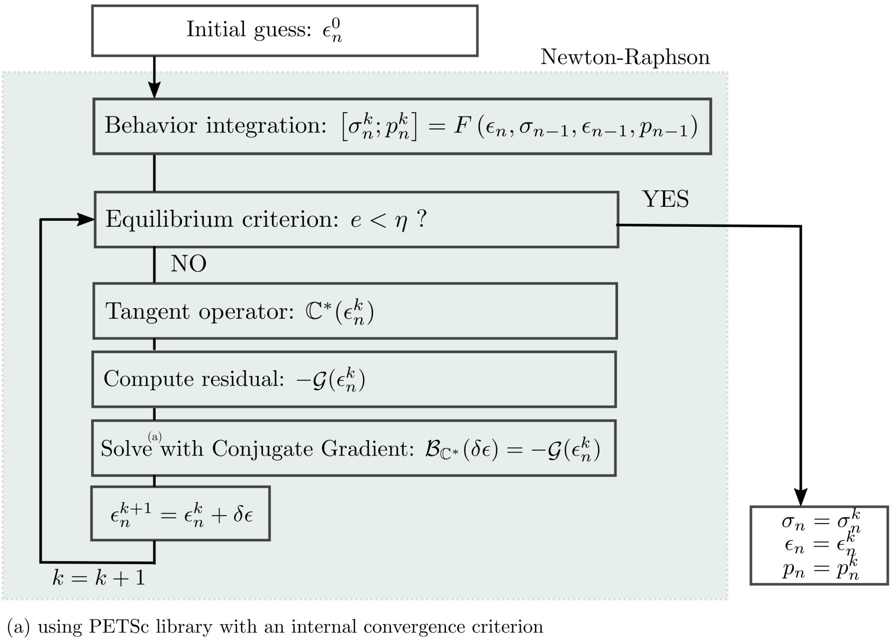

Fig. 4.5: Algorithm overview of Gélébart and Mondon-Cancel (2013) homogenisation method.

in the framework of finite differences. The local equations of equilibrium and compatibility are approximated by finite differences and DFT to define new operators.

With $v_j, j \in \{1,2\}$ in 2D, or $j \in \{1,2,3\}$ in 3D, being basis vectors in cartesian coordinates, Willot (2015) proposed:

- a centered difference scheme as follows,

$$\sigma_{ij,j} \approx \frac{\sigma_{ij}(x+v_j) - \sigma_{ij}(x-v_j)}{2} \tag{4.46}$$

$$\epsilon_{ij} \approx \frac{[u_i(x+v_j) - u_i(x-v_j)] + [u_j(x+v_i) - u_j(x-v_i)]}{4} \tag{4.47}$$

- a forward-and-backward difference scheme,

$$\sigma_{ij,j} \approx \sigma_{ij}(x) - \sigma_{ij}(x-v_j) \tag{4.48}$$

$$\epsilon_{ij} \approx \frac{[u_i(x+v_j) - u_i(x)] + [u_j(x+v_i) - u_j(x)]}{2} \tag{4.49}$$

- an original scheme where centered differences are used in a 45°-rotated basis to approximate the strain field and the divergence of the stress field. Strains and stresse are

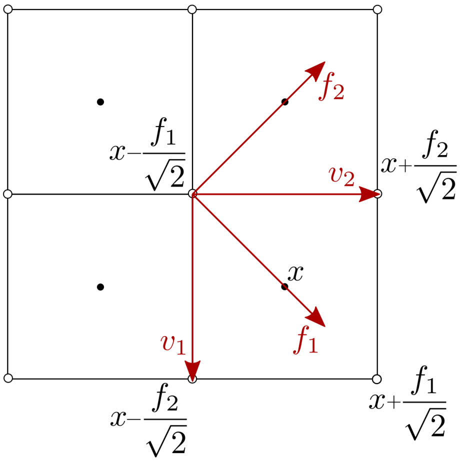

Fig. 4.6: The 2D cartesian (v_1, v_2) basis and 45°-rotated (f_1, f_2) basis used in the rotated scheme of integration defined by Willot (2015). Displacement and divergence of stress vectors are evaluated at the corners of each pixel (open circles). Strain and stress fields are evaluated at the centre of pixels (black disks).

evaluated at the centre of the pixels whereas displacements and stress divergence are evaluated at the corners (see Fig. 4.6). This can be written in 2D,

$$\sigma_{IJ,J} \approx \left[\frac{\sigma_{I1}(x) - \sigma_{I1}\left(x - \sqrt{2} f_1\right)}{\left\| \sqrt{2} f_1 \right\|} + \frac{\sigma_{I2}\left(x + \frac{f_2 - f_1}{\sqrt{2}}\right) - \sigma_{I2}\left(x - \frac{f_2 + f_1}{\sqrt{2}}\right)}{\left\| \sqrt{2} f_2 \right\|} \right] \tag{4.50}$$

$$\epsilon_{IJ} \approx \frac{1}{2} \left[\frac{u_I\left(x + \frac{f_J}{\sqrt{2}}\right) - u_I\left(x - \frac{f_J}{\sqrt{2}}\right)}{\left\| \sqrt{2} f_J \right\|} + \frac{u_J\left(x + \frac{f_I}{\sqrt{2}}\right) - u_J\left(x - \frac{f_I}{\sqrt{2}}\right)}{\left\| \sqrt{2} f_I \right\|} \right] \tag{4.51}$$

and a similar expression can be extended to 3D (Willot, 2015).

DFT are then applied to these expressions to get the following form of the equilibrium and compatibility equations in Fourier space, similar to Eq. 4.10 and Eq. 4.11b:

$$k_i^*(\xi_{AB})\hat{\sigma}_{(AB)ij} = 0 \tag{4.52}$$

$$\hat{\epsilon}_{(AB)ij} = \frac{1}{2}\left[k_i(\xi_{AB})u_{(AB)j} + k_j(\xi_{AB})u_{(AB)i}\right] \tag{4.53}$$

for $(A, B) \in \rrbracket \frac{-N_1}{2}; \frac{N_1}{2} \rrbracket \times \rrbracket \frac{-N_2}{2}; \frac{N_2}{2} \rrbracket$. The same discretisation of Fourier space as the one of section 4.3.3 is used here, k is the discrete gradient operator while k^*, its complex conjugate, is the discrete divergence operator. For each of the three finite difference schemes Willot (2015) found the following expressions (in 3D) of k:

- centered difference scheme

$$k_j^C(\xi_{AB}) = i \sin(\xi_{(AB)j}) \tag{4.54}$$

- forward-and-backward scheme

$$k_j^W(\xi_{AB}) = e^{i\xi_{(AB)j}} - 1 \tag{4.55}$$

- rotated centered difference scheme

$$k_j^R(\xi_{AB}) = \frac{i}{4}\tan\left(\frac{\xi_{(AB)j}}{2}\right)\left(1+e^{i\xi_{(AB)1}}\right)\left(1+e^{i\xi_{(AB)2}}\right)\left(1+e^{i\xi_{(AB)3}}\right) \tag{4.56}$$

These operators were then used to compute the new discrete Green operators of Willot following the similar expression as Eq. 4.13:

$$\begin{aligned}\hat{\Gamma}_{ijkl}(\xi_{AB}) =& \frac{1}{4}\Big[k_i(\xi_{AB})N'_{jk}(\xi_{AB})k_l^*(\xi_{AB}) + k_i(\xi_{AB})N'_{jl}(\xi_{AB})k_k^*(\xi_{AB}) \\ &+ k_j(\xi_{AB})N'_{ik}(\xi_{AB})k_l^*(\xi_{AB}) + k_j(\xi_{AB})N'_{il}(\xi_{AB})k_k^*(\xi_{AB})\Big]\end{aligned} \tag{4.57}$$

with $N'(\xi_{AB}) = K'^{-1}(\xi_{AB})$, and $K'_{ij}(\xi_{AB}) = k_m^*(\xi_{AB})\mathbb{C}^0_{mijn}k_n(\xi_{AB})$. We implemented in our code the discrete Green operators of Willot $\hat{\boldsymbol{\Gamma}}^C$, $\hat{\boldsymbol{\Gamma}}^W$, and $\hat{\boldsymbol{\Gamma}}^R$ associated with k^C, k^W, and k^R respectively, in addition to the classic Green operator $\hat{\Gamma}^0$ of Moulinec and Suquet (1994).

4.3.6 Code implementation

The code has been implemented in C and with the help of open source librairies:

- fftw3 (Frigo and Johnson, 2005) for the backaward and forward Fast Fourier Transforms in the algorithm,

- PETSc (Balay et al., 2019) for the iterative conjugate gradient solver, more precisely we used the Stabilised version of the BiConjugate Gradient method (BCGS).

One particularity of using FFT in homogenisation is the required memory space as we have at least four mechanical second order tensors, $\boldsymbol{\epsilon}$ and $\boldsymbol{\sigma}$ at current and previous time steps, and a fourth order tensor $\boldsymbol{\Gamma}$ to store for each pixel. The use of in-place FFT or the symmetry of the Fourier transform of real data allowed for some optimisations.

In order to take into acount the nonlinear behaviour, and in particular the plastic behaviour, of some constituents, we used the Drucker-Prager criterion or Modified Mohr-Coulomb model. The return-mapping algorithms used for Drucker-Prager and CamClay models are the ones already implemented in the open source finite element code developped in the laboratory called Bil (Dangla, 2017).

The case of uniform macroscopic strain load in homogenisation has been presented in the previous sections but some authors proposed algorithms to solve a periodic homogenisation problem with a uniform stress load (Moulinec and Suquet, 1998; Gélébart and Mondon-Cancel, 2013). We also implemented the extension of the method to stress and mixed loadings developped by Gélébart and Mondon-Cancel (2013). The case of macroscopic strain load is particularly suitable for the multiscale approaches, as the incremental strains at the macroscopic scale become the uniform load input at the microscopic scale in order to solve the local problem and obtain the resulting macroscopic stress increments. The stress and mixed loadings though, are of interest for the development of macroscopic constitutive laws where one can reproduce laboratory experimental conditions, like triaxial conditions for instance.

4.4 Comparison of Finite Elements and FFT Methods

In this section, in order to validate our FFT-based homogenisation code, we compared it to the finite element code developped in the laboratory called Bil (Dangla, 2017). The first homogenisation calculations were performed on a simple 3D geometry, a spherical elastic inclusion embedded in an elastic matrix, for which the analytical solution is known. The case of a void inclusion was also investigated. Then, the same geometry was used in plasticity, the behaviour of the elastic inclusion remaining elastic and the matrix becoming plastic this time. This allowed us to validate our FFT-based homogenisation code.

4.4.1 Elasticity

A simple 2D geometry for the microstructure was first introduced to compare the results of the FEM and the FFT-based codes. We used the case of isotropic elastic circular inclusions embedded in an isotropic elastic matrix. The input parameters for the matrix and the inclusion phase are summarised in Tab. 4.1. The periodic microstructure is defined by $\Omega = [0;1] \times [0;1]$ and discretised into $N_1 \times N_2$ pixels for the FFT homogenisation. The radius of the inclusion is $R = 0.25$. We examined several microstructure discretisations by varying the pixel resolution $N1$ (here $N1 = N2$) for FFT-based calculations, and various triangular mesh refinements (using Gmsh software, Geuzaine and Remacle, 2009) for the FEM. The unit cell was subjected to plane strain simple shear and biaxial compression macroscopic loadings with the corresponding 2D macroscopic uniform strain loads:

$$E_{12} = E_{21} = 1\%, \quad E_{11} = E_{22} = 0 \tag{4.58}$$

$$E_{11} = E_{22} = 1\%, \quad E_{12} = E_{21} = 0 \tag{4.59}$$

The tolerance of the FFT-based code was set to $\eta = 10^{-7}$, and the Green operator was $\boldsymbol{\Gamma}^0$ for these first results. The influence of the latter parameter will be shown later in the section.

Tab. 4.1: Parameters of the two-phase microstructure used for the elastic homogenisation calculations.

Phase	Young modulus	Poisson's ratio
matrix	$E_m = 2.67\text{GPa}$	$\nu_m = 0.33$
inclusion	$E_i = 13.33\text{GPa}$	$\nu_i = 0.33$

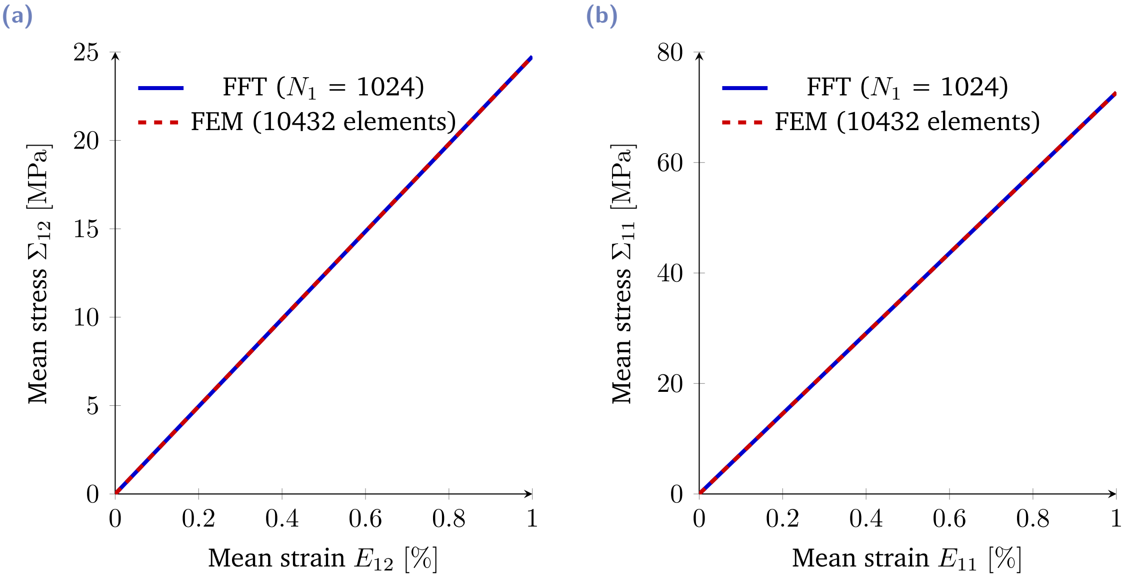

Fig. 4.7: Comparative results between FFT-based and FEM homogenisation of an elastic circular inclusion submitted to a plane strain (a) shearing and (b) biaxial compression macroscopic loading.

The homogenised stress strain responses to the shearing and the biaxial loading are plotted in Fig. 4.7 for the two codes at fine discretisation. The FFT-based homogenised results are the same as the ones computed with the FEM. The convergence of FEM simulations was assessed by comparing the obtained results of multiple refined meshes (Fig. 4.8.b). Moreover, the results converge quickly, and from a resolution of 32x32 pixels the resulting curves in Fig. 4.8.a no longer vary.

The interest of the Gélébart and Mondon-Cancel (2013) method that we have included in our house code is that it allows to perform calculations for high stiffness contrasts and even infinite contrasts. Indeed, among the types of gas hydrate bearing soils generally encountered, some granular soils present this particularity of high contrast between the moduli of sand grains, hydrate phase and voids for the homogenisation of the effective mechanical properties. We tested the elastic circular inclusion used previously for different stiffness contrasts $c = E_i/E_m$, and for a void inclusion under the same macroscopic loadings as Eq. 4.58 and Eq. 4.59. Again the results correspond between FEM and FFT-based homogenisations (Fig. 4.9), but the responses are more influenced by the resolution of the input geometry (Fig. 4.10) than with the previous ratio of $c = 5$.

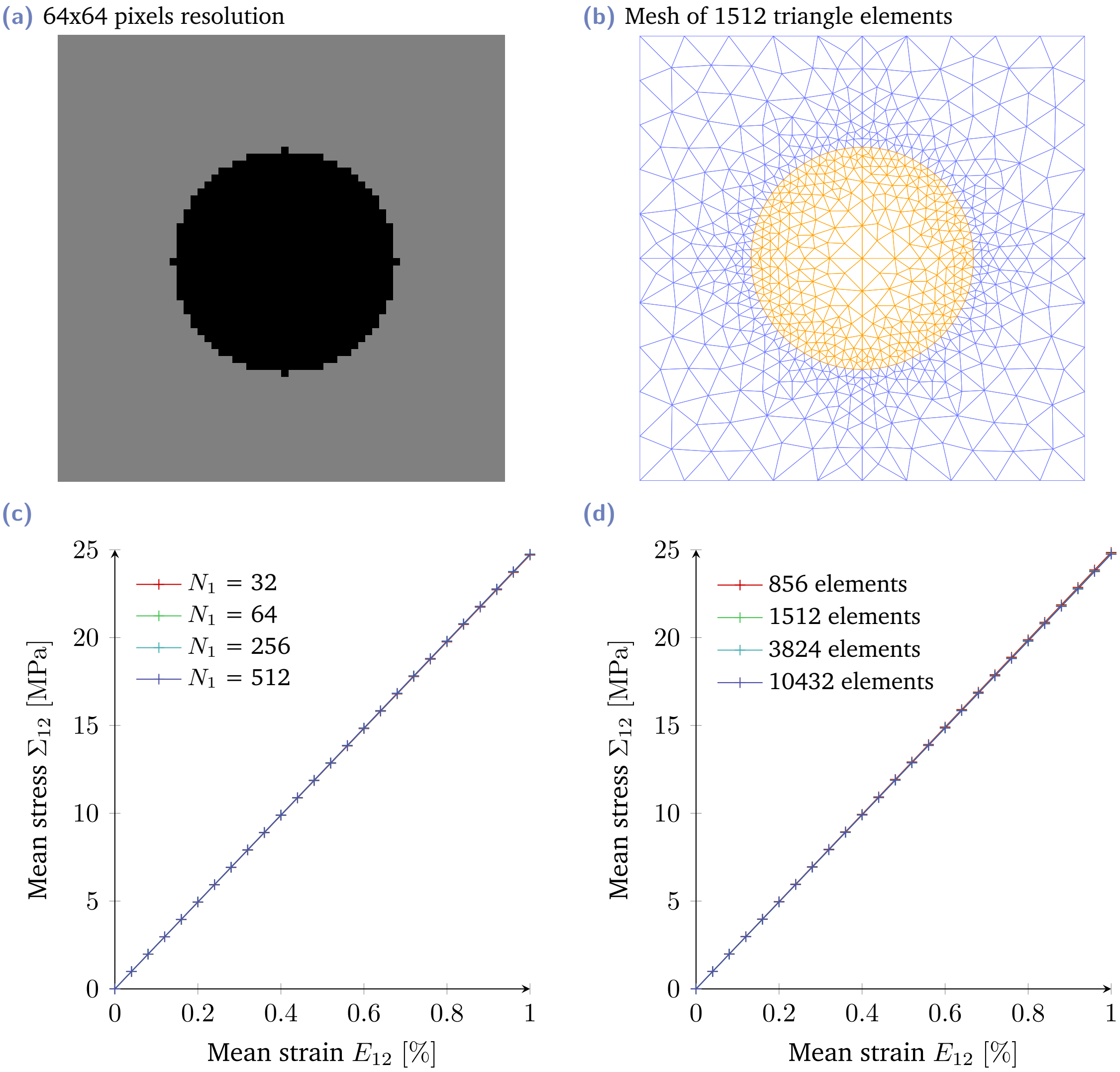

(a) 64x64 pixels resolution

(b) Mesh of 1512 triangle elements

Fig. 4.8: Results of (c) FFT-based and (d) FEM homogenisation of an elastic circular inclusion at different resolutions or mesh refinements for the macroscopic shear loading. Examples of space discretisation used are given in (a) and (b).

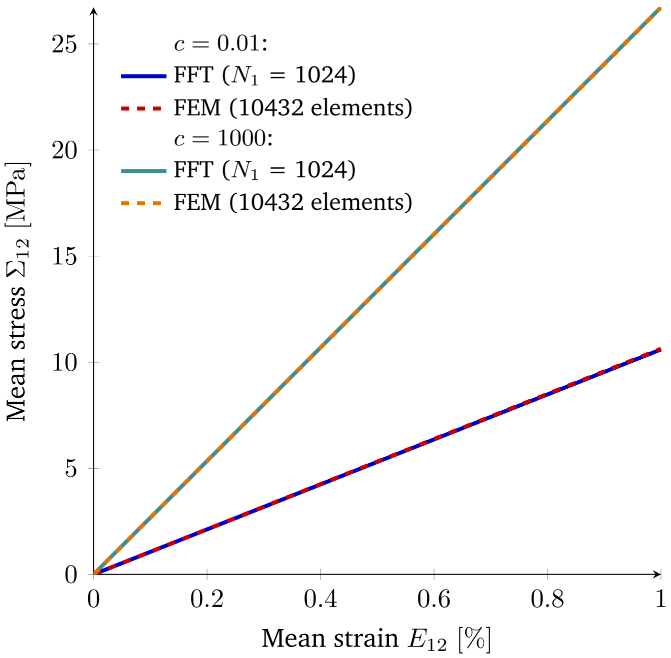

Fig. 4.9: Comparative results between FFT-based and FEM homogenisation of an elastic circular inclusion submitted to a simple macroscopic shearing for different stiffness contrasts: $c = 0.01$ and $c = 1000$.

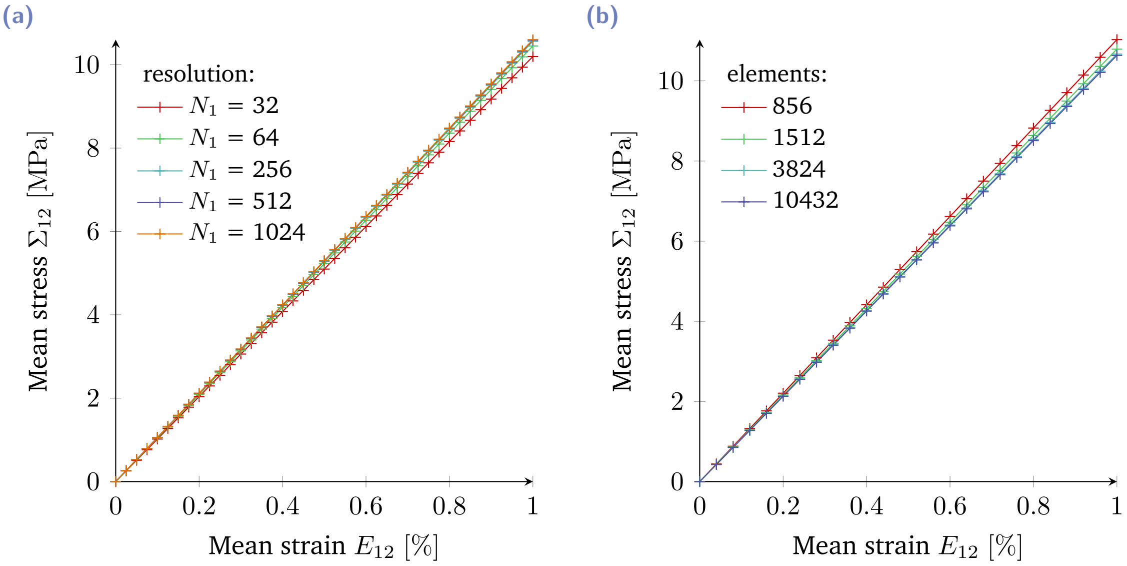

Fig. 4.10: Results of (a) FFT-based and (b) FEM homogenisation of an elastic circular inclusion at different resolutions or mesh refinements for the macroscopic shear loading, for a stiffness contrast $c = 0.01$.

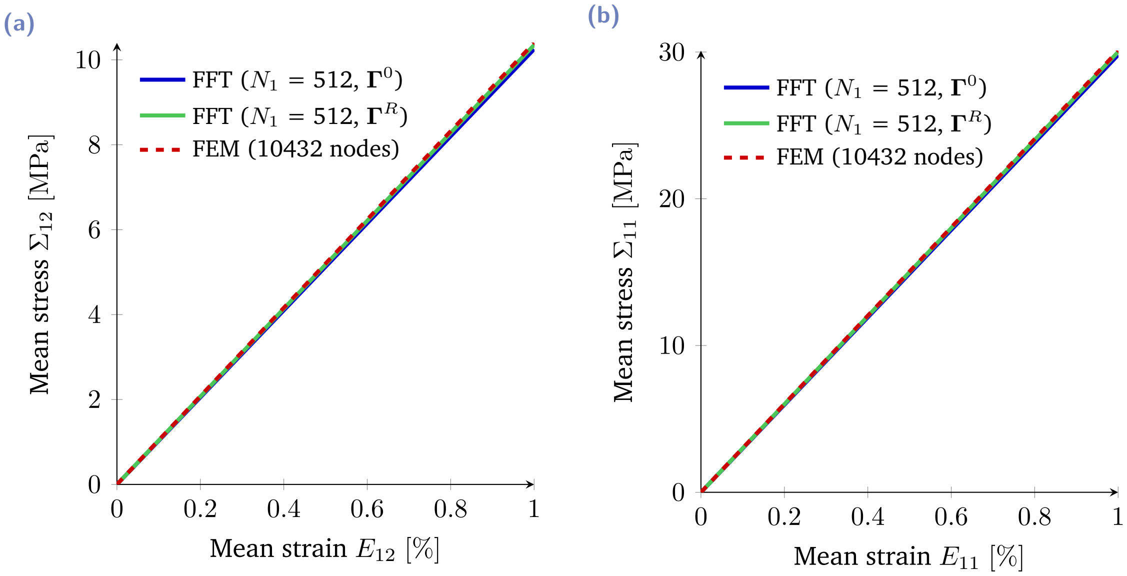

Fig. 4.11: Comparative results between FFT-based and FEM homogenisation of a void inclusion submitted to a plane strain (a) shearing and (b) biaxial compression macroscopic loading.

For the void inclusion the comparative results are shown in Fig. 4.11 for fine given space discretisations, and the responses to the shear and compression loadings are in good agreement. The results of homogenisation using both the truncated Green operator $\boldsymbol{\Gamma}^0$ and the rotated operator from Willot (2015) $\boldsymbol{\Gamma}^R$ are also presented. Fig. 4.12 represents the distributions of the stress component σ_{12} over the geometry of the microstructure (FE mesh and pixelised image) at the end of the macroscopic shearing as an example.

Looking at the results obtained with the FFT-based homogenisation, one can see that the stress component is indeed null inside the inclusion. In the FEM the void inclusion has simply not been meshed here. The comparison between the results obtained with the FEM and the FFT-based method with the rotated Green tensor is conclusive. Differences appear when using the truncated Green operator even though the macroscopic responses obtained with the two Green operators in Fig. 4.11 were comparable. When zooming in the stress distribution we can observe oscillations in the results computed with the truncated Green operator $\boldsymbol{\Gamma}^0$. This phenomenon has already been described by Willot (2015), as well as the slower convergence obtained with the Green operator compared to finite differences operators like $\boldsymbol{\Gamma}^R$. We discovered that for high resolution or finner discretisation of the microstructure geometry as well as for high stiffness contrasts, the FFT-based homogenisation computation seem faster than the FEM homogenisation (Fig. 4.13), and this will also be confirmed in plasticity in the next section. Moreover, the use of the rotated Green operator is definitely more interesting both in terms of time of numerical convergence and in terms of microscopic field accuracy.

We also applied the different Green operators to the case of the inclusion with a stiffness ratio $c = 5$, whose homogenised macroscopic responses to two different loadings has been

(a) FEM (7216 elements)

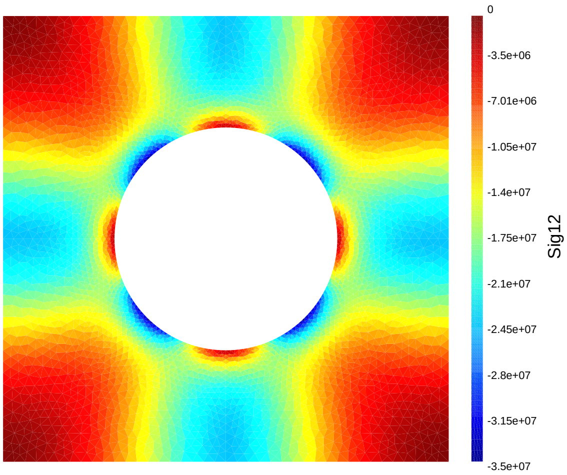

(b) $\boldsymbol{\Gamma}^0$ (c) $\boldsymbol{\Gamma}^R$

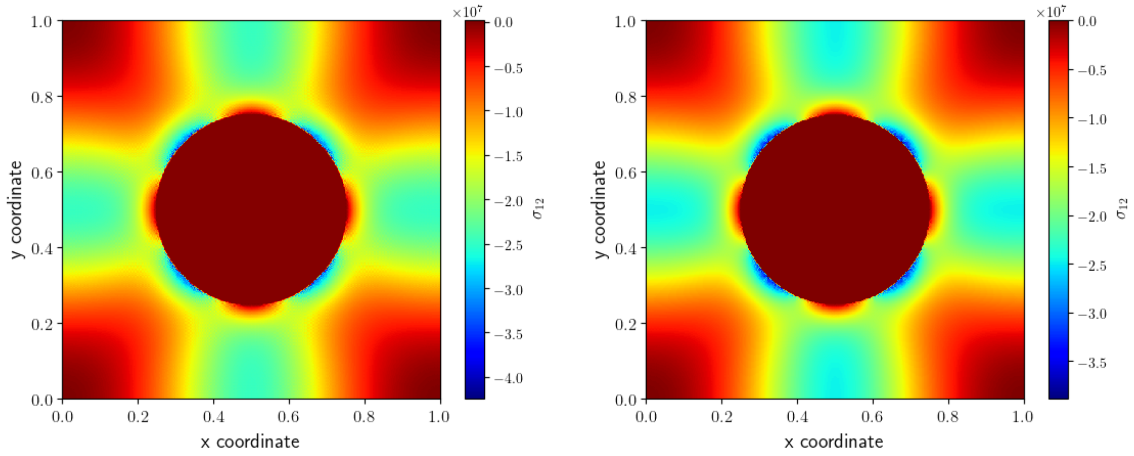

(d) $\boldsymbol{\Gamma}^0$ (zoom) (e) $\boldsymbol{\Gamma}^R$ (zoom)

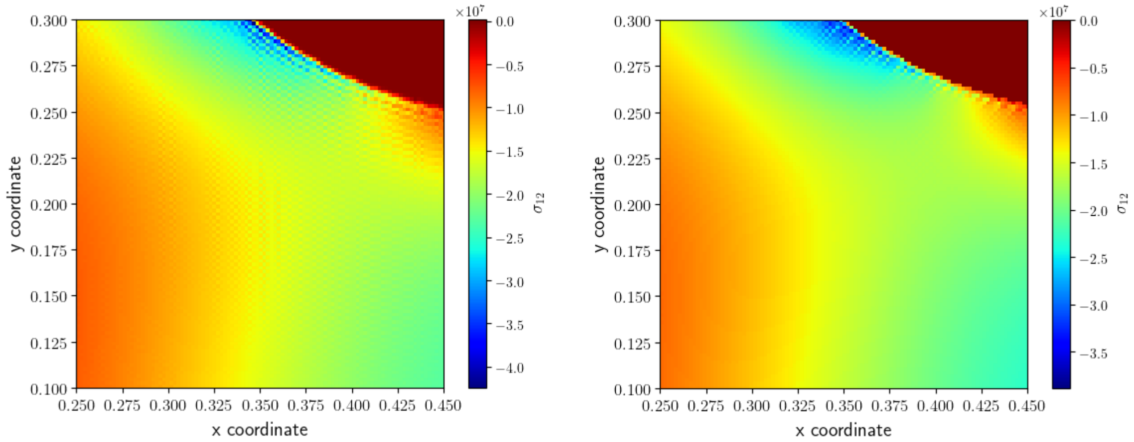

Fig. 4.12: Distribution of the stress component σ_{12} resulting from (a) the FEM homogenisation, (b),(c) the FFT-based homogenisation with two different Green operators. A zoom of the resulting stress field from (b) and (c) is represented in (d) and (e).

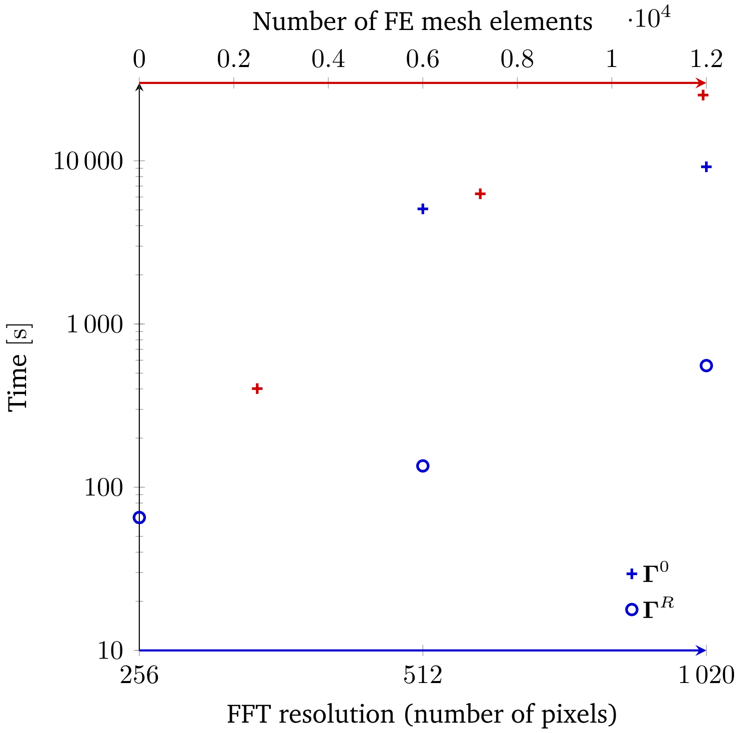

Fig. 4.13: Computation time for FFT-based and FEM homogenisation of a void inclusion embedded in an elastic matrix with the following Young's modulus and Poisson's ratio: $E_m = 2.67\text{GPa}$ and $\nu_m = 0.33$.

presented in Fig. 4.7 for the Green operator $\boldsymbol{\Gamma}^0$. Willot (2015) has already investigated the effects of the different operators on the distribution of the microscopic mechanical fields resulting from FFT-based homogenisation. He concluded in particular that the backward-and-forward operator $\boldsymbol{\Gamma}^W$ produced non-symmetrical fields at low resolutions (from 256 in the case of square inclusion), which is why we only applied the rotated and centered finite differences operators here. The microscopic distribution of stresses σ_{12} resulting from the shear load are presented in Fig. 4.14 and Fig. 4.15 for the FFT-based calculations and the FEM calculations respectively. The results clearly show the same results as the ones observed for the void inclusion in Fig. 4.12: the use of discrete Green operators $\boldsymbol{\Gamma}^0$ and $\boldsymbol{\Gamma}^C$ gives oscillating mechanical fields at low resolutions. Furthermore, the comparison of computation time at convergence (Fig. 4.16) confirms that the rotated Green operator allows for faster convergence and that the FEM is slower than the FFT-based homogenisation and that this trend increases when refining the discretised geometry.

(a) $\boldsymbol{\Gamma}^0$ $(N_1 = 512)$ (b) $\boldsymbol{\Gamma}^0$ $(N_1 = 512)$

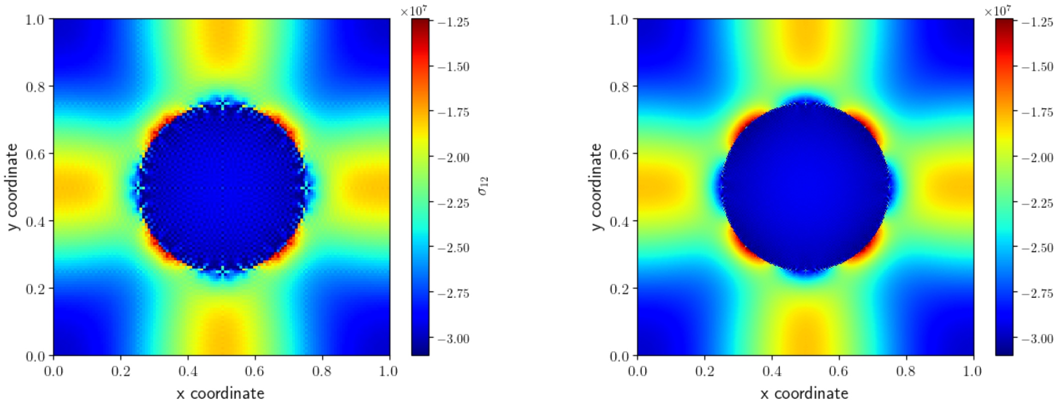

(c) $\boldsymbol{\Gamma}^C$ $(N_1 = 256)$ (d) $\boldsymbol{\Gamma}^C$ $(N_1 = 512)$

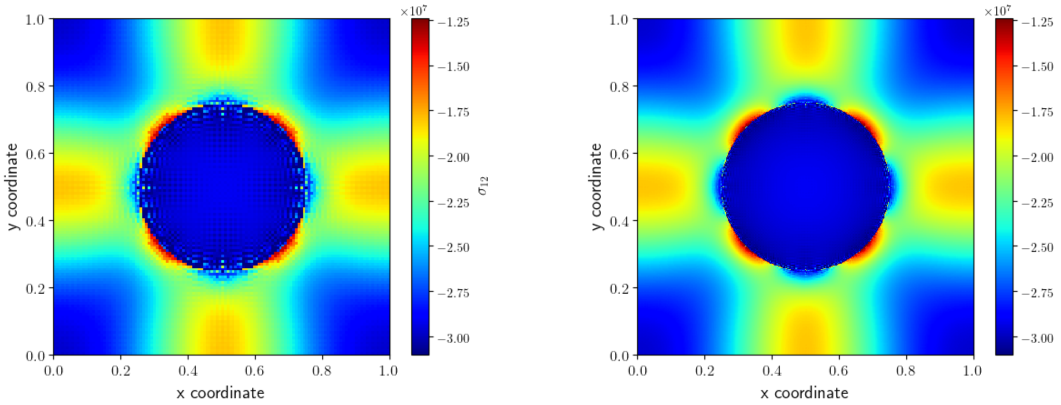

(e) $\boldsymbol{\Gamma}^R$ $(N_1 = 256)$ (f) $\boldsymbol{\Gamma}^R$ $(N_1 = 512)$

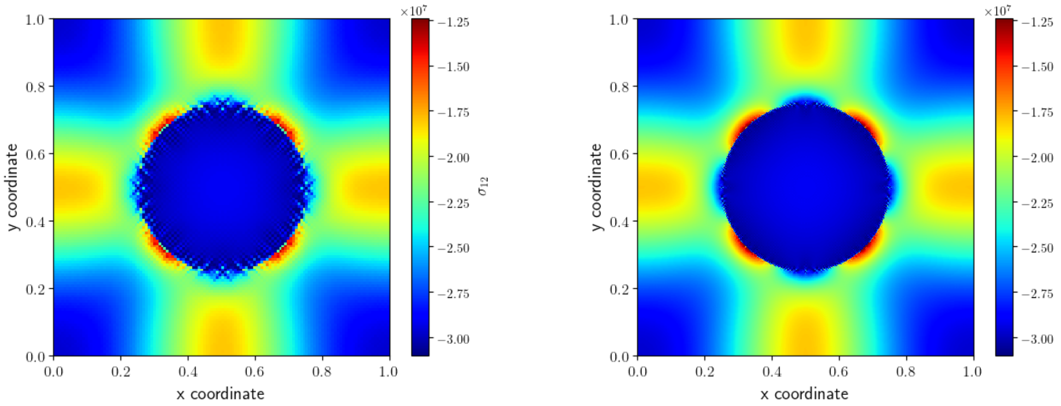

Fig. 4.14: Distribution of the stress component σ_{12} resulting from the FFT-based homogenisation of an elastic inclusion (contrast $c = 5$) with three different Green operators $\boldsymbol{\Gamma}^0$, $\boldsymbol{\Gamma}^C$ and $\boldsymbol{\Gamma}^R$ and at 2 different resolution, 256x256 and 512x512 pixels.

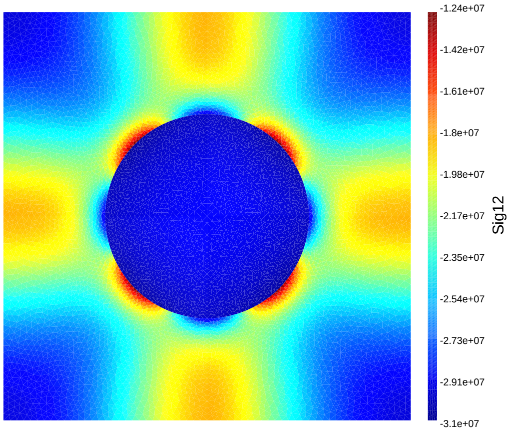

Fig. 4.15: Distribution of the stress component σ_{12} resulting from the FEM homogenisation of an elastic inclusion (contrast $c = 5$) (10432 elements)

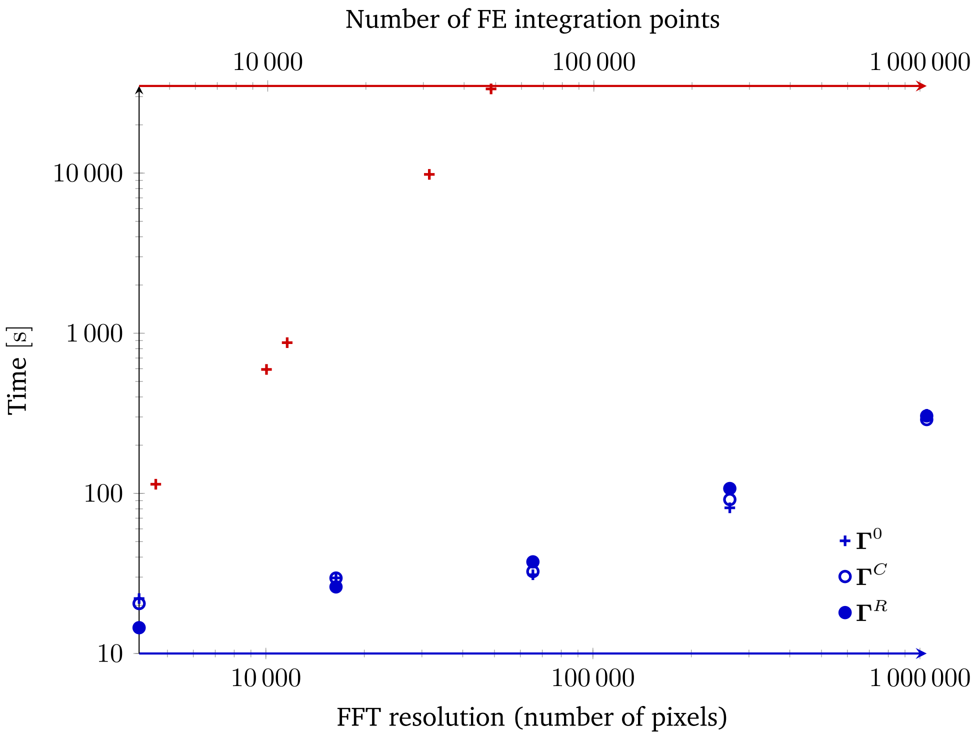

Fig. 4.16: Computation time for FFT-based and FEM homogenisation of an elastic inclusion embedded in an elastic matrix with a stiffness contrast of $c = 5$.

Tab. 4.2: Parameters of the two-phase microstructure used for the elastoplastic homogenisation calculations.

Phase	Young modulus	Poisson's ratio	yield strength (von Mises' criterion)
matrix	$E_m = 2.67\text{GPa}$	$\nu_m = 0.33$	$\sigma_y = 34.64\text{MPa}$
inclusion	$E_i = 13.33\text{GPa}$	$\nu_i = 0.33$	

4.4.2 Plasticity

The same 2D geometry for the microstructure was then used for the purpose of calculations with plasticity. In a further effort to compare our FFT code with the FEM software, we have this time assigned a local elastoplastic behaviour to the matrix surrounding the inclusion of our unit cell. We have therefore chosen an elastic perfectly plastic model with von Mises' criterion and subjected the microstructure to the same 2D macroscopic shear loading as in the elasticity part:

$$E_{12} = 1\%, \quad E_{11} = E_{22} = 0 \tag{4.60}$$

The data for the used materials are summarised in Tab. 4.2, σ_y is the yield stress or limit stress in the von Mises' criterion $\sqrt{3J_2} \leqslant \sigma_y$, where J_2 is the second deviatoric stress invariant defined by:

$$J_2 = \frac{1}{2}s_{ij}s_{ji} = \frac{1}{6}\left[(\sigma_{11}-\sigma_{22})^2 + (\sigma_{11}-\sigma_{33})^2 + (\sigma_{22}-\sigma_{33})^2\right] + \sigma_{12}^2 + \sigma_{13}^2 + \sigma_{23}^2 \tag{4.61}$$

with $s_{ij} = \sigma_{ij} - \frac{\sigma_{kk}}{3}\delta_{ij}$. Here, the applied macroscopic strain load implies that $\sqrt{J_2} \approx \sigma_{12}$ as all components but σ_{12} have a null average and thus are really small compared to σ_{12}. This also implies that the yield criterion becomes $\sigma_{12} \leqslant \sigma_y/\sqrt{3}$, which according to the value of σ_y corresponds to $\sigma_{12} \leqslant 20\text{MPa}$. The tolerance of the FFT-based code was again set to $\eta = 10^{-7}$, and the Green operators $\boldsymbol{\Gamma}^0$ and $\boldsymbol{\Gamma}^R$ were both used for these results. The comparative results are presented in Fig. 4.17 where we obtained a good agreement between the results of our FFT-based homogenisation code with two different Green operators and the results of the FEM software. The nonlinearity of the stress strain curve indicates that the material has reached a plastic behaviour at some points. Again the convergence was assessed by varying the mesh refinement and comparing the results obtained with it, as well as varying the pixel resolution (Fig. 4.18). For the given stiffness contrast, as it has been noticed in elasticity, the convergence is obtained even for coarser meshes and lower pixel resolutions such as 32x32 pixels.

The average of the homogenisation results over each phase is represented in Fig. 4.19, and helps understanding the influence of the elastoplastic behaviour of the matrix on the whole material response. The components $\boldsymbol{\Sigma}_{12}^m$, E_{12}^m and $\boldsymbol{\Sigma}_{12}^i$, E_{12}^i correspond to the average of σ_{12} and ϵ_{12} over the space domains of the matrix phase and the inclusion phase respectively. In the FFT-based method, since all pixels have the same dimension, these mean

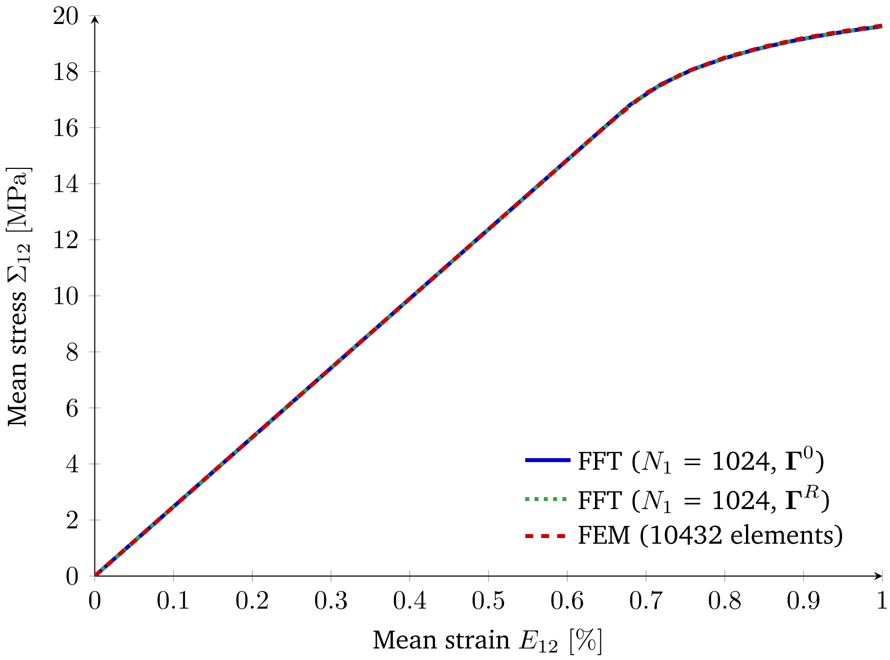

Fig. 4.17: Comparative results between FFT-based and FEM homogenisation of an elastic circular inclusion embedded in an elastoplastic matrix submitted to a macroscopic plane strain shearing.

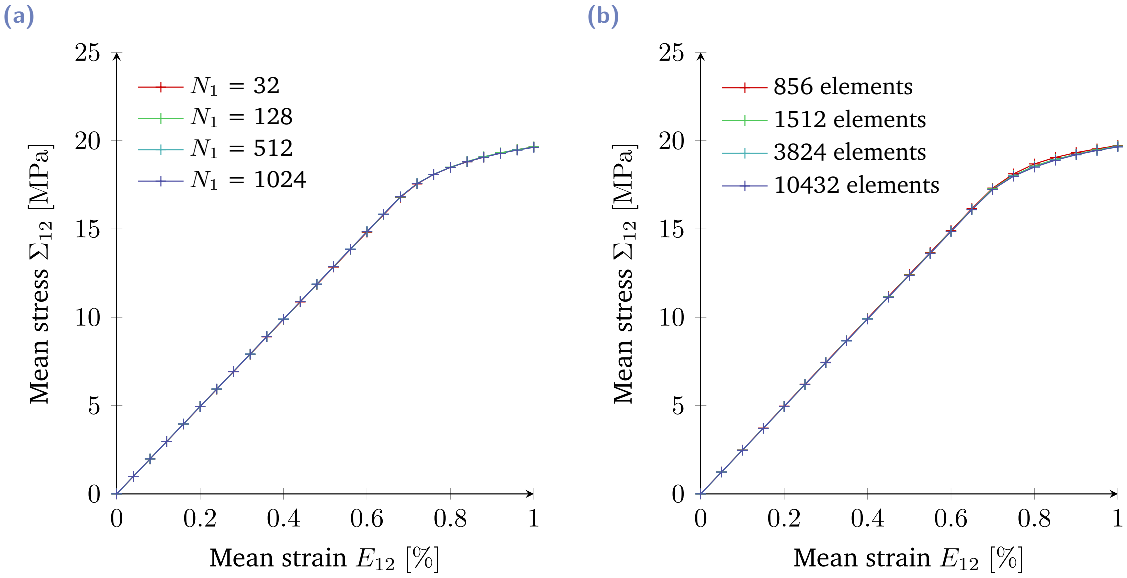

Fig. 4.18: Results of (a) FFT-based (with $\boldsymbol{\Gamma}^0$) and (b) FEM homogenisation of an elastic circular inclusion in an elastoplastic matrix at different resolutions or mesh refinements submitted to a macroscopic shear loading. Concerning the figure (a) the results follow the same trend with the rotated Green operator $\boldsymbol{\Gamma}^R$.

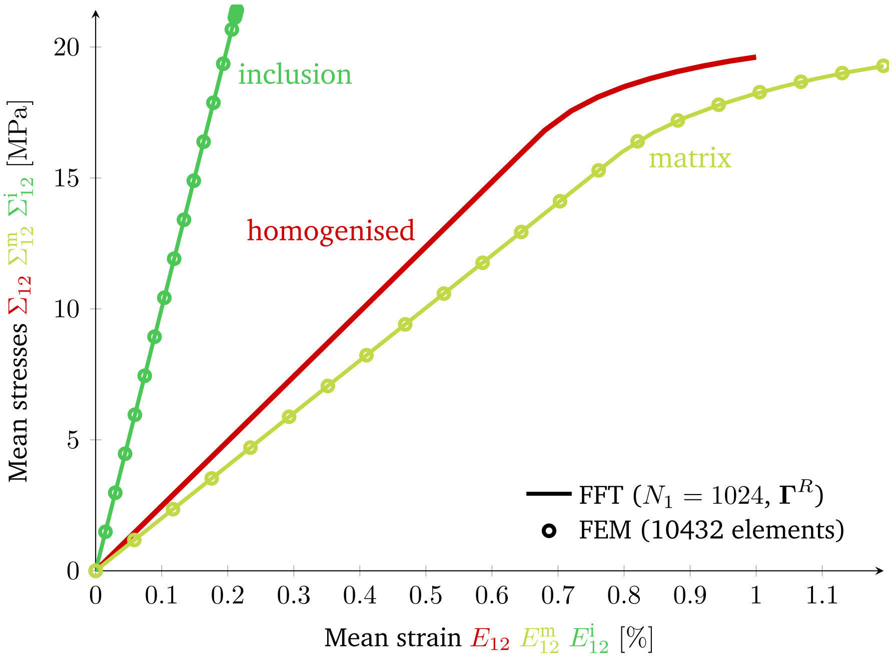

Fig. 4.19: Comparative average per phase results between FFT-based homogenisation with $\boldsymbol{\Gamma}^R$ at a resolution of 1024x1024 pixels, and FEM homogenisation with a 10432 element mesh, of an elastic circular inclusion embedded in an elastoplastic matrix submitted to a macroscopic plane strain shearing. In green are respresented the results averaged over each phase domain (matrix in light green, and inclusion in dark green), and in red is represented the homogenised response over the whole domain.

field components per phase are simply obtained by summing all the values of σ_{12} and ϵ_{12} of each pixel defined by the correct phase material and by normalising this sum by the total number of pixels of the given phase material. In the FEM, the same kind of operation is conducted but in the sum the values of σ_{12} and ϵ_{12} are weighted by the element volume or area over which they have been evaluated. At the end of the loading we can see that a large amount of the pixels of the matrix phase has reached the perfectly plastic regime. The choice of an elastic perfectly plastic model in our case implies that the value of σ_{12} can only reach the yield stress σ_y but not exceed it for the matrix phase, as well as its average value $\boldsymbol{\Sigma}_{12}^m$, so when the light green curve in Fig. 4.19 will reach the limit stress this will mean that all the domain has reached the plastic criterion.

It is also interesting to see it with the microstructure distribution of the yield criterion value $f = \sqrt{3J_2} - \sigma_y$ during loading (Fig. 4.20). While this yield criterion is negative the pixels or elements are still in the elastic regime, but we can see on the local distribution of this criterion that at the end of the loading a significant area has become plastic, or reached the perfectly plastic regime. Again, there is a good agreement between the results of the FEM and the results of the FFT-based method.

The comparison between computation times at convergence for the different methods are reproduced in Fig. 4.21, and show the same trend as in elasticity, that is a faster convergence with the FFT-based homogenisation code.

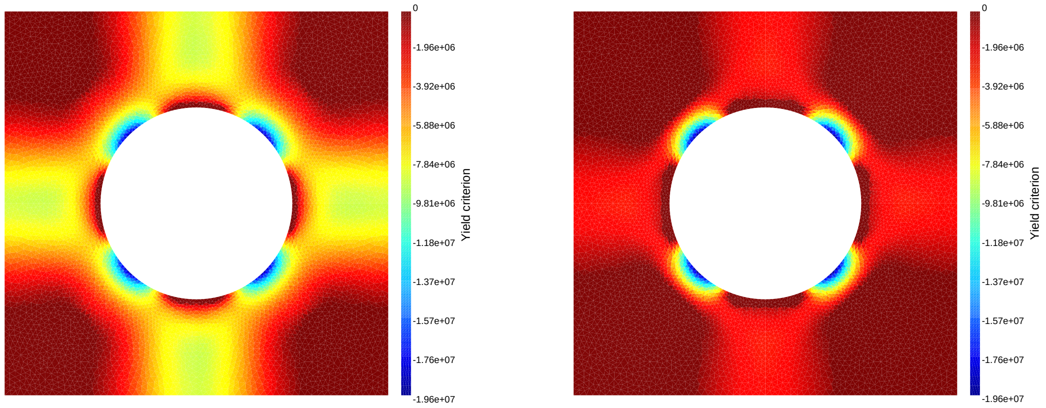
(a) FEM (7216 elements) **(b)** FEM (7216 elements)

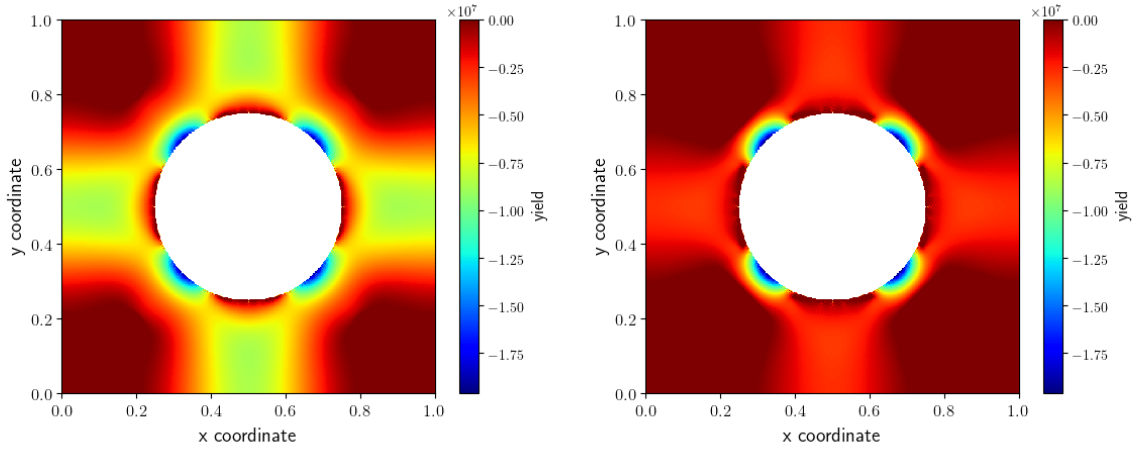
(c) $(N_1 = 512)$ $\boldsymbol{\Gamma}^R$, $E_{12} = 0.8\%$ **(d)** $(N_1 = 512)$ $\boldsymbol{\Gamma}^R$, $E_{12} = 1.0\%$

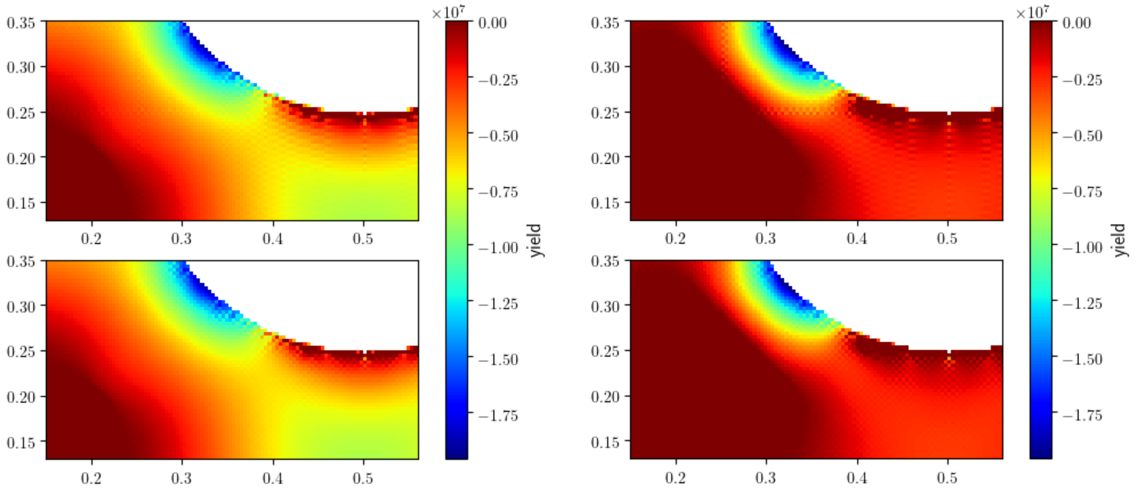
(e) (zoom) above: $\boldsymbol{\Gamma}^0$, below: $\boldsymbol{\Gamma}^R$, $E_{12} = 0.8\%$ **(f)** $E_{12} = 1.0\%$

Fig. 4.20: Distribution of the yield criterion over the matrix phase resulting from (a), (b) the FEM homogenisation, (c),(d) the FFT-based homogenisation with the rotated Green operator, at two different values of the macroscopic strain load. A zoom of the resulting yield criterion from (c) and (d) is represented in (e) and (f) on the bottom figures, the top ones being the results obtained with $\boldsymbol{\Gamma}^0$.

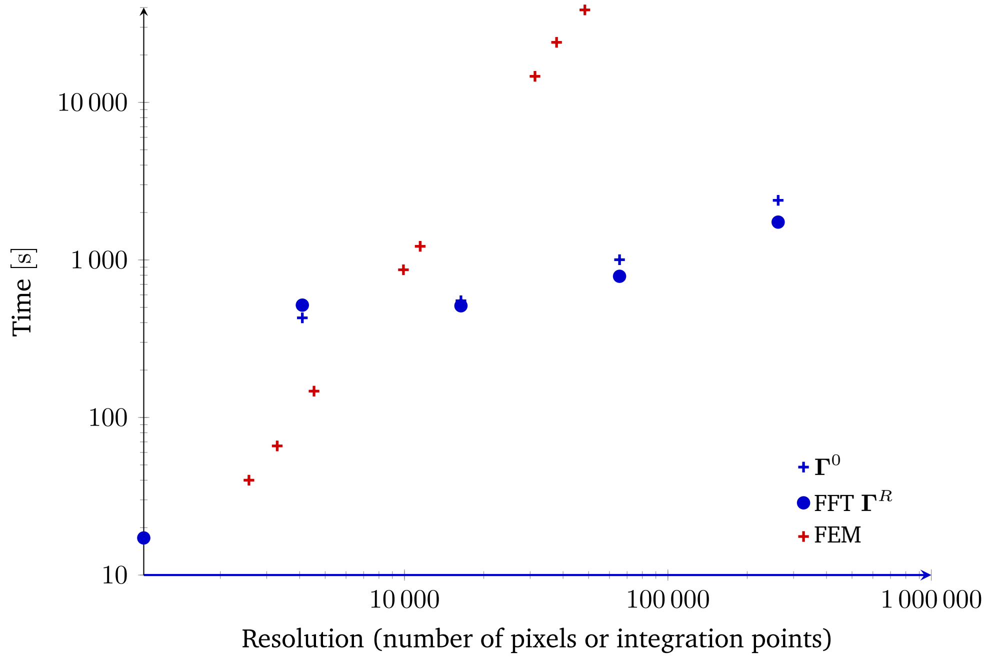

Fig. 4.21: Computation time for FFT-based and FEM homogenisation of an elastic inclusion embedded in an elastoplastic matrix with a stiffness contrast of $c = 5$.

4.5 Conclusion

This section introduced the principles of the FFT-based homogenisation techniques and more particularly the method of Gélébart and Mondon-Cancel (2013) that we implemented in our code. The FFT-based homogenisation methods do not need any mesh like the FEM, they can use real images as input geometry, and they can be quite easy to implement with efficient open source libraries. The combination of a Newton-Raphson algorithm with a conjugate gradient solver that Gélébart and Mondon-Cancel (2013) developped allows for the homogenisation of materials with high stiffness contrasts. This is interesting in our case for the next section, where we will apply this method to different gas hydrate bearing soils with stiffness contrasts that can be quite significant. Moreover the same FFT-based method implemented in our code allows for the use of any nonlinear law, that is nonlinear elasticity, plasticity or even viscosity. This was also a criterion in our choice for the modelling of the gas hydrate bearing soils as they present a clear nonlinear behaviour according to the results of different laboratory experiments (see section 2.2).

Our code has been validated against a FEM software both in linear elasticity and elastoplasticity for uniform macroscopic strain loadings. The results even showed that the computation time at convergence is lower with the FFT-based method than with the FEM.

5

Application to GHBS

5.1 Introduction

Gas hydrate crystals occupy the pore space of sediments in different ways depending on the conditions under which they were formed (Waite et al., 2009). In coarse-grained sediments gas hydrates can occur under various types of pore habits usually described in the literature as pore-filling, load-bearing or cementing (Waite et al., 2009; Chaouachi, 2015). It is generally assumed that in the laboratory one of the two common methods of synthesis leads to a load-bearing type of hydrates while the other one leads to a cementing type of hydrates (Ebinuma et al., 2005). In fine sediments they can fracture the soil matrix and form networks of veins (Rees et al., 2011). These complex microstructures influence the macroscopic (apparent) response of the material.

The FFT-based homogenisation method we described in the previous chapter can be applied to study the impact of parameters such as pore habits or volume fraction of gas hydrates on the macroscopic behaviour of GHBS. This is the purpose of the present chapter. First we introduce the local mechanical constitutive laws used to define the materials of the phases constituting the gas hydrate bearing soils. In a second step we present the results obtained by application to different types of natural sediments that naturally contain gas hydrates. Different 2D geometries, based either on schematic representations or real images, are tested. Finally, we end with an application to 3D images of sand containing synthetic methane hydrates obtained at the synchrotron by a team from our laboratory.

5.2 Granular microstructures

5.2.1 Elasticity

We first tested periodic microstructures with different hydrate pore habits in densely packed spheres representing grains of sand for example. For the same grain packing, hydrates were in two configurations: around each grain in a 'grain-coating' mode, or inside the void or pore volume but in contact with the spheres in a 'load-bearing' mode. Fig. 5.1 illustrates this description, and shows the two-dimensional geometries that were used as unit cells for our homogenisation calculations. These geometries were defined by three different

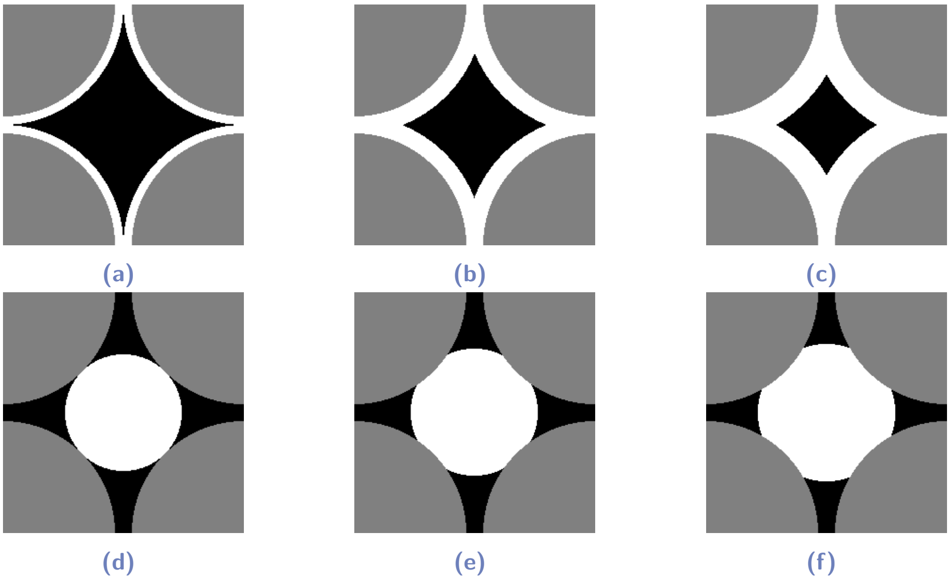
(a) (b) (c) (d) (e) (f)

Fig. 5.1: Microstructures for a porosity of $n = 32$ and at a resolution of 256x256 pixels, with solid grains in grey, gas hydrates in white and voids in black. (a),(b) and (c) show grain-coating hydrates, (d), (e) and (f) represent load-bearing gas hydrates.

hydrate volume fractions of pores, or hydrate saturations S_H, 33%, 60% and 77% for the coated grains and 57.5%, 65% and 70% for load-bearing hydrates. These values of hydrate saturations have already been encountered in nature in granular soils, but they may be too large for fine soils.

The following elastic parameters (Young's modulus and Poisson's ratio) were given for each phase: $E_g = 94$ GPa and $\nu_g = 0.1$ for the grains considering that they are made up of quartz, $E_h = 9$ GPa and $\nu_h = 0.32$ for the gas hydrates and null parameters for the void or liquid phase as we were interested in the effective behaviour of the composite material. Each unit cell was submitted to the two following macroscopic strain loadings:

$$E_{11} = 1 \text{ and } E_{ij} = 0 \quad \forall i \neq 1 \text{ or } j \neq 1 \tag{5.1}$$

$$E_{12} = E_{21} = 0.5 \text{ and others } E_{ij} = 0 \tag{5.2}$$

This allowed to determine the effective stiffness matrix components $\mathbb{C}_{1111}$ and $\mathbb{C}_{1212}$ respectively as at the end of the first loading $\boldsymbol{\Sigma}_{11} = \mathbb{C}_{1111} E_{11} = \mathbb{C}_{1111}$ and of the second one $\boldsymbol{\Sigma}_{12} = 2\mathbb{C}_{1212} E_{12} = \mathbb{C}_{1212}$.

The resulting effective stiffness components are represented in Fig. 5.2 in function of the hydrate saturation and of the type of hydrate occupancy of the pore. These first results are in agreement of the general trends for cemented materials as the grain-coated microstructures have higher stiffness components than the ones containing load-bearing hydrates.

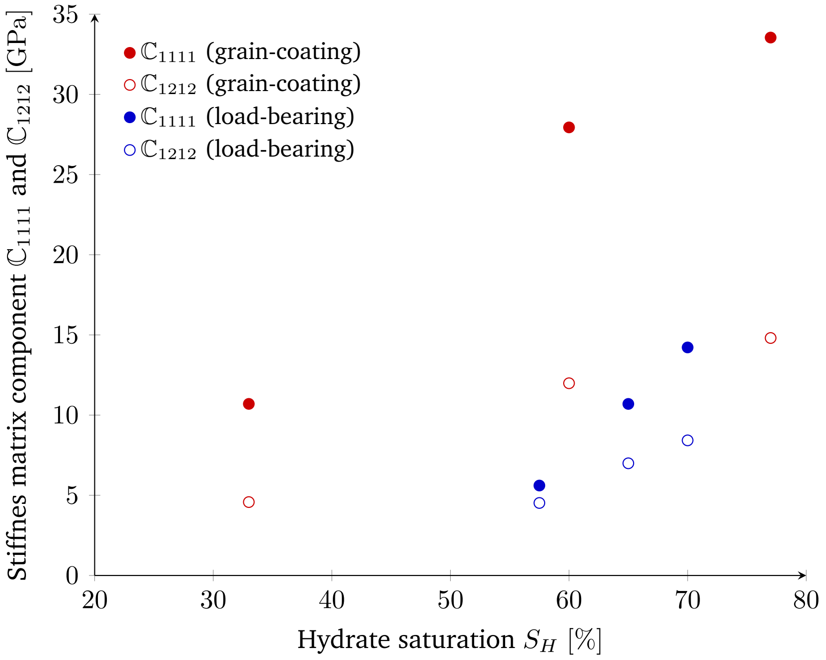

Fig. 5.2: Homogenised stiffness components $\mathbb{C}_{1111}$ and $\mathbb{C}_{1212}$ function of gas hydrate saturations and pore occupancy mode in the geometries.

However, the homogenised values of elastic stiffness components are too high. This is due to the dense packing geometry that is not very representative of the usual porosities observed in natural gas hydrate bearing granular soils. We present in the next section less dense microstructures with a plastic behaviour of the gas hydrate phase.

5.2.2 Plasticity

In this section, different periodic geometries of two-dimensional coarse-grained microstructures were tested as examples (Fig. 5.3 and Fig. 5.4) to demonstrate the relevance of the method in the study of gas hydrate bearing soils. The pore space around randomly distributed grains at a given porosity was filled with hydrates using two different scenarios of pore habits: load-bearing and cementing gas hydrates (Fig. 5.4). Three phases constitute the material in these calculations: rigid grains, hydrates and voids, with a volume fraction of gas hydrates varying between 80% and 100% of the pore space. We did not consider lower hydrate saturations in these simulations in 2D because we needed a surface of hydrates large enough to ensure a continuity between the solid phases to avoid the occurrence of floating grains. A loading corresponding to an oedometer test was applied to the different unit cells:

$$\Delta E_{11} = 1\% \text{ and } \Delta E_{22} = \Delta E_{12} = \Delta E_{13} = \Delta E_{23} = \Delta E_{33} = 0 \qquad (5.3)$$

The grains were assumed to have an isotropic linear elastic behaviour, defined by the following Young's modulus and Poisson's ratio: $E_g = 2.45$ GPa, $\nu_g = 0.1$. We used the Poisson's ratio of the quartz material (Mcknight et al., 2008), and we chose a Young's

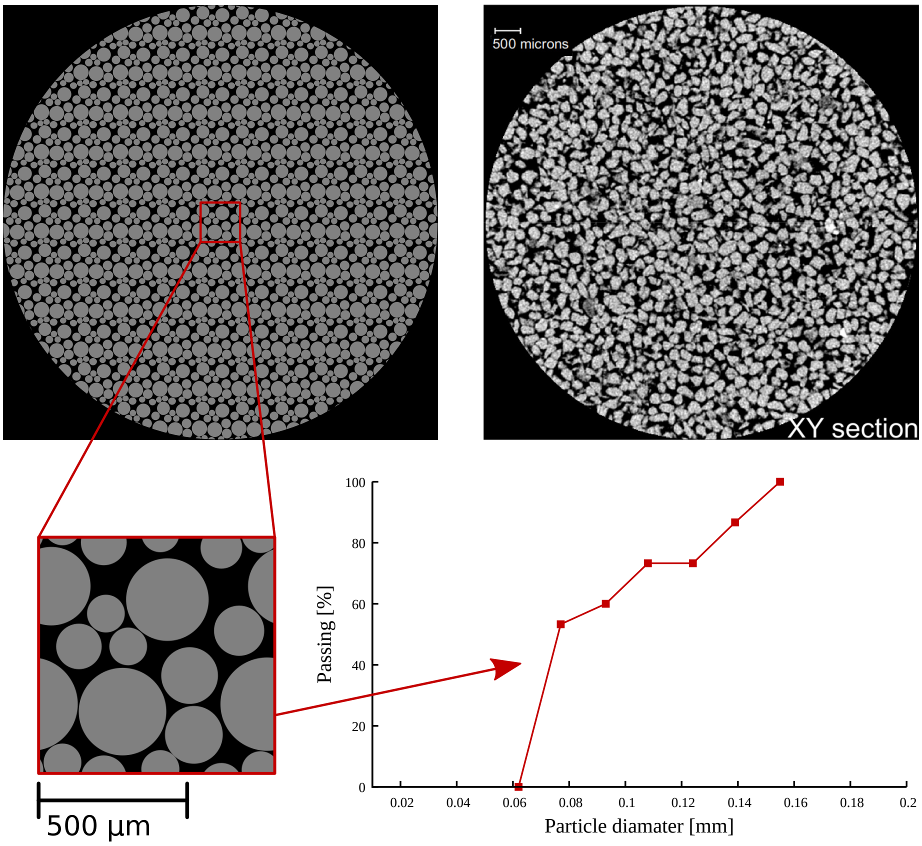

Fig. 5.3: The upper right image shows a typical example of a real coarse-grained microstructure with a porosity of $n = 0.28$ (Al Mahbub and Haque, 2016) and the upper left image represents an example of the ideal periodic microstructures that we imagined for our calculations. The unit cell used in this example to describe the microstructure (with a porosity of $n = 0.27$) is shown below. Here we only represent the granular skeleton of the microstructure, obtained by randomly adding circles with a radius between 0.08 and 0.2 in a unit square. To obtain realistic values of microstructures from this unit-square, we simply multiply the length of each geometrical object by the desired length scale, which gives us the realistic grain size distribution on the right.

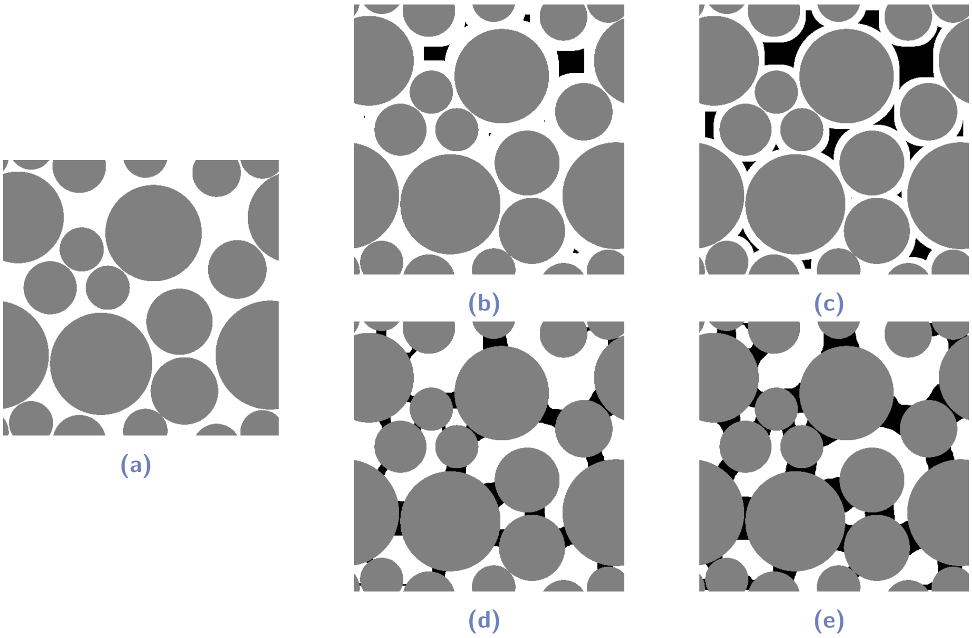

(a) (b) (c) (d) (e)

Fig. 5.4: Examples of microstructures for a porosity of $n = 0.27$ and at a resolution of 512 pixels, with solid grains in grey, gas hydrates in white and voids in black. In (a) voids are completely filled with hydrates. (b) and (c) represent cementing gas hydrates at 95% and 80% of pore volume fraction respectively while (d) and (e) represent load-bearing gas hydrates at 90% and 80% of pore volume fraction.

modulus that gave us results approaching those of mechanical tests performed on methane hydrate bearing sands in the laboratory (Le et al., 2019). There are only few data and test results regarding the behaviour of pure gas hydrates samples, but Yoneda et al. (2019) managed to retrieve natural pressure core samples of massive gas hydrates and tested them. They obtained values for the Young's modulus of $287\ \mathrm{MPa}$ and $350\ \mathrm{MPa}$ under quasi-static conditions, and maximum deviator stress values of $3.04\ \mathrm{MPa}$ and $3.24\ \mathrm{MPa}$. This is why the gas hydrate phase was defined by an elastic perfectly plastic model with von Mises' criterion, with the given parameters: $E_h = 300\ \mathrm{MPa}$, $\nu_h = 0.32$, and a yield strength equal to $\sigma_y = 3\ \mathrm{MPa}$. The Poisson's ratio for the pure hydrate phase was taken from Sloan and Koh (2007). The voids represent fluid-filled porosity and were characterised by a null stiffness matrix, like in a drained test configuration, as we homogenise the effective properties of the material. The macroscopic stress-strain response is obtained by averaging the microscopic fields over the entire unit cell at the end of each time step. A tolerance of $\eta = 10^{-7}$ was taken for the calculations.

First, we looked at the repeatability of our simulations by performing calculations over randomly drawn unit cells with a hydrate saturation of 100% and a porosity between 27.8% and 28.8% but with different arrangements of the granular skeleton. The mean macroscopic response and the corresponding standard deviation obtained for 10 different simulations are plotted in Fig. 5.5 and show a rather low dispersion.

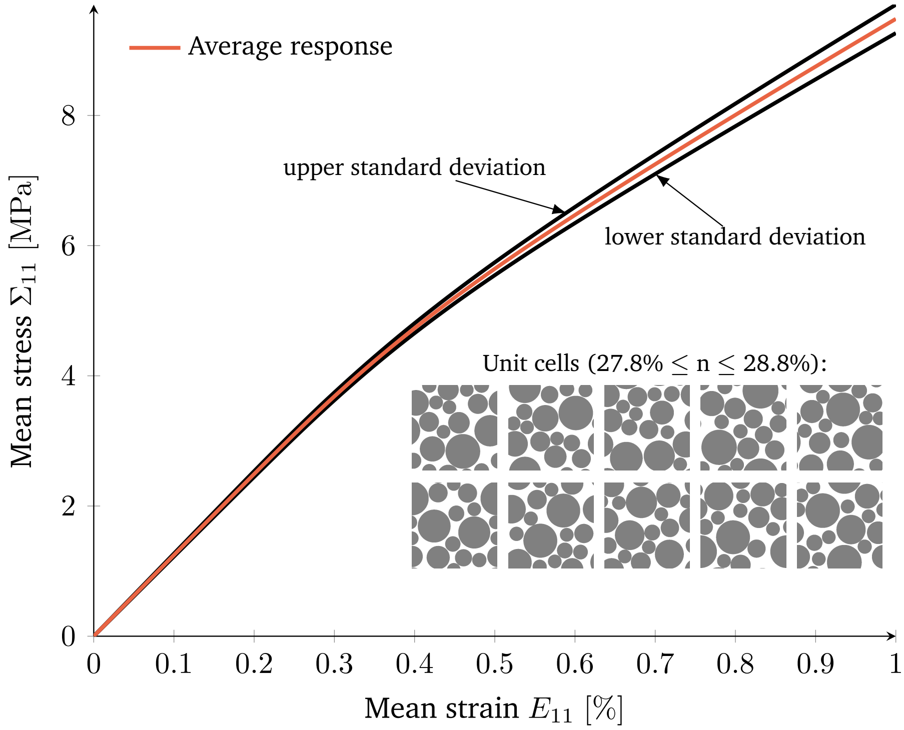

Fig. 5.5: Average macroscopic stress-strain response (in red) to the oedometer loading of 10 random granular microstructures, each with a porosity n between 27.8% and 28.8%. The upper and lower black curves represent the standard deviation of the responses of the simulated microstructures that are represented at the bottom right part of the figure.

Fig. 5.6 shows the results for 'cemented' microstructures of two different porosities, $n = 0.4$ and $n = 0.27$, and various values of volume fraction of gas hydrates for each of them. As expected, the increase in gas hydrate saturation and the decrease in porosity lead to a stiffer material, which is in ageement with many experimental results. In Fig. 5.7, a comparison between the effects of cementing and load-bearing gas hydrates is represented for a given porosity. The global responses of the two types of pore habits for the same volume fraction of hydrates match expectations. The cemented structures have a stiffer mechanical response while the load-bearing structure yields more rapidly. Both morphologies reach a perfectly plastic behaviour when hydrates occupy a volume fraction of the pores of $S_h = 80\%$. The fact that the chosen technique does not take into account contact laws and that we chose a unit cell containing only few grains plays a role on the resulting macromechanical fields. The geometries that were chosen as unit cell in this section are based on circular solid grains representing the sedimentary phase, but more complex and realistic microstructures have to be used in the study of gas hydrate bearing sediments. The advantage of the FFT-based homogenisation methods is that one can analyse real images. In the next section we present the case of fine soils containing gas hydrate with unit-cells adapted from real images.

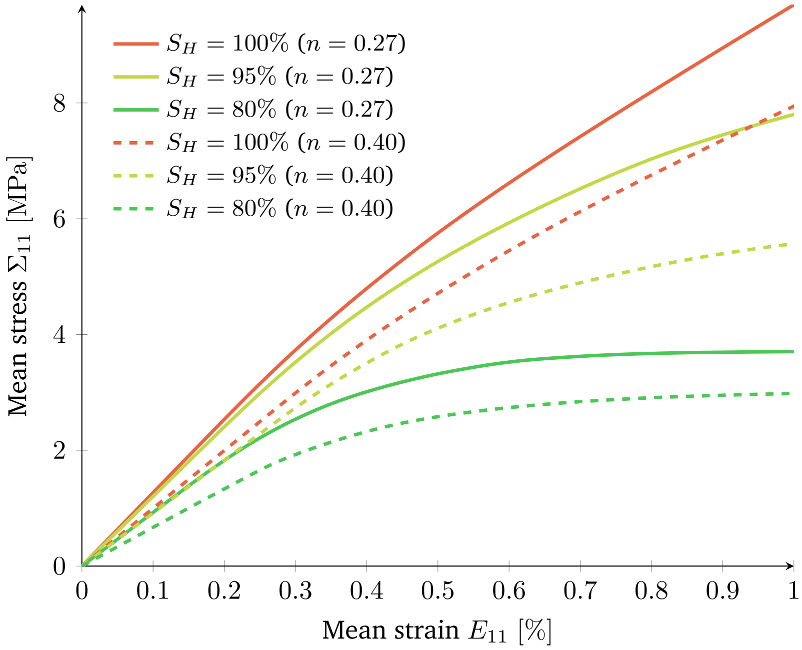

Fig. 5.6: Macroscopic stress-strain response to the loading of the granular soil with cementing gas hydrates for different values of porosity and gas hydrate saturation, at a resolution of 512 pixels.

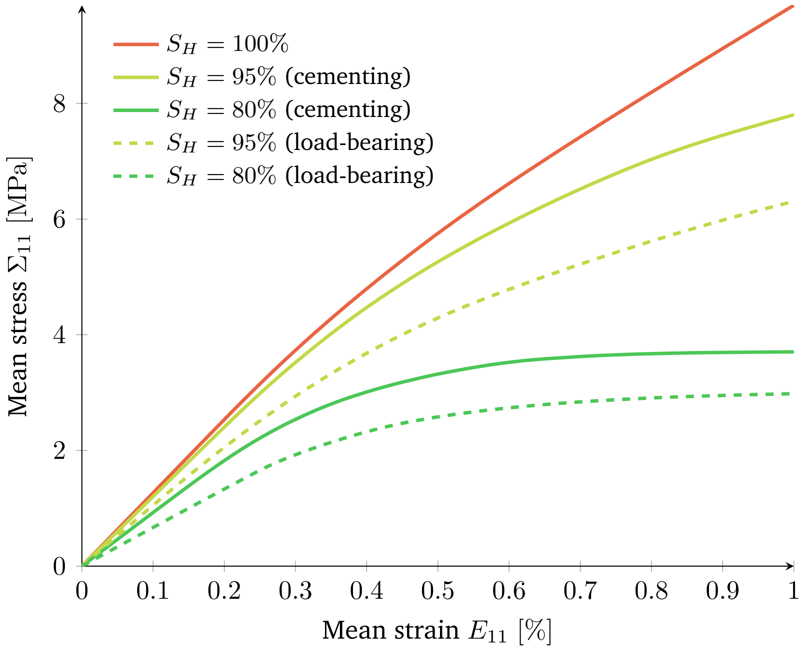

Fig. 5.7: Macroscopic stress-strain response to an 'oedometer' loading of granular soil for different pore habits - cementing and load-bearing - and different values of gas hydrate saturation S_H, at a porosity of n=0.27 and a resolution of 512 pixels.

5.3 Fine soil microstructures

Few studies managed for now to get real images of gas hydrate bearing soils at the microscopic scale. Since it is difficult and expensive to get pressure core samples and maintain them under in situ conditions, the observation of gas hydrate nucleation through x-ray microtomography for example are mainly done on synthetic samples (Chaouachi et al., 2015). However the investigations that have been conducted until today give an insight of the actual microstructure of gas hydrate bearing soils and can be used as unit cells to homogenise the mechanical properties.

In this section we applied the same FFT-based homogenisation code to a real image of hydrate veins in fine sediments. There are only few images of the microstructure of fine-grained sediments with gas hydrates. It is known that gas hydrates tend to occur as veins and nodules in fine-grained sediments, in contrast with coarse-grained soils. A unit cell with a resolution of 256 pixels was defined based on the micro Computed Tomography (CT) scans of depressurised and cooled cores from the Krishna-Godavari Basin (Rees et al., 2011) represented in Fig. 5.8.

Fig. 5.9 shows the original image and its *periodic-plus-smooth decomposition* (Moisan, 2011) via Brisard's Python implementation (Brisard, 2018). By working with a non-periodic image the resulting mechanical fields would be disturbed at the edges. This image processing allows us to work with a periodic REV, but it should also be noted that it generates a disturbed image compared to the original one around the edges.

In Rees et al. (2011) the scans were done on samples that had been obtained by depressurising pressure cores, cuting them into sections and freezing them with nitrogen. Some oberved veins may have been filled with either gas hydrates, ice or water. Considering the sample disturbance prior to scanning and the potential phase changes resulting from it, it would be very difficult to define the exact distribution of phases. For simplicity in this example we chose to define only two phases from the periodic microstructure: the fine-grained soil matrix and the gas hydrates phase forming veins (Fig. 5.9d). For the homogenisation calculations we then had to segment the real image in order to identify the two constituting phases. Two threshold values were tested for the image segmentation: (A) the minimum value of the valley between the two principal peaks of the image histogram, and (B) the average value of these two peaks (figure 5.10). Morphological operations such as dilation and erosion were then applied to process the resulting images in order to get artificial volume fractions of the gas hydrate phase f_{H} (14%, 16%, 23% and 34%). These operations consist in adding or removing pixels to or from object boundaries, the object being hydrates veins in our case.

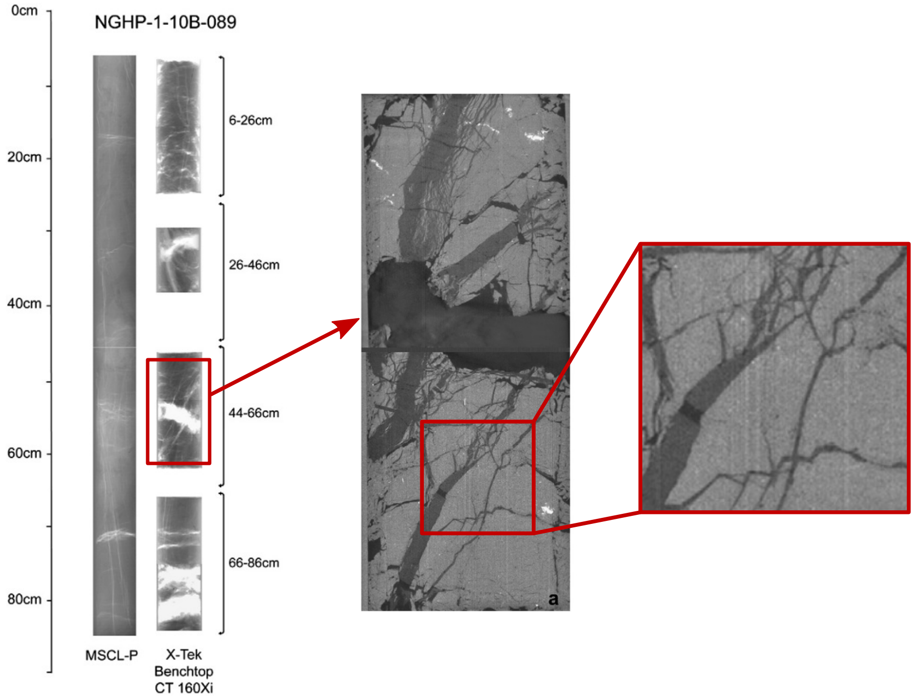

Fig. 5.8: On the left are represented X-ray images of a natural core published by Rees et al. (2011) and from which the vertical slice (a, in the middle) of core section 46-66cm was taken using the micro CT scanning method. On the right we represent the extracted image that we chose to use for our application, which corresponds to an area with vein inclusions, while we can observe a nodule above it in the middle image.

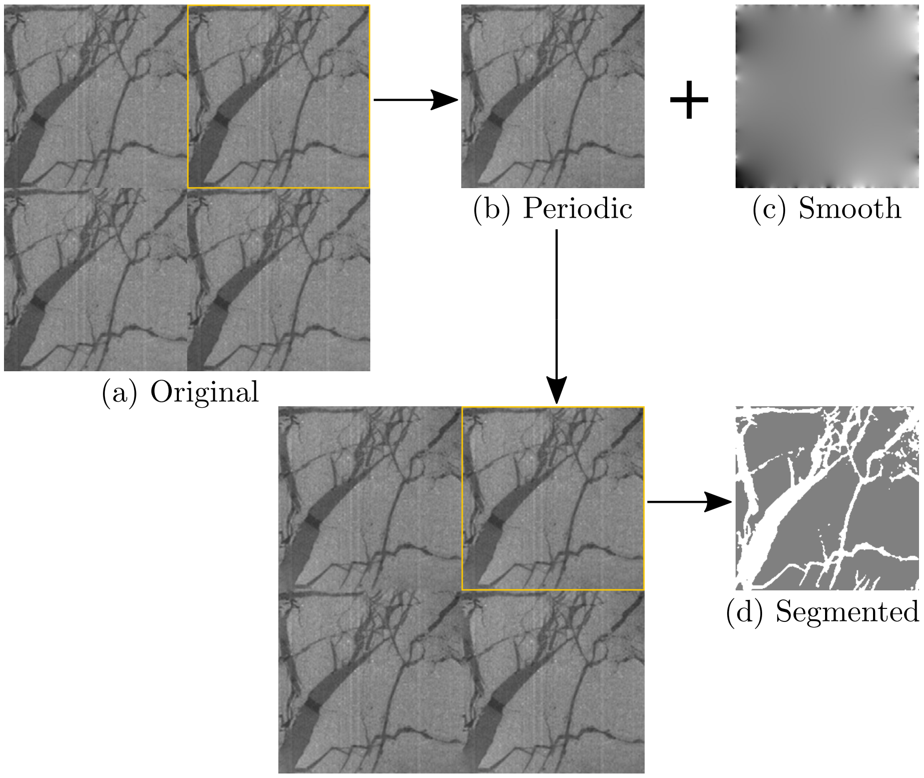
(a) Original
(b) Periodic
(c) Smooth
(d) Segmented

Fig. 5.9: Periodic pattern made with the real image (a) used as a unit-cell (yellow box - 256 pixels resolution); its periodic (b) plus smooth (c) decomposition and the segmented image (d) used for calculations.

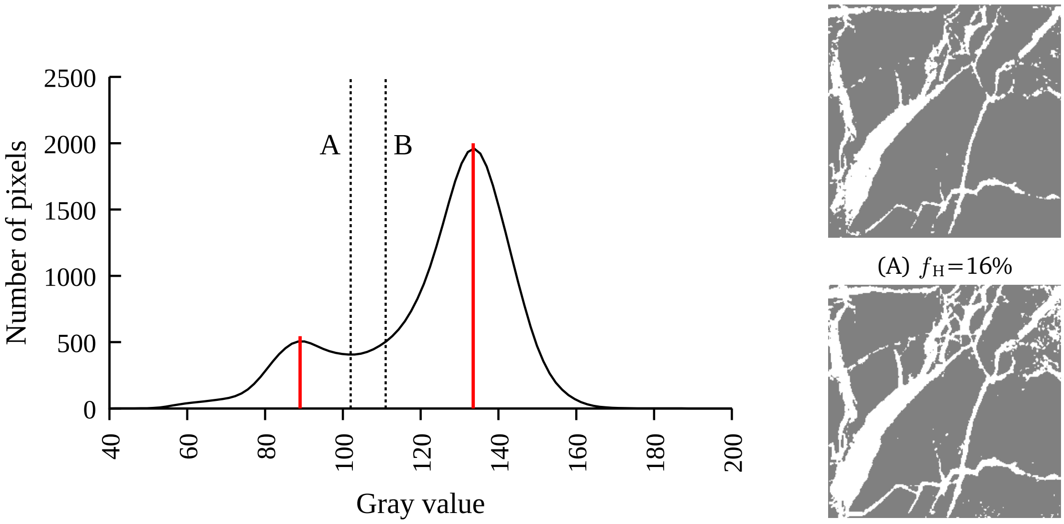

(A) f_{H}=16%

(B) f_{H}=23%

Fig. 5.10: On the left the smooth histogram of the periodic real image (see Fig. 5.9b) from which two threshold values were chosen: A is the grey value corresponding to the minimum number of pixels in the valley between the two peaks in red, and B is the mean value of these peaks. On the right the segmented images obtained from A and B and the corresponding volume fraction of gas hydrates f_{H}.

Tab. 5.1: Cam Clay properties for the fine soil matrix

Parameter	Value	Unit
Compression index λ	0.1	-
Swelling index κ	0.01	-
Elastic shear modulus G	300	(MPa)
Pre-consolidation pressure p_{c0}	2	(MPa)
Initial Porosity ϕ	0.37	-
Slope of critical state line M	1.0	-
Initial mean stress p_0	1.25	(MPa)

The gas hydrate phase was defined by an elastic perfectly plastic model with von Mises' criterion, with the given elastic parameters: $E_h = 9\ \mathrm{GPa}$, $\nu_h = 0.32$ (dynamic moduli from Sloan and Koh, 2007). For a first assessment and based on existing data (Hyodo et al., 2002; Yu et al., 2011b) the yield stress has been taken equal to $\sigma_y = 5\ \mathrm{MPa}$. The local material for the soil matrix was defined by a modified Cam-Clay model, and the properties are summarised in Tab. 5.1. The macroscopic loading consisted in a mixed loading, comparable to a triaxial compression test loading. Starting from a uniform initial stress of 1.25 MPa over the entire cell, the horizontal stresses were kept constant while a vertical strain loading was imposed until reaching the macroscopic mean strain value of 5%:

$$\varDelta E_{11} = 5\% \text{ and } \varDelta \boldsymbol{\Sigma}_{22} = \varDelta \boldsymbol{\Sigma}_{33} = \varDelta \boldsymbol{\Sigma}_{ij} = 0 \quad \forall i \neq j \tag{5.4}$$

Given the fact that the unit cell is two-dimensional and to insure the periodicity conditions on the displacements, the fluctuating part of the cross-sectional strain ϵ'_{33} has to be null. The condition $\Delta\boldsymbol{\Sigma}_{33} = 0$ corresponds to a microscopic plane stress condition with a non-zero mean strain component in the cross direction: $E_{33} \neq 0$. A tolerance of $\eta = 10^{-5}$ was taken for the calculations.

The homogenised macroscopic results are represented in Fig. 5.11. There is a difference in the response of the segmented images prior to morphological operations (Fig. 5.10), meaning the segmentation with the threshold value A with $S_H = 16\%$ and the one with the threshold value B and $S_H = 23\%$. However the stress-strain curves of homogenised images obtained from different threshold values of segmentation but with comparable hydrate volume fraction are relatively close. In this case, for equivalent hydrate volume fractions, the segmentation method does not seem to be important. One can observe the effect of the plastic yielding of the sedimentary matrix on the global response of the material. The behaviour is clearly nonlinear and shows two different trends during the shearing: a first one with the deviator stress value under approximately 0.5 MPa and a second one beyond 0.5 MPa. The second part corresponds to the moment when an important part of the local points of the solid matrix yields. The evolution of the fraction of yielding pixels over each entire phase in Fig. 5.12 shows that the soil matrix yields more quickly than the gas hydrates here. Indeed, between 0.62 MPa and 0.83 MPa of the deviator stress values, the fraction of yielding pixels over the soil material increase from 1.49% to 28.11% (Fig. 5.12b and 5.12c). Fig. 5.13 shows the evolution of the fraction of yielding pixels but in function of the mean strain component ϵ_{11} this time, and we can see that the soil matrix has practically entirely yielded when $E_{11} = 1\%$, while this is only the case when $E_{11} = 3.5\%$ for the gas hydrate phase.

There are three stages in the behaviour of the unit cells when we look at Fig. 5.12: an elastic part when the deviator q is below 0.5 MPa, the yielding of the soil matrix pixels when q is between 0.5 and 1.0 MPa and finally the yielding of the gas hydrate pixels while all pixels of the soil matrix phase exhibit a hardening behaviour when q is above 1.0 MPa. The distinction between the last two parts of the macroscopic response is not clearly visible in the stress-strain curve of Fig. 5.11 though, as the pixels of the gas hydrate phase represent a small fraction of each whole unit cell: 34% at the maximum. Locally the gas hydrate phase reaches the perfectly plastic regime characterized by a constant value of deviator stress but the hardening behaviour of the soil matrix pixels prevails as they representing 76% volume fraction of the unit cell at the minimum. Figure 5.12 also shows that the gas hydrates have an influence on the point when 100% of the soil matrix pixels have reached the plastic regime. An increase of the gas hydrate volume fraction seems to delay the yielding of the soil matrix as there are more gas hydrates pixels to support the loading.

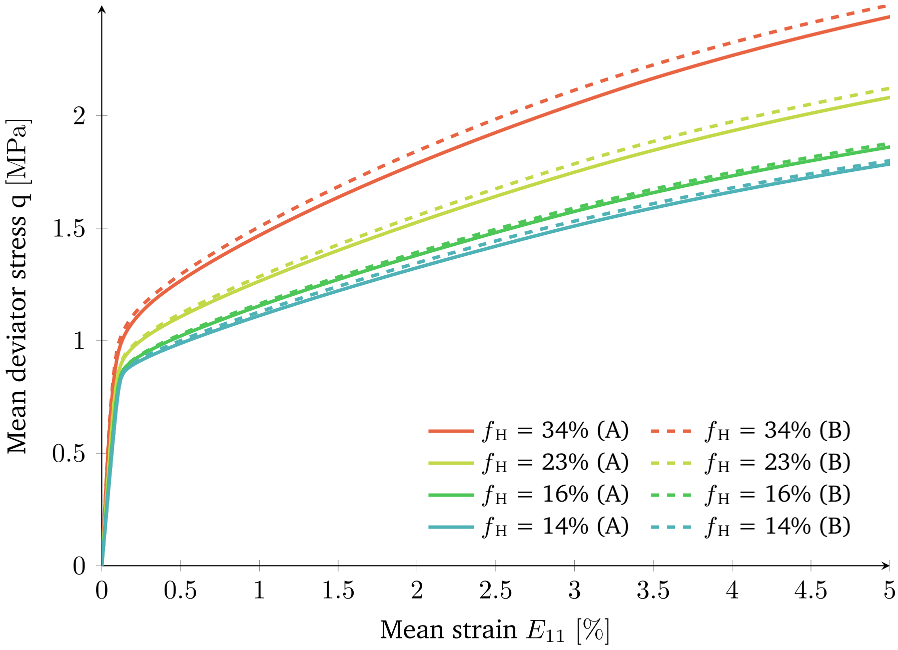

Fig. 5.11: Macroscopic stress-strain responses of fine soils with hydrate veins inclusions for four different values of gas hydrate volume fractions (f_H=14%, f_H=16%, f_H=23% and f_H=34%), at a resolution of 256 pixels.

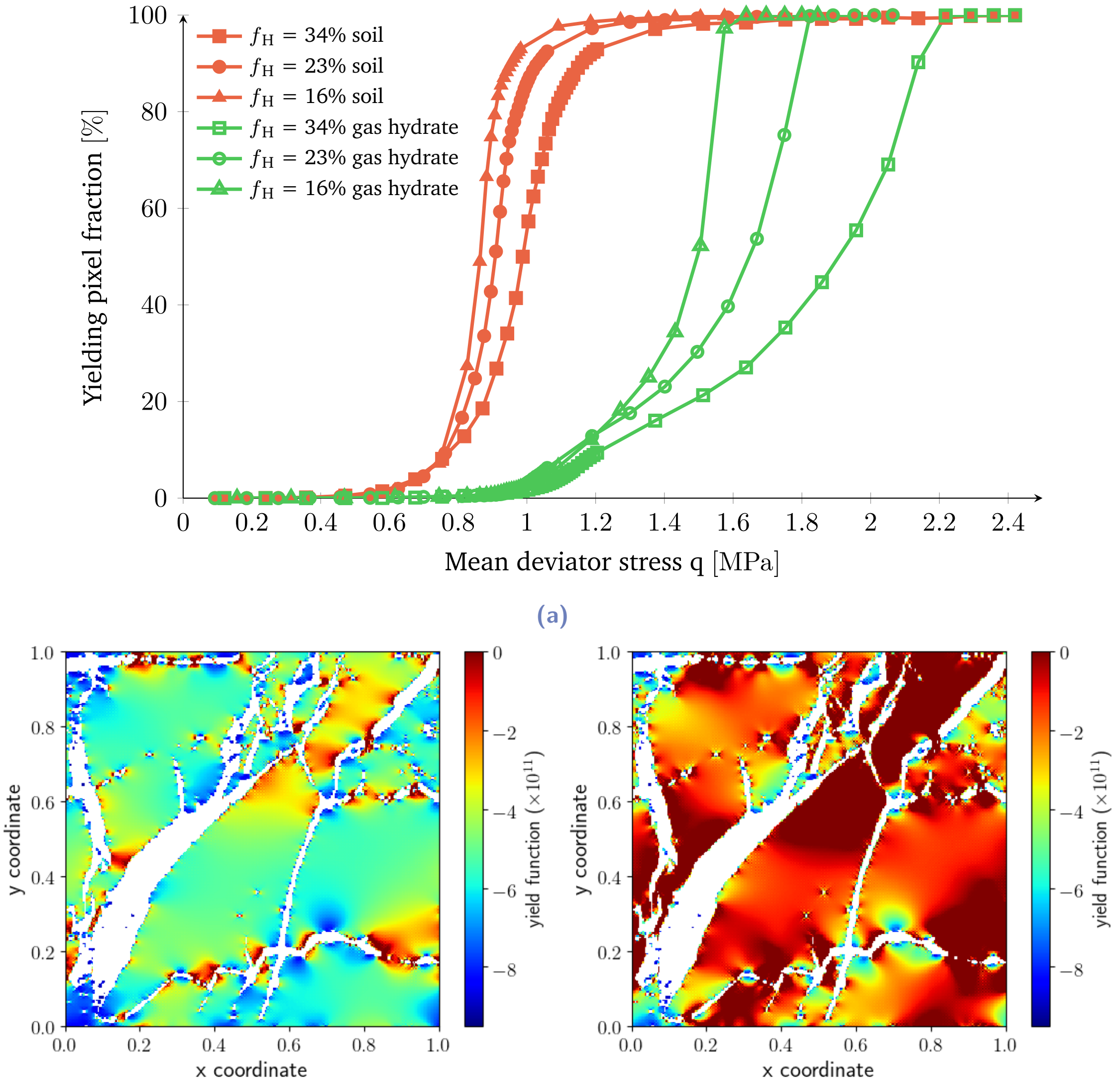

(b) E11=0.07%, q=0.62 MPa

(c) E11=0.11%, q=0.83 MPa

Fig. 5.12: (a) Evolution of the fraction of yielding pixels for each phase as a function of the mean deviator stress q; (b) and (c) represent the yield function distribution over the soil phase (Cam Clay) of the microstructure with 16% of gas hydrate volume fraction at two different stages of the shearing (resolution of 256 pixels; threshold value A).

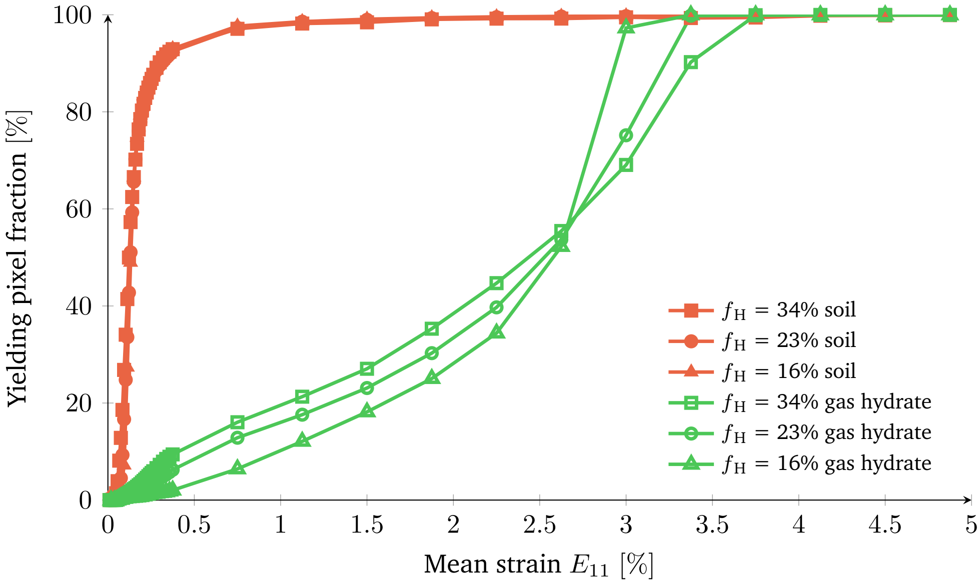

Fig. 5.13: Evolution of the fraction of yielding pixels for each phase as a function of the macroscopic strain component E_{11}.

5.4 Synchrotron images

In this section we studied cubic real images obtained with synchrotron-based x-ray tomography by a research team of our laboratory, working on the ANR HYDRE project, composed of Thi-Xu Le, Anh Minh Tang, Michel Bornert, Patrick Aimedieu, and Baptiste Chabot (Le, 2019; Le et al., 2019). We had access to three-dimensional images of a synthesised gas hydrate bearing sand sample (Fig. 5.14) (Le, 2019). They formed their sample by placing a wet sand (the reference sand called Fontainebleau sand) into a mold and by percolating methane gas at a pressure of 7 MPa and a temperature of 275 K into it. They let the system in these conditions long enough for the reaction to occur and for gas hydrates to form. The same team also performed triaxial tests on samples made up of the same reference sand both with synthesised gas hydrates in it and without gas hydrates. The results of these triaxial tests (Le, 2019) are represesented in Fig. 5.15 and have been used to calibrate our parameters.

5.4.1 Elastic calibrations

We worked with two substacks of synchrotron images at two different times of the formation stage. No mechanical tests were performed on the sample which was not submitted to any confining pressure during the image acquisition. Given the conditions, we suppose that the effective stresses in the solid grains were close to zero or negligible during the formation process. This means that the scanned sample was not exactly under the same conditions as the triaxial test conditions where confining pressure was equal to $10\mathrm{MPa}$, pore pressure was equal to $7\mathrm{MPa}$, and therefore effective pressure was equal to $3\mathrm{MPa}$. However we decided to calibrate our homogenisation calculations over the synchrotron images with the triaxial test results as they were obtained with the exact same protocols and materials. As a first step we had to segment the real images in order to get the exact number of colors corresponding to the exact number of phases, being three here as there were a sand grain phase, a methane hydrate phase and a void or fluid phase. The choices we made can be debated as the comparable densities of methane gas, liquid water and methane hydrates make it difficult to differentiate these phases in the segmentation process. The real porosity was known to be 40% to 41% in the sample (Le, 2019), but no other data like the local methane hydrate saturation was known for sure for the substack of images that we had. We have therefore chosen threshold values in order to get the target values of the known porosity and the artificial methane hydrate saturations given in Tab. 5.2 in the two substacks we had, as an application example because these saturation values were the ones established in the triaxial tests shown in Fig. 5.15.

Beforehand, as we did in the previous section with the hydrate veins, we have used a *periodic-plus-smooth decomposition* of the two substacks to obtain a three-dimensional periodic stack

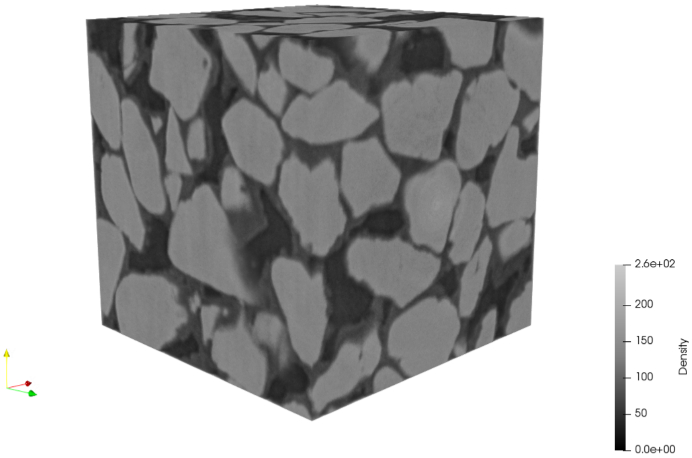

Fig. 5.14: Substack of synchrotron images at resolution 1024x1024x1024 pixels (data courtesy of Thi-Xiu Le and her team; Le, 2019).

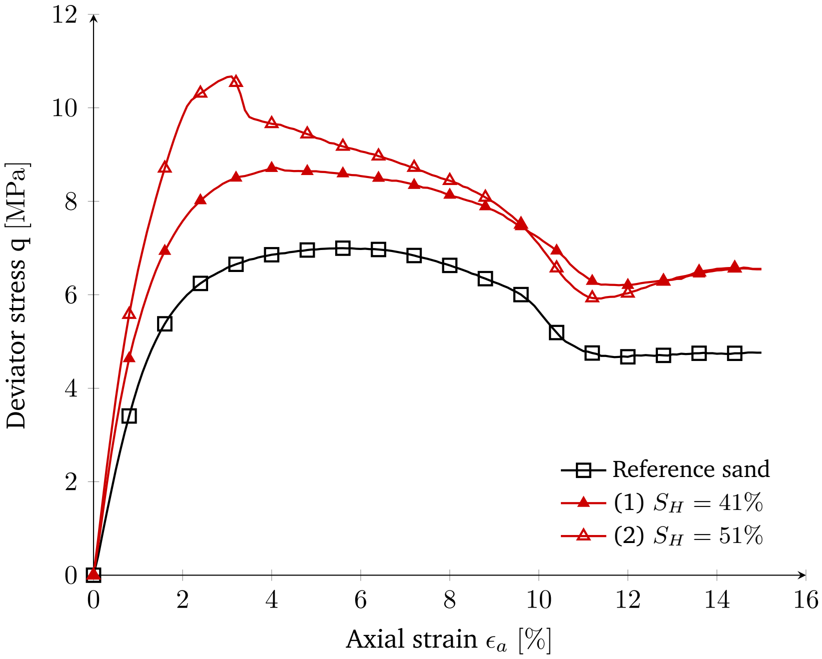

Fig. 5.15: Triaxial test results on synthetic gas hydrate bearing sand (Fontainebleau sand) with various values of gas hydrate saturations S_H (from Le, 2019).

Tab. 5.2: Targeted porosity and hydrate saturations for image segmentation.

Parameter	Sample 1	Sample 2
Hydrate saturation S_H	41%	51%
Porosity n	40-40%	

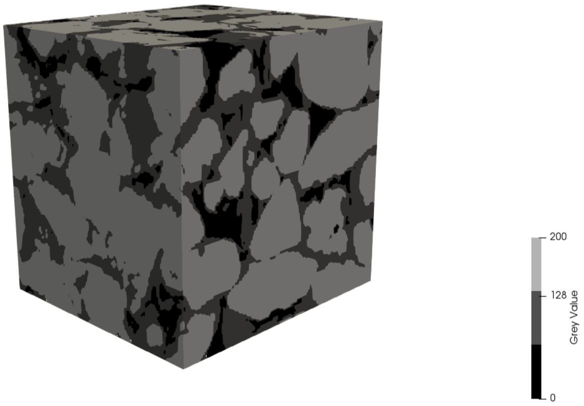

Fig. 5.16: Clip of modified (periodic and segmented) synchrotron images at resolution 128x128x128 pixels, the black color represents the void phase, the dark grey color represents the gas hydrate phase and the light grey color represents the sand grains.

Tab. 5.3: Calibrated elastic parameters of each material phase.

Phase	Young's modulus	Poisson's ratio
Sand	4.65 GPa	0.4
Hydrate	139 MPa	0.32

of images. This means that each two-dimensional image of the stack was periodic, and that in the cross sectional direction, the first and last images of the stack were corresponding too. Then, as 1024x1024x1024 resolution was too big for the memory capacity at our disposal, a mean reduction of the images to size 128x128x128 has been applied and the reduced image has been segmented. A clip of the resulting periodic segmented sample 1 is shown in Fig. 5.16, and one can observe that the images that are at the the borders or the faces of the cube are slightly disturbed as well as in the previous two-dimensional example.

After the image processing, we have homogenised the unit cell elastic behaviour without any hydrate phase, the material parameters of the hydrate phase were put to zero like in the void material, so we had a two-phase material : sand grains and voids. We have assumed an isotropic elastic local behaviour of the sand grains. We have determined the local elastic parameters of the sand grains by comparing the resulting macroscopic elastic moduli with the reference curve showed in black in Fig. 5.15. The comparative results for this first reference material is presented in Fig. 5.17 along with the second comparative results corresponding this time to the establishment of the local isotropic elastic parameters of the hydrate phase of the unit cell defined by $S_H = 41\%$. This second homogenisation calculation has been done with a three-phase unit cell with the previously calibrated parameters for the sand phase and non-zero values for the elastic parameters of the hydrate phase. The second triaxial curve has helped determine the latter parameters, and the calibrated local elastic moduli are summarised in Tab. 5.3.

Finally, we have used the calibration results (Tab. 5.3) as input parameters for the local elastic behaviour of the phases of the second microstructure with $S_H = 51\%$. The resulting

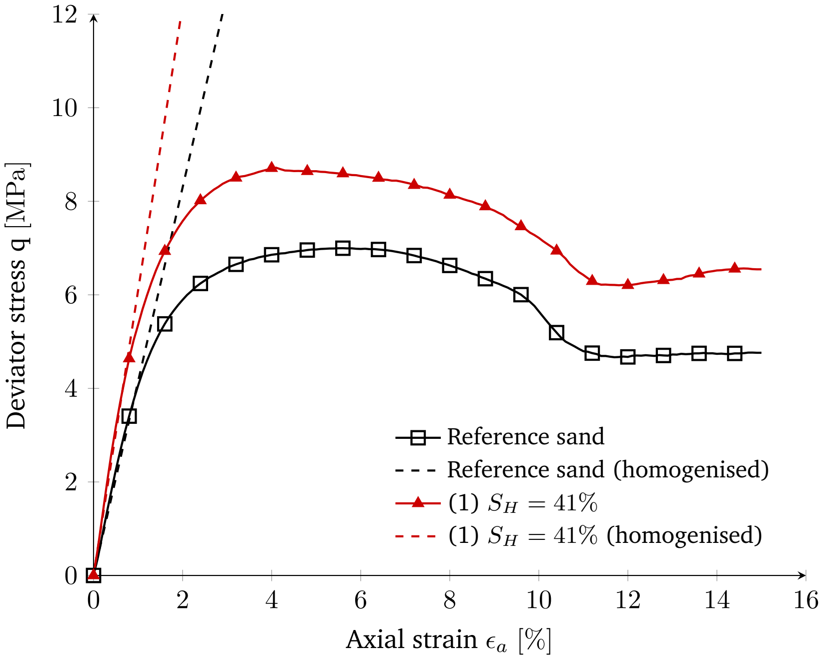

Fig. 5.17: Comparative results between real triaxial tests on synthetic methane gas hydrate bearing sand (Le et al., 2019) and homogenised elastic behaviour of voxelised unit cells made up of (dashed black line) sand grains and voids, and (dashed red line) sand grains, hydrates and voids.

predicted macroscopic stress-strain curve is compared to the triaxial test results in Fig. 5.18 and they are in good agreement with each other, the measured and homogenised Young's moduli are 725 MPa and 669 MPa respectively, the relative error being 7%.

5.4.2 Plasticity

After having determined the elastic local parameters of each material in the previous subsection, we have introduced a plastic criterion for the behaviour of the grains and the methane hydrate phase. All calculations were performed with a reduced resolution for the unit cell of 32x32x32 voxels while keeping the same porosity and hydrate saturation values as in the previous calculations. We simply investigated the feasibility and the interest of the method. In a first step we determined the local properties of the grains by comparing the homogenisation results with the triaxial curves like in Fig. 5.17 but, based on the triaxial test results for the reference sand, we assumed an elastic-perfectly plastic behaviour for the grains with a von Mises criterion. The unit cell with no methane hydrate phase was thus submitted to the following macroscopic loading corresponding to triaxial conditions:

$$E_{11} = 8\% \text{ and } \boldsymbol{\Sigma}_{ij} = 0 \quad \forall i \neq 1 \text{ or } j \neq 1 \tag{5.5}$$

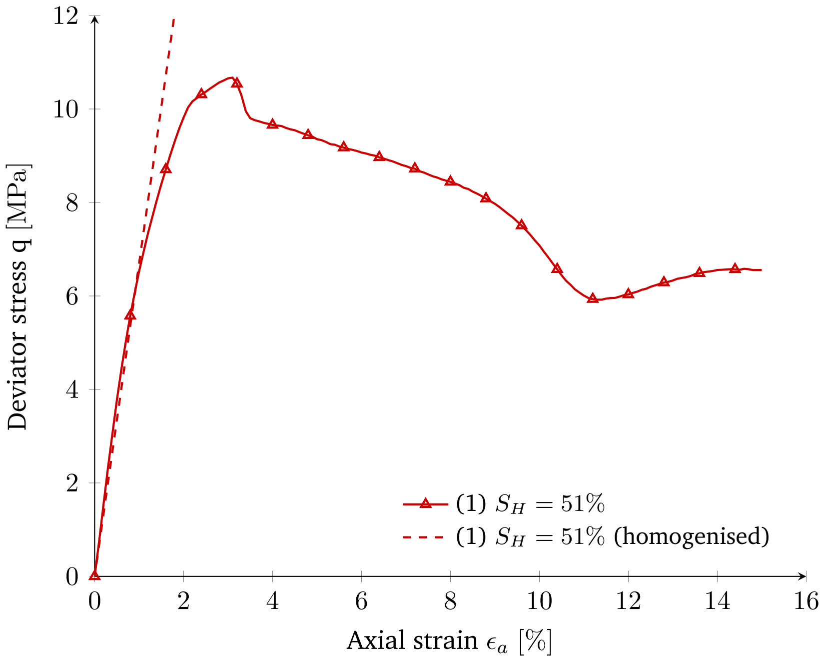

Fig. 5.18: Comparative results between real triaxial tests on synthetic methane gas hydrate bearing sand (Le et al., 2019) and predicted homogenised elastic behaviour of voxelised unit cells made up of sand grains, hydrates and voids, with a methane hydrate saturation of $S_H = 51\%$.

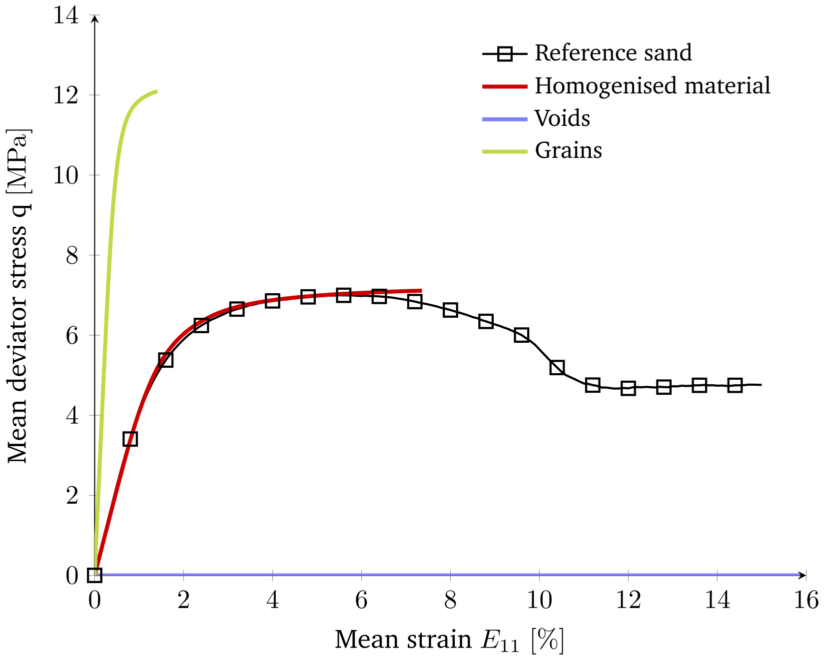

Fig. 5.19: Macroscopic stress-strain response of the homogenised synchrotron images in plasticity with two constituting phases: grains and voids.

Tab. 5.4: Material models and calibrated parameters of the grains and voids constituting the three-dimensional cell in plasticity.

Grains	Voids
Elastic perfectly plastic (von Mises)	Elastic
E_g = $2.45\mathrm{GPa}$	
ν_g = 0.4	0
σ_y = $40\mathrm{MPa}$	

Tab. 5.5: Material models and parameters of each constituting phase of the three-dimensional cell in plasticity.

Hydrates	Grains	Voids
Elastic perfectly plastic (von Mises)	Elastic perfectly plastic (von Mises)	Elastic
E_h = $200\mathrm{MPa}$	E_g = $2.45\mathrm{GPa}$	
ν_h = 0.32	ν_g = 0.4	0
σ_y = $2\mathrm{MPa}$	σ_y = $40\mathrm{MPa}$	

The average stress-strain responses over each phase and over the whole unit cell are shown in Fig. 5.19 and were obtained with the local material properties given in Tab. 5.4. The local parameters had to be changed from the ones of the previous fitting with a 128x128x128 pixels unit cell because the reduced resolution modifies the geometry and the mechanical response of the unit cell. In a second step we found the local parameters of the gas hydrate phase that we assumed elastic-perfectly plastic too, with the same plastic criterion as the grains. The fitted local parameters describing the behaviour of the grains in Tab. 5.4 were used for the calculations. The applied loading was the same as in Eq. 5.5.

Fig. 5.20 shows the macroscopic response of the unit cell and the average responses of each phase in comparison with the triaxial results obtained for a gas hydrate saturation of $S_H = 51\%$. The model properties used for the gas hydrate phase to obtain this curve are presented in Tab. 5.5. Looking at the average curve of the hydrate phase, one can see that voxels defined by the hydrate material have quickly reached the plastic criterion. The introduction of a nonlinear behaviour for the grains instead of the elastic model led to a less rigid macroscopic response of the unit cell. The local constitutive laws did not allow us to simulate the strain softening phenomena that appears in the triaxial curves, one possibility to achieve this would be to introduce a damage law for instance.

In a last step we used the local properties in Tab. 5.5 to homogenise the unit cell with a gas hydrate saturation of $S_H = 41\%$ in order to validate the fitted parameters. This second unit cell was also reduced to 32x32x32 pixels and subjected to the same loading as the one described in Eq. 5.5. The predicted response obtained by homogenisation calculation is shown with the triaxial test results for $S_H = 41\%$ in Fig. 5.21. There is a good agreement between the simulation and the experimental results.

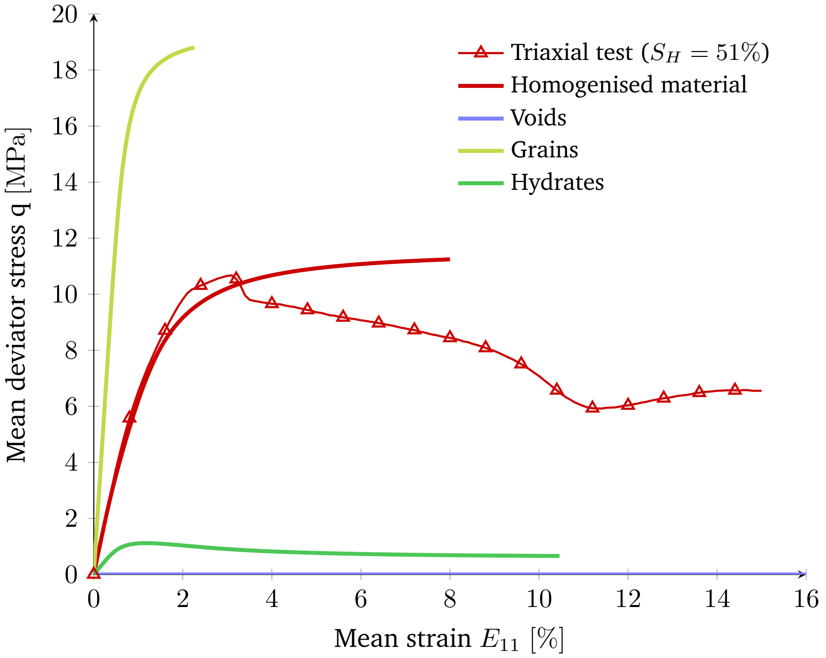

Fig. 5.20: Macroscopic stress-strain response of the homogenised synchrotron images in plasticity with three constituting phases: grains, gas hydrates and voids.

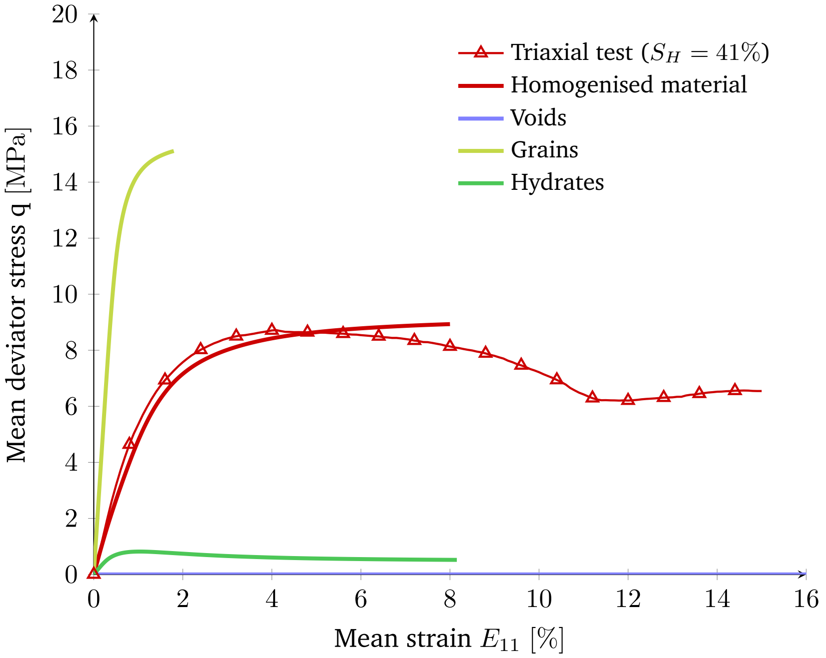

Fig. 5.21: Macroscopic stress-strain response of the homogenised synchrotron images in plasticity with three constituting phases: grains, gas hydrates and voids.

5.5 Conclusion

We applied a numerical homogenisation method to gas hydrate bearing sediments to overcome the experimental difficulties usually met in the study of these soils. The chosen FFT-based homogenisation method can help model the effective mechanical behaviour of different types of materials defined by complex microstructures that can be obtained from real images, thus avoiding the multiplication of experiments. This is an advantage especially for the modeling of fine sediments as it is still difficult to form gas hydrates in fine grained soils in laboratory. This is why we used the numerical method on real images from micro CT scans. We investigated the impact of different threshold values on the results. more elaborate method can be used to determine these threshold values in the future. As for granular soils, examples were given for schematic unit-cells formed with only few circular grains being surrounded by either cementing or load-bearing gas hydrates. Real images were also used to calibrate local mechanical models defining each material phase of the microstructure, meaning the sand grains, the gas hydrates and the voids or fluid phase.

The examples gave a good insight of the advantages and the potential of the method. Several applications to gas hydrates are possible such as multi-scale modeling or developing macroscopic laws based on microstructural particularities. In the next chapter we will introduce the multi-scale approach and more precisely a FEM-FFT multi-scale method.

6

Multi-scale FEM-FFT approach

6.1 Introduction

In this chapter we introduce the method that we have chosen in the framework of a two-scale model using a multi-scale FEM-FFT approach to compute the macroscopic mechanical response of a gas hydrate bearing sediment layer from its microscopic fields. In the FEM-FFT approach, the macroscopic mechanical problem is solved by the FEM using a macroscopic FE mesh and the macroscopic stress-strain constitutive equation is obtained through the resolution of a homogenisation problem on a microscopic periodic REV (Fig. 6.1). As seen in previous sections, the macroscopic and microscopic mechanical fields are linked by average calculations over the volume of the microscopic REV. Therefore, each integration point of the FEM is associated to a microscopic unit cell discretised into pixels or voxels for the purpose of FFT-based homogenisation calculations. The Newton-Raphson iterative algorithm used to solve the linearised macroscopic element equations (Potts and Zdravkovic, 1999)

$$[K_e]\,\{\varDelta u_e\} = \{\varDelta R_e\} \tag{6.1}$$

and obtain the element nodal displacements $\{\varDelta u_e\}$, requires both:

- the computation of the stress tensor increment $\varDelta \boldsymbol{\Sigma}$ at each integration point to compute the incremental element nodal forces $\{\varDelta R_e\}$

- the computation of the macroscopic tangent matrix $\overline{\mathbb{C}}$ at each integration point to compute the element stiffness matrix $[K_e]$:

$$\varDelta \boldsymbol{\Sigma} = \overline{\mathbb{C}} : \varDelta \boldsymbol{E} \tag{6.2}$$

The computation of $\varDelta \boldsymbol{\Sigma}$ is obtained by using any numerical periodic homogenisation method and by averaging the microscopic stress field $\boldsymbol{\sigma}$ over the unit cell. In our case this is done with the FFT-based homogenisation method presented in chapter 4. However the main issue in the development of a multi-scale code based on a Newton-Raphson algorithm at the macroscopic scale is the computation of the macroscopic tangent stiffness matrix $\overline{\mathbb{C}}$ at each integration point and each iteration. This usually implies an increase in the memory storage of the calculation and in the computational time.

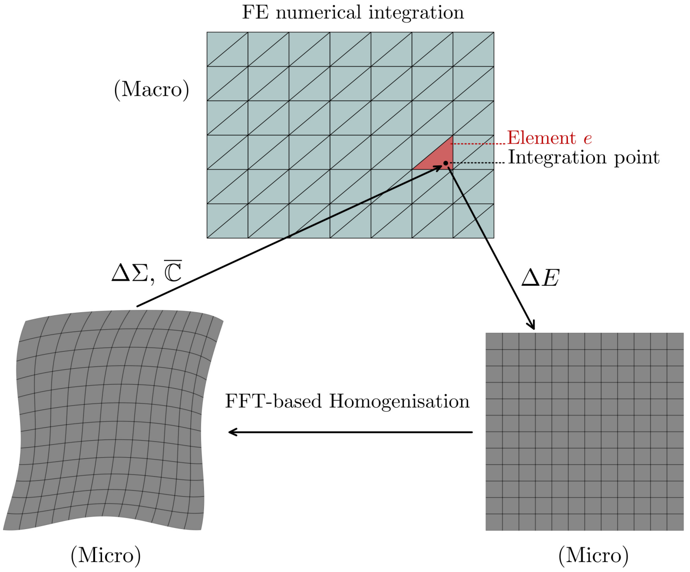

Fig. 6.1: Schematic of the FEM-FFT multiscale approach.

Several authors have developed methods to determine the tangent stiffness matrix, among which we can cite Kouznetsova et al. (2001) and Miehe (1996). Kouznetsova et al. (2001) proposed a technique in FEM to directly compute the macroscopic tangent stiffness matrix from the condensed global stiffness matrix of the microscopic REV in the resolution of the microscale problem. This method requires the computation of the Schur complement of the global stiffness matrix of the microscopic REV, involving the inversion of a matrix block whose size increases with the number of nodes of the mesh. Miehe (1996) proposed a perturbation technique based on forward finite differences approximation. Taking into account the strain tensor symmetries, a set of six different small perturbation loads $\delta E_{kl} \neq 0$ is imposed to the REV at the end of the current load with equilibrated stress fields; the corresponding incremental macroscopic stresses $\delta\boldsymbol{\Sigma}(\delta E_{kl})$ are obtained solving the six perturbated homogenisation problems at the microscale. The macroscopic tangent stiffness matrix is then obtained from the six different stresses via the approximation $\overline{\mathbb{C}}_{ijkl} \approx \dfrac{1}{|\delta E_{kl}|}\delta\boldsymbol{\Sigma}_{ij}$. This latter technique require more computational time as it implies six resolution steps but it remains more convenient than the previous one in terms of memory storage and does not require any expensive matrix inversion. Moreover it does not depend on the general resolution method and has been used in most of the multi-scale approaches with FFT-based homogenisation (Göküzüm and Keip, 2018). Göküzüm and Keip (2018) presented a new way of computing a consistent macroscopic tangent matrix for FFT-based homogenisation and compared it to the perturbation technique. We chose to use their method in the next sections.

One important principle in the first order homogenisation theory that we have been using here is the separation of scales (Geers et al., 2010; Bornert, 1996). This principle states that the typical length scale of the microscopic REV ℓ_m is much smaller than the characteristic length of the macroscopic field fluctuations ℓ_M, and that ℓ_m is large enough to be

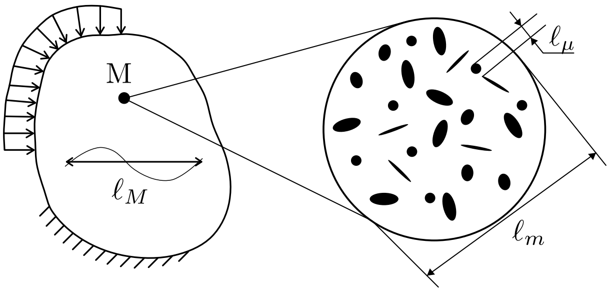

Fig. 6.2: Schematic of relevant length scales (Matouš et al., 2017)

statistically representative of the material morphology. The characteristic length scale of the microstructural morphology fluctuations can be introduced ℓ_μ, being for instance the distance between heterogeneities like pores or inclusions, and the scale separation can be written as the following inequalities (Geers et al., 2010), and represented as in Fig. 6.2:

$$\ell_\mu < \ell_m \ll \ell_M \tag{6.3}$$

The second inequality is an interpretation of the first order theory that leads to the assumption that the macroscopic strain is uniform over the microscopic REV geometry and that the microscopic stress, strain and displacement fields for example can be decomposed into their macroscopic part and a fluctuating part whose average is null over the REV like in $\boldsymbol{\epsilon} = \boldsymbol{E} + \boldsymbol{\epsilon}'$. The REV geometry at the microscopic scale or the length of variation of the macroscopic fields are then very important and have to respect this principle of separation of scales. Matouš et al. (2017) recalls for example that multi-scale problems applied to localisation of deformation or to large microstructural features violate the separation of scales. The morphology approximation of the microstructure and its length scale is usually determined through statistics to be considered as representative of the microscopic material. Microstructures can either be developed with molecular dynamics models, statiscal models or continuum models. In our case we use the continuum mechanics framework and we use schematic or real morphologies of microstructures as seen in the previous sections. The problem of realistic microstructures obtained with imaging methods such as micro-computed tomography is that the data are too large for numerical simulations (Matouš et al., 2017) and the reconstruction of representative sub-domains is a necessity. Unfortunately the determination of a representative unit cell has not been treated in this work, but is kept as an important aspect for future developments.

6.2 Tangent Matrix

6.2.1 Principle

In this section we present the method developed by Göküzüm and Keip (2018) to compute a consistent macroscopic tangent matrix using FFT-based homogenisation. We implemented this method in our FFT-based homogenisation code. They based their concept on the expression of a macroscopic tangent matrix from Miehe et al. (1999) in the large-strain setting, but it can also be applied to the small-strain setting. The expression is obtained from the following macroscopic linearised stress increment

$$\varDelta \boldsymbol{\Sigma} = \frac{\partial \boldsymbol{\Sigma}}{\partial \boldsymbol{E}} : \varDelta \boldsymbol{E} \tag{6.4}$$

and by recalling the definition of the macroscopic stress tensor in the homogenisation context

$$\boldsymbol{\Sigma} = \frac{1}{\varOmega} \int_{\varOmega} \boldsymbol{\sigma} \mathrm{d}\varOmega \tag{6.5}$$

which gives

$$\varDelta \boldsymbol{\Sigma} = \frac{1}{\varOmega} \left[\int_{\varOmega} \frac{\partial \boldsymbol{\sigma}(\boldsymbol{\epsilon})}{\partial \boldsymbol{\epsilon}} : \frac{\partial \boldsymbol{\epsilon}}{\partial \boldsymbol{E}} \mathrm{d}\varOmega \right] : \varDelta \boldsymbol{E} \tag{6.6}$$

and with the use of the microscopic strain decomposition $\boldsymbol{\epsilon} = E + \boldsymbol{\epsilon}'$ and the microscopic tangent stiffness matrix $\mathbb{C}^* = \dfrac{\partial \boldsymbol{\sigma}}{\partial \boldsymbol{\epsilon}}$ leads to:

$$\varDelta \boldsymbol{\Sigma} = \frac{1}{\varOmega} \left[\int_{\varOmega} \mathbb{C}^* \mathrm{d}\varOmega + \int_{\varOmega} \mathbb{C}^* : \frac{\partial \boldsymbol{\epsilon}'}{\partial \boldsymbol{E}} \mathrm{d}\varOmega \right] : \varDelta \boldsymbol{E} \tag{6.7}$$

Hence the expression of the macroscopic tangent matrix to compute:

$$\overline{\mathbb{C}} = \frac{1}{\varOmega} \left[\int_{\varOmega} \mathbb{C}^* \mathrm{d}\varOmega + \int_{\varOmega} \mathbb{C}^* : \frac{\partial \boldsymbol{\epsilon}'}{\partial \boldsymbol{E}} \mathrm{d}\varOmega \right] \tag{6.8}$$

Depending on the local mechanical model attributed to each pixel or voxel the tangent stiffness matrix $\mathbb{C}^*$ can either be known in closed-form or computed through different methods such as return mapping or substepping algorithms. However the computation of the partial derivative $\dfrac{\partial \boldsymbol{\epsilon}'}{\partial \boldsymbol{E}}$ is not straightforward. Göküzüm and Keip (2018) proposed to start from the identification of the fluctuating strains $\boldsymbol{\epsilon}'$ in Lippmann-Schwinger equation $\boldsymbol{\epsilon}' = -\boldsymbol{\varGamma}^0 * (\boldsymbol{\sigma} - \mathbb{C}^0 : \boldsymbol{\epsilon})$ and differentiate it as follows:

$$\frac{\partial \boldsymbol{\epsilon}'}{\partial \boldsymbol{E}} = -\varGamma^0 * \left(\frac{\partial \boldsymbol{\sigma}}{\partial \boldsymbol{\epsilon}} : \frac{\partial \boldsymbol{\epsilon}}{\partial \boldsymbol{E}} - \mathbb{C}^0 : \frac{\partial \boldsymbol{\epsilon}}{\partial \boldsymbol{E}} \right) \tag{6.9}$$

The equation can then be transformed using the strain decomposition again and be arranged as

$$-\varGamma^0 * \left(\mathbb{C}^* - \mathbb{C}^0 \right) = \varGamma^0 * \left((\mathbb{C}^* - \mathbb{C}^0) : \frac{\partial \boldsymbol{\epsilon}'}{\partial \boldsymbol{E}} \right) + \frac{\partial \boldsymbol{\epsilon}'}{\partial \boldsymbol{E}} \tag{6.10}$$

Eq. 6.10 can be seen as a linear equation $\boldsymbol{A} \cdot X = B$ with respect to $X \equiv \dfrac{\partial \boldsymbol{\epsilon}'}{\partial \boldsymbol{E}}$ where

$$\boldsymbol{A} \cdot X \equiv \mathit{\Gamma}^0 * \left((\mathbb{C}^* - \mathbb{C}^0) : \frac{\partial \boldsymbol{\epsilon}'}{\partial \boldsymbol{E}} \right) + \frac{\partial \boldsymbol{\epsilon}'}{\partial \boldsymbol{E}} \tag{6.11}$$

$$B \equiv -\mathit{\Gamma}^0 * \left(\mathbb{C}^* - \mathbb{C}^0 \right) \tag{6.12}$$

As in the Lippmann-Schwinger equation, the above expressions involve a convolution product with the Green operator, and it can be solved with the use of a conjugate gradient method combined with forward and backward FFT, with the null average constraint:

$$\overline{\left(\frac{\partial \boldsymbol{\epsilon}'}{\partial \boldsymbol{E}} \right)} = \frac{1}{\mathit{\Omega}} \int_{\mathit{\Omega}} \frac{\partial \boldsymbol{\epsilon}'}{\partial \boldsymbol{E}} \mathrm{d}\mathit{\Omega} = 0 \tag{6.13}$$

This amounts to imposing $\dfrac{\widehat{\partial \boldsymbol{\epsilon}'}}{\partial \boldsymbol{E}}(\xi = 0) = 0$ in Fourier space.

The partial derivative $\dfrac{\partial \boldsymbol{\epsilon}'}{\partial \boldsymbol{E}}$ that the we are looking for in order to compute the macroscopic tangent matrix $\overline{\mathbb{C}}$ is a fourth order tensor that needs to be found for each pixel or voxel of the microscopic geometry. This represent a linear system of $N_1 \times ...N_{dim} \times n_{dim}^4$ equations to solve with n_{dim} the number of spatial dimension of the local problem and N_i the resolution number in the direction i (number of pixels or voxels). Such problem implies a higher memory storage than the resolution of the six perturbation equations, but it only requires the resolution of one linear equation whereas the six perturbation equations require the local resolution of non-linear equations for non-linear materials of some pixels. To compute it we use the Newton-Raphson iteration step where the macroscopic stress $\mathit{\Delta}\boldsymbol{\Sigma}$ is computed using the FFT-based algorithm from the macroscopic strains $\mathit{\Delta}\boldsymbol{E}$. From this step, the fields $\boldsymbol{\sigma}$ and $\boldsymbol{\epsilon}$ solution of the local mechanical problem under the current load step have been found iteratively and the last iteration of the solving method over the microscopic scale can lead to the local tangent operator $\mathbb{C}^*$ distribution.

6.2.2 Computation

The calculation therefore consists in computing the right hand side of the problem at each pixel or voxel using the local tangent stiffness matrices at each pixel (or voxel), one forward FFT, followed by the double dot product with the Green operator in Fourier space and finally using the backward FFT:

$$\mathbb{B}(x) = \mathbb{C}^*(x) - \mathbb{C}^0 \quad \forall x \in \mathit{\Omega} \tag{6.14}$$

$$\longrightarrow FFT(\mathbb{B}) \tag{6.15}$$

$$\hat{\mathbb{B}}(\xi) = -\mathit{\Gamma}^0(\xi) : \hat{\mathbb{B}}(\xi) \quad \forall \xi \in \mathit{\Omega} \tag{6.16}$$

$$\longrightarrow FFT^{-1}(\hat{\mathbb{B}}) \tag{6.17}$$

The right hand side $\mathbb{B}$ is a fourth order tensor field. The FFT are computed with the functions of the C open source library fftw3 (Frigo and Johnson, 2005) just like for the previous parts of the FFT-based homogenisation code.

Once the right hand side of the function has been computed and stored in a $N_1 \times ...N_{dim} \times n_{dim}^4$ array, it is passed as an argument to the Stabilised BiConjugate Gradient solver of the C open source library PETSc (Balay et al., 2019), along with the 'matrix-vector product' function corresponding to $\boldsymbol{A} \cdot x$, which we rename $\boldsymbol{A} \cdot \mathbb{X}$ as the unknown is a fourth order tensor field. Again, there is no need to compute the matrix $\boldsymbol{A}$ with the conjugate gradient-based method here. The function $\boldsymbol{A} \cdot \mathbb{X}$ is also stored in a fourth order tensor field $\mathbb{Y}$ and computed as follows:

$$\mathbb{Y}(x) = (\mathbb{C}^*(x) - \mathbb{C}^0) : \mathbb{X}(x) \quad \forall x \in \Omega \tag{6.18}$$

$$\longrightarrow FFT(\mathbb{Y}) \tag{6.19}$$

$$\hat{\mathbb{Y}}(\xi) = -\Gamma^0(\xi) : \hat{\mathbb{Y}}(\xi) \quad \forall \xi \in \Omega \tag{6.20}$$

$$\longrightarrow FFT^{-1}(\hat{\mathbb{Y}}) \tag{6.21}$$

$$\mathbb{Y}(x) = \mathbb{Y}(x) - \mathbb{X}(x) \quad \forall x \in \Omega \tag{6.22}$$

In the above processes the evaluated tensor fields were presented as continuous functions of real (x) and Fourier (ξ) spaces to be clear, but in practice the equations and fields are discretised exactly in the same way as in the chapter 4, with pixel-wise constant tensor fields. Which means that the solution $\mathbb{X} = \dfrac{\partial \epsilon'}{\partial \boldsymbol{E}}$ and the local microscopic tangent stiffness tensors $\mathbb{C}^*$ are, for example in 2D, the discrete sequences:

$$\{\mathbb{X}_{ab}\}_{(a,b) \in [\![0;N_1[\![\times [\![0;N_2[\![} \tag{6.23}$$

$$\{\mathbb{C}^*_{ab}\}_{(a,b) \in [\![0;N_1[\![\times [\![0;N_2[\![} \tag{6.24}$$

for a discrete 2D geometry of size $N_1 \times N_2$ pixels. And finally, when the set of linear equations is solved, the solution sequence and the local tangent stiffness matrix sequence are used to compute the macroscopic tangent stiffness matrix based on Eq. 6.8:

$$\overline{\mathbb{C}} = \frac{1}{N_1 N_2} \sum_{a=0}^{N_1} \sum_{b=0}^{N_2} [\mathbb{C}^*_{ab} + \mathbb{C}^*_{ab} : \mathbb{X}_{ab}] \tag{6.25}$$

In their article, Göküzüm and Keip (2018) verified their algorithm by comparing the algorithmically obtained macroscopic tangent stiffness matrix to Eshelby analytical solution for the elastic case of a dilute distribution of stiff spherial inclusions in a matrix. We did the same to verify our code and got the same results as Göküzüm and Keip (2018).

6.3 Two-scale FEM-FFT approach

6.3.1 Implementation

The FFT-based code, with the addition of the above computation of the macroscopic tangent stiffness matrix, is incorporated into a mechanical model of the finite element software Bil. When initialising the calculation, a table of $N_1 \times ... \times N_{dim} \times N_{var}$ is attributed to each integration point of elements whose material is defined by a micro-macro mechanical homogenisation, with N_{var} being the number of data variables that we need to store.

Here, N_{var} corresponds to the components of the following variables

$$\{\boldsymbol{\epsilon}(t_n), \boldsymbol{\sigma}(t_n), p(t_n), \boldsymbol{\epsilon}(t_{n-1}), \boldsymbol{\sigma}(t_{n-1}), p(t_{n-1})\}.$$

The internal variables p depend on the local constitutive models. If it is elastic we don't need p, but if the constitutive model is nonlinear like an elastic-perfectly plastic model with Drucker-Prager's criterion for instance, we need to store the yield function value y along with the plastic strains at both current and previous time steps $\boldsymbol{\epsilon}^p(t_n)$ and $\boldsymbol{\epsilon}^p(t_{n-1})$.

The $N_1 \times ... \times N_{dim}$ Green operators $\{\mathit{\Gamma}_{ab}\}$ are computed at initialisation and the n_{dim}^4 components of each of them are allocated, but once and not at each integration point.

Only temporary allocations are needed to compute the macroscopic tangent stiffness matrix which is then stored in allocated space memory of the FEM at macroscale.

6.3.2 First Results

Preliminary results are presented here. The multi-scale model has been developed at the end of this PhD work, and we have not applied it to gas hydrate bearing sediments yet. In this section we applied the FEM-FFT model to a simple 2D geometry made up of two quadrangle elements. Two different microstructures are attributed to the elements, both defined by a 2D matrix-circular inclusion geometry with a resolution of 128x128 pixels but with a distinct volume fraction or radius for the inclusion (Fig. 6.3). The material properties of the phases constituting the microstructures are the same and there is only a difference in the size of the inclusion, one representing a volume fraction of 20% of the unit cell and the other 1% of the unit cell. The constitutive model of the matrix is elastic-perfectly plastic with the same von Mises' criterion as the one seen in previous sections and the inclusion has an isotropic linear elastic behaviour. The properties are given in Tab. 6.1, and the micro-scale FFT-based homogenisation is performed with the rotated Green operator.

Tab. 6.1: Parameters of the two-phase matrix-inclusion microstructures used for the homogenisation calculations at the micro-scale.

Phase	Young modulus	Poisson's ratio	yield strength (von Mises' criterion)
matrix	$E_m = 2.67\mathrm{GPa}$	$\nu_m = 0.33$	$\sigma_y = 5\mathrm{MPa}$
inclusion	$E_i = 13.33\mathrm{GPa}$	$\nu_i = 0.33$	

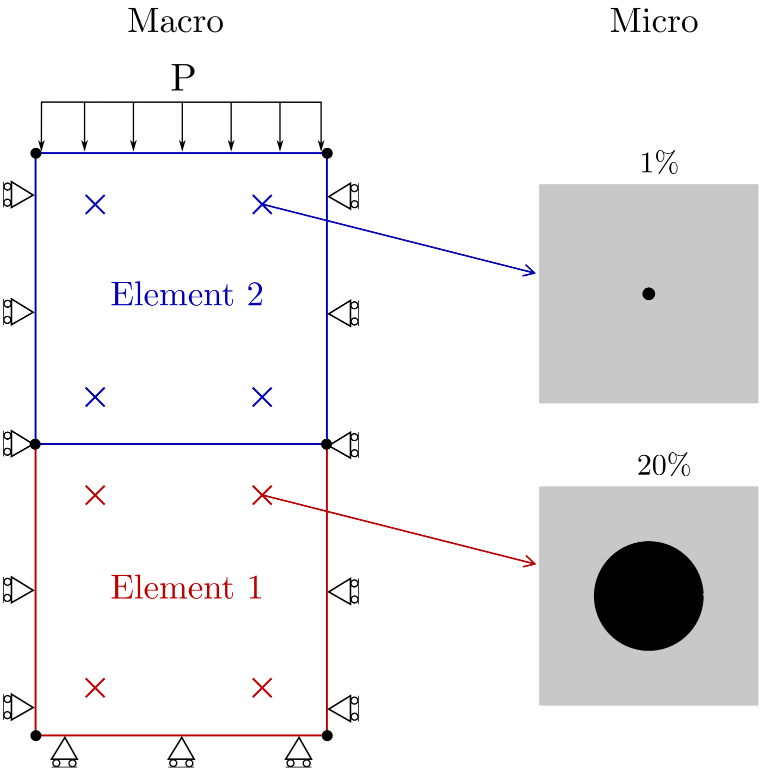

Fig. 6.3: Schematic of the two-scale problem with the two macroscopic elements and the initial microscopic matrix-inclusion geometries of the microscale. The macroscopic boundary conditions are also represented here.

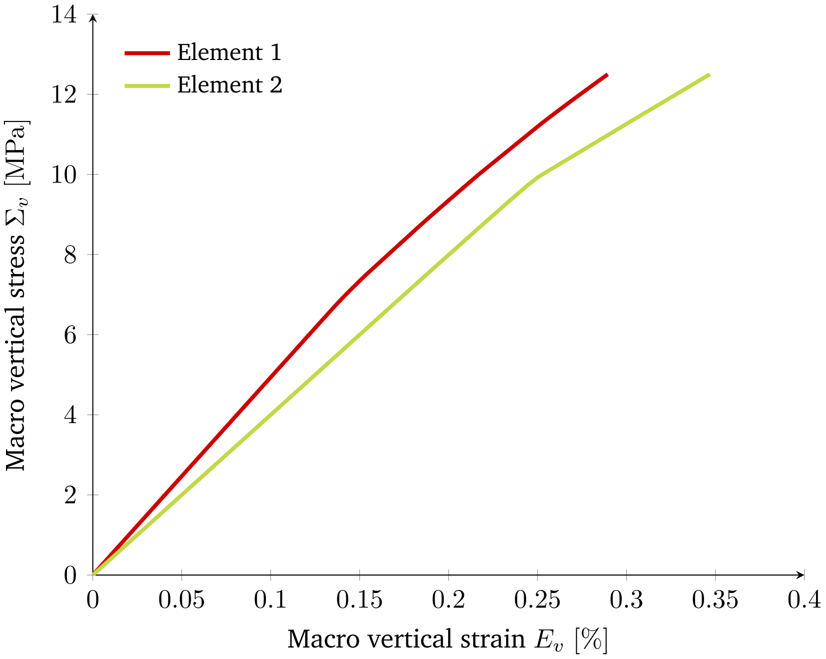

Fig. 6.4: Macroscopic vertical stress-strain response of the two elements of the FE mesh.

During the computation of the FEM at the macro-scale, 4 integration points are defined for each element which represents a total of 8 FFT-based homogenisation calculations at each Newton-Raphson iteration for each time-step. The macroscopic loading is a kind of oedometer test, the corresponding boundary conditions are given in Fig. 6.3, where a vertical pressure of 12.5 MPa is applied on top of the geometry.

The results for the elements 1 and 2 are given in Fig. 6.4 and Fig. 6.5 where we can see the nonlinear macroscopic response induced by the yielding of the microscopic matrix phase. Fig. 6.4 represents the macroscopic vertical stress as a function of the vertical strain while Fig. 6.5 represents the macroscopic deviator stress evolution as a function of the vertical strain. As expected, the response of the element 1 is stiffer than the second element since its associated microstructure contains a higher volume fraction of inclusions which have a stiffer behaviour than the microscopic matrix material. One can also see on the deviator curves (Fig. 6.5) that the mean deviator stress of the element 2 has reached the yield strength value. If we look at the distribution of the yield criterion at the microscale for both elements we can see that all the matrix phase is yielding at the end of the loading.

This simple application case has allowed us to verify that the FEM-FFT code was working, but still need some optimisation concerning memory storage and computational time that we will take care of before applying it to larger meshes and more complex microstructures than the ones presented in the previous chapter concerning the gas hydrate bearing sediments.

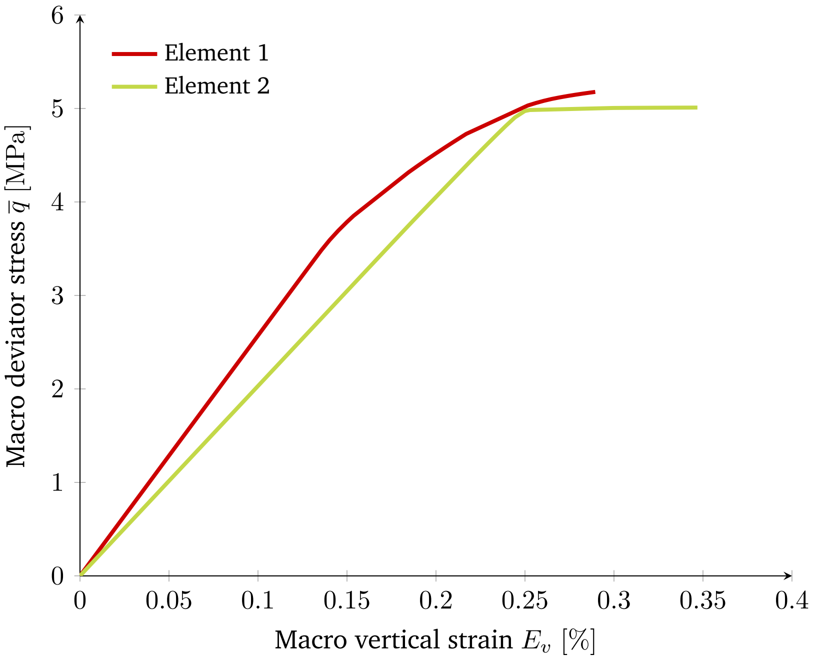

Fig. 6.5: Resulting macroscopic deviator stress as a function of the vertical strain represented for the two elements constituting the FE mesh.

(a) Element 1 - $P = 7.5\mathrm{MPa}$ **(b)** Element 2 - $P = 7.5\mathrm{MPa}$

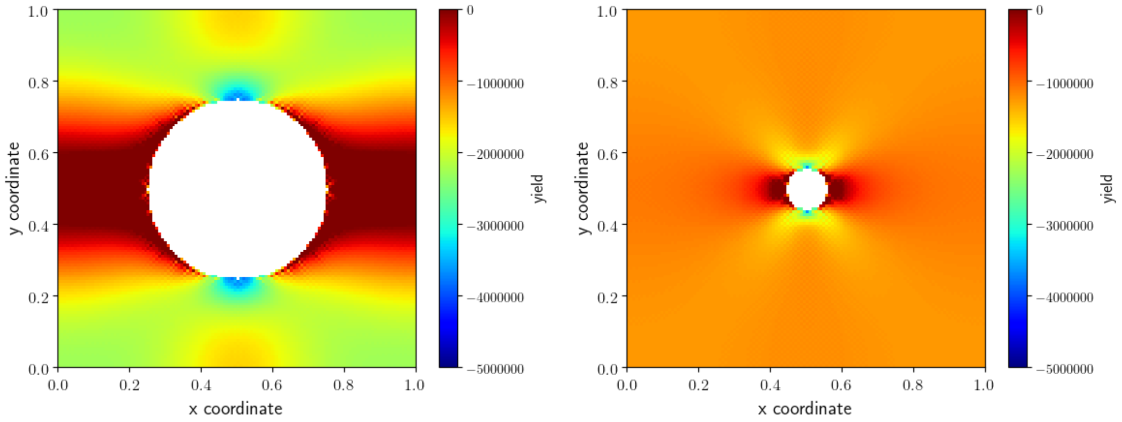

(c) Element 1 - $P = 10\mathrm{MPa}$ **(d)** Element 2 - $P = 10\mathrm{MPa}$

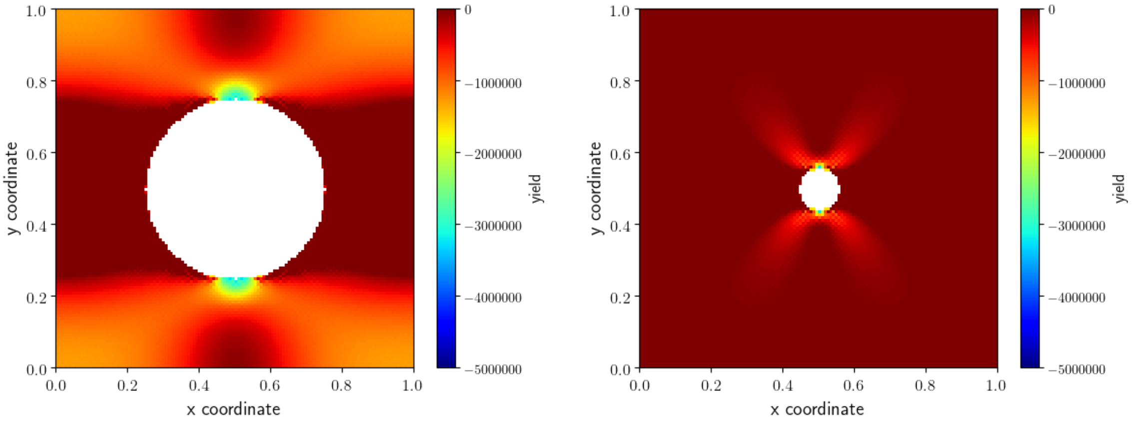

(e) Element 1 - $P = 12.5\mathrm{MPa}$ **(f)** Element 2 - $P = 12.5\mathrm{MPa}$

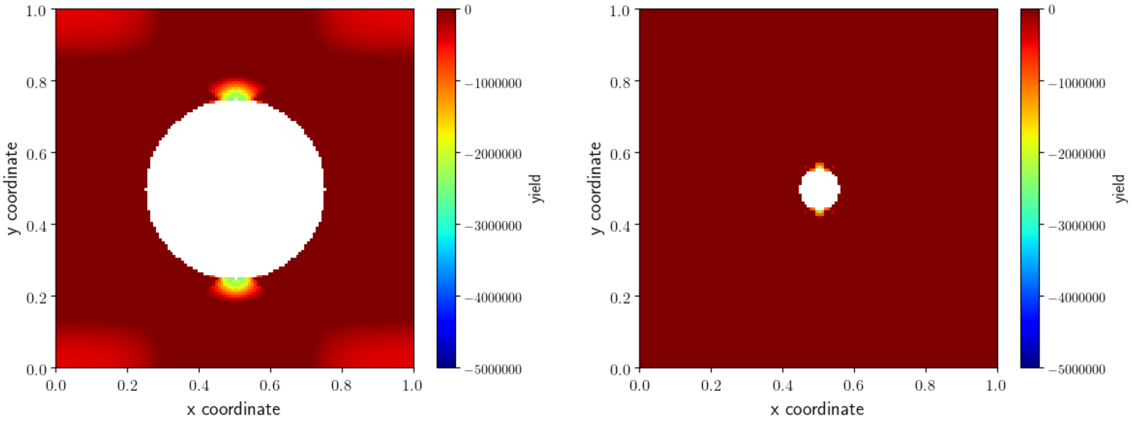

Fig. 6.6: Distribution of the yield criterion over both microstructures at one given integration point of element 1 and 2 respectively, and at three different loading steps.

6.4 Conclusion

In this chapter we presented the multi-scale principle and in particular the FEM-FFT code that we have developed by combining the FFT-based homogenisation code presented in the previous chapters and the FE simulation software Bil developed in the laboratory. We used the algorithm proposed by Göküzüm and Keip (2018) to compute a consistent macroscopic tangent stiffness matrix that is necessary for the macroscopic Newton-Raphson solving method. A simple case of application has been shown in the end, but the idea for the future is to apply this two-scale model to gas hydrate laboratory samples for the macro-scale with different realistic microstructures of gas hydrate bearing sediments at the micro-scale. This method would be particularly interesting for the modeling of heterogeneous gas hydrate bearing soil samples, even for the modeling of these soils at the scale of the reservoir but this would require sufficient computational resources.

Conclusions and Perspectives (English)

7

7.1 Thesis contributions

This work aims to model the mechanical behaviour of gas hydrate bearing sediments in order to prevent possible environmental problems caused by hydrate instability. The latter form in the pores of sediments in various morphologies and can modify the behaviour of these soils. Several studies have shown, for example, that at fixed temperature and pressure conditions, soils with a high hydrate content were more rigid and had a higher strength than soils with a lower hydrate content, or even no hydrates at all. The very heterogeneous microstructure of soils containing gas hydrates influences the macroscopic response of these materials. We have therefore chosen to use micro-mechanical approaches to model the effective behaviour of these sediments. First-order homogenisation theory is applied first by analytical and then numerical approaches to simulate the responses of soils defined by microstructures with gas hydrates.

The implementation of an analytical approach presented in chapter 3 provides a practical and inexpensive way to evaluate the effective elastic moduli of sediments represented by models of matrices with hydrate inclusions. But this approach has its limitations, especially for the geometry of microstructures, and the actual highly non-linear behaviour of gas hydrate-rich sediments cannot be simulated with it. Especially in the case of fine sediments with gas hydrates, ellipsoidal geometric inclusion models, for example, are not suitable.

The periodic homogenisation based on Fast Fourier Transforms that is presented in the chapter 4 offers an interesting alternative and has the advantage of not requiring any mesh and can be applied to real images for microstructures. In particular, the Gélébart and Mondon-Cancel (2013) method is implemented in a C language code that is validated by comparison with homogenisation results obtained via a finite element simulation on simple circular inclusion morphologies. The application of the FFT-based homogenisation code to more realistic microstructures in the chapter 5 allows to characterise the behaviour of the microstructure and analyse its effects on a macroscopic scale. This means of calculation makes it possible to compensate for the experimental difficulties associated with the study of soils containing gas hydrates. Complex microstructures, based on the processing of real images in particular, such as those obtained in task 2 of the ANR HYDRE project financing this thesis, can be analysed and subjected to several loading conditions through calculation.

One of the advantages of the homogenisation method presented in chapter 4 and of the code that has been developed for the application of this method is the multi-scale approach. The chapter 6 introduces the principle of multi-scale numerical computation, especially in the case of a resolution of the macroscopic problem by the finite element method using the Newton-Raphson algorithm. This algorithm requires the evaluation of the macroscopic tangent stiffness matrix from the microstructure at each mesh integration point. We therefore implement in our code a method developed by Göküzüm and Keip (2018) for the evaluation of this macroscopic tangent matrix in the context of homogenisation based on FFT. Finally, the developed homogenisation code is linked as a shared library to a finite element simulation software of the laboratory called Bil in order to design a FEM-FFT two-scale model. Preliminary test calculations using this model are presented at the end of the chapter.

7.2 Limitations and possible improvements

The FFT-based homogenisation code developed during the thesis is based on the theory of continuum mechanics, which obviously raises problems when applied to granular media for instance. Contact induced phenomena cannot be taken into account. In addition, the regular grid discretisation into pixels or voxels requires making choices on the distribution of local constitutive laws, especially for pixels or voxels that are found at the interfaces between different phase materials. One possibility for improving the method would be to define interface materials, as already applied in other studies.

The use of micro-mechanical methods ultimately requires rather little input data compared to advanced macroscopic models, but it also requires a knowledge of the local behaviour of each phase of the microstructure, which is not necessarily obvious in the case of hydrates. There are relatively few studies, particularly for the characterisation of the mechanical behaviour of pure hydrate crystals. The work of Task 1 of the ANR HYDRE project, which focuses on gas hydrate studies at the micrometer scale, has produced results that could remedy this problem, or at least nourish discussions on the selection of suitable models.

In addition, homogenisation computation times can become quite important when increasing the resolution of geometries, which is why the code still needs to be optimised for the memory allocated but also for the management of processes. Parallelisation of the code could be an area for improvement. Parallelisation of the FEM calculation at the macrostructure level in the multiscale approach is also important.

The application of the code to real microstructures was presented in chapter 5 but this involves making choices in image processing before calculation. These choices may have consequences on the macroscopic response of the homogenised medium, which is why this point should be clarified, in particular by applying rules borrowed from statistical mechanics to the question of the representativity of the unit cell.

7.3 Perspectives

For future applications of the code developed during the thesis, it may be interesting to develop macroscopic mechanical constitutive laws for sediments containing gas hydrates for different types of microstructures, based on homogenisation calculations under several macroscopic loads. The theory of homogenisation can also be applied to fluid mechanics problems, so a continuation of this thesis work would be to extend the application of the code to this area since transport phenomena also play a significant role in the behaviour of sediments containing gas hydrates. This would help characterise properties such as the permeability of these soils and provide additional analysis to the experimental tests that are still difficult to perform due to the extreme conditions required to maintain the stability of gas hydrates.

The application of the multi-scale model presented in chapter 6 is contemplated for simulations of laboratory specimens subjected to triaxial tests when specimens are heterogeneous, which can be the case with real samples or even synthetic gas hydrate bearing soils. These specimens could be defined by different microstructures typical of sediments containing gas hydrates, and by different volume fractions of the phases constituting the global material. In particular the modeling of fine soils containing gas hydrates with the multi-scale approach could be particularly interesting as there are still difficulties to synthesise gas hydrates in these soils. The results of computed tomography observations such as those reported in Task 2 of the ANR HYDRE project can provide the data necessary for the definition of the microstructures. Finally, in the long-term, a larger-scale application is also possible, to simulate the behaviour of reservoirs, for example by adding other physical phenomena at the macroscopic level such as thermodynamic or transport phenomena.

7

Conclusions et Perspectives (français)

7.1 Apports de la thèse

Ce travail s'attache à modéliser le comportement mécanique des sédiments riches en hydrates de gaz dans le but de pouvoir prévenir les éventuels problèmes environnementaux posés par l'instabilité des hydrates. Ces derniers se forment dans les pores des sédiments sous différentes morphologies et peuvent modifier le comportement de ces sols, plusieurs études ont montré par exemple qu'à des conditions de température et pression fixes, les sols avec une forte teneur en hydrates étaient plus rigides et plus résistants que des sols à plus faible teneur en hydrates, ou sans hydrates. La microstructure très hétérogène des sols contenant des hydrates de gaz a une influence sur la réponse macroscopique de ces matériaux. Nous avons donc choisi d'utiliser les approches micro-mécaniques pour modéliser le comportement effectif de ces sédiments. La théorie d'homogénéisation du premier ordre est appliquée d'abord par approche analytique puis numérique afin de simuler les réponses de sols définis par des microstructures avec hydrates de gaz.

La mise en place d'une approche analytique présentée au chapitre 3 offre un moyen pratique et peu couteux en calcul d'évaluer les modules élastiques effectifs des sédiments représentés par des modèles de matrices de sol avec inclusions d'hydrates. Mais cette approche a ses limites, notamment pour la géométrie des microstructures, et le comportement réel fortement non-linéaire des sédiments riches en hydrates de gaz ne peut être simulé. En particulier dans le cas des sédiments fins avec hydrates de gaz, les modèles d'inclusions géométriques ellipsoïdales par exemple ne sont pas adaptées.

L'homogénéisation périodique basée sur les Transformées Rapides de Fourier qui est présentée dans le chapitre 4 offre une alternative intéressante et qui présente l'avantage de ne nécessiter aucun maillage et de pouvoir être appliquée à des images réelles de microstructures. En particulier, la méthode de Gélébart and Mondon-Cancel (2013) est implémentée dans un code en langage C qui est validé par comparaison aux résultats d'homogénéisation obtenus via un code de calcul aux éléments finis sur des morphologies simples d'inclusions circulaires. L'application du code d'homogénéisation avec Transformées de Fourier à des microstructures plus réalistes dans le chapitre 5 permet de caractériser le comportement de la microstructure et analyser ses effets à l'échelle macroscopique. Ce moyen de calcul permet de compenser les difficultés expérimentales liées à l'étude des sols contenant des hydrates de gaz. Des microstructures complexes, basées sur le traitement d'images réelles notamment, comme celles obtenues dans la tâche 2 du projet ANR HYDRE qui finance cette thèse, peuvent être analysées et sollicitées soumises à plusieurs conditions de chargement par le calcul.

Un des intérêts de la méthode d'homogénéisation présentée au chapitre 4 et du code qui a été développé pour l'application de cette méthode est l'approche multi-échelle. Le chapitre 6 introduit le principe des calculs numériques multi-échelle, en particulier dans le cas d'une résolution du problème macroscopique par la méthode des éléments finis faisant intervenir l'algorithme de Newton-Raphson. Cet algorithme requiert l'évaluation de la matrice de rigidité tangente macroscopique issue de la microstructure en chaque point d'intégration du maillage. Nous implémentons donc dans notre code une méthode dévelopée par Göküzüm and Keip (2018) pour l'évaluation de cette matrice tangente macroscopique dans le cadre de l'homogénéisation basée sur les transformées de Fourier rapides. Finalement le code de calcul d'homogénéisation développé est lié en tant que bibliothèque partagée à un logiciel de calcul aux éléments finis du laboratoire appelé Bil afin de concevoir un modèle à deux échelle Eléments Finis-Transformées de Fourier. Des calculs préliminaires d'essai de ce modèle sont présentés en fin de chapitre.

7.2 Limites et améliorations

Le code d'homogénéisation par transformées de Fourier rapides développé lors de la thèse est notamment basé sur la théorie des milieux continus, ce qui pose évidemment des problèmes lors de son application à des milieux granulaires notamment. Les effets de contacts ne peuvent être pris en compte. Par ailleurs la discrétisation en grille régulière de pixels ou voxels impose de faire des choix sur la distribution des lois constitutives locales, surtout pour les pixels ou voxels qui se retrouvent aux interfaces entre différents matériaux de phases. Une possibilité d'amélioration de la méthode serait de définir des matériaux d'interface, comme cela est déjà appliqué dans d'autres études.

L'utilisation des méthodes micro mécaniques demande finalement assez peu de données d'entrée si l'on compare à des modèles macroscopiques avancés, mais elle requiert par ailleurs une connaissances du comportement local de chaque phase de la microstructure, ce qui n'est pas forcément évident dans le cas des hydrates. Assez peu d'études existent notamment pour la caractérisation du comportement mécanique des cristaux d'hydrates purs, les travaux de la tâche 1 du projet ANR HYDRE qui s'intéressent à l'études des hydrates de gaz à l'échelle du micromètre ont produit des résultats qui pourraient pallier ce problème, ou du moins alimenter les discussions sur le choix de modèles adéquats.

De plus, les temps de calculs d'homogénéisation peuvent devenir assez importants lorsque l'on augmente la résolution des géométries c'est pourquoi le code demande encore d'être optimisé pour la gestion de la mémoire allouée mais aussi pour la gestion des processus. La parallélisation du code pourrait être une piste d'amélioration. La parallélisation du calcul de la méthode aux éléments finis au niveau de la macrosctructure dans l'approche multi-échelle est également importante.

L'application du code à des microstructures réelles a été présentée brièvement au chapitre 5 mais cela implique de faire des choix dans les traitements d'images avant calcul. Ces choix peuvent avoir des conséquences sur la réponse macroscopique du milieu homogénéisé. C'est pourquoi il faudrait éclaircir ce point, notamment en appliquant des règles empruntées à la mécanique statistique sur la question de la représentativité de la cellule unitaire.

7.3 Perspectives

Pour des applications futures du code développé pendant la thèse, il peut être intéressant de développer des lois constitutives mécaniques macroscopiques pour les sédiments contenant des hydrates de gaz et ce pour différents types de microstructures, en se basant sur des calculs d'homogénéisation sous plusieurs chargements macroscopiques.
La théorie de l'homogénéisation peut également s'appliquer à des problèmes de mécanique des fluides, une poursuite envisagée de ce travail de thèse serait donc d'élargir l'application du code à ce domaine puisque les phénomènes de transport jouent également un rôle non négligeable dans le comportement des sédiments contenant des hydrates de gaz. Cela aiderait à la caractérisation des propriétés comme la perméabilité de ces sols et offrirait un complément d'analyse aux essais expérimentaux qui restent encore difficiles à réaliser du fait des conditions extrêmes requises pour maintenir la stabilité des hydrates de gaz.

L'application du modèle multi-échelle présenté au chapitre 6 est envisagée pour des simulations d'éprouvettes de laboratoires soumises à des essais triaxiaux. Ces éprouvettes pourraient être définies par différentes microstructures typiques des sédiments granulaires contenant des hydrates de gaz, et par différentes fractions volumiques des phases constitutives du matériau global. Les résultats d'observations par tomographies comme ceux de la tâche 2 du projet ANR HYDRE peuvent fournir les données nécessaires à la definition de ces microstructures. Enfin à plus longue échéance une application à plus grande échelle est également envisageable, pour simuler le comportement de réservoirs par exemple avec l'ajout d'autre phénomènes physique au niveau macroscopique comme les phénomènes thermodynamiques ou de transports.

Bibliography

A

Al Mahbub, A. and A. Haque (2016). „X-ray Computed Tomography Imaging of the Microstructure of Sand Particles Subjected to High Pressure One-Dimensional Compression“. *Materials* 9.11, p. 890 (cit. on p. 94).

Archer, D. (2007). „Methane hydrate stability and anthropogenic climate change“. *Biogeosciences*, pp. 521–544 (cit. on p. 29).

B

Bagherzadeh, S. A., I. L. Moudrakovski, J. A. Ripmeester, and P. Englezos (2011). „Magnetic Resonance Imaging of Gas Hydrate Formation in a Bed of Silica Sand Particles“. *Energy & Fuels* 25, pp. 3083–3092 (cit. on p. 26).

Balay, S., S. Abhyankar, M. Adams, et al. (2019). *PETSc Web page*. `https://www.mcs.anl.gov/petsc` (cit. on pp. 71, 74, 118).

Bornert, M. (1996). „Morphologie microstructurale et comportement mécanique ; caractérisations expérimentales, approches par bornes et estimations autocohérentes généralisées“. PhD thesis. Ecole Nationale des Ponts et Chaussées (cit. on p. 114).

Boswell, R. and T. S. Collett (2011). „Current perspectives on gas hydrate resources“. *Energy and Environmental Science* 4.4, pp. 1206–1215 (cit. on p. 28).

Boswell, R., K. Yamamoto, S.-r. Lee, T. Collett, and P. Kumar (2014). „Chapter 8. Methane Hydrates“. *Future Energy*. 2nd ed. Elsevier Ltd, pp. 159–178 (cit. on pp. 25, 26).

Briaud, J.-L. and A. Chaouch (1997). „Hydrate melting in soil around hot conductor“. *Journal of geotechnical and geoenvironmental engineering* 123.7, pp. 645–653 (cit. on p. 29).

Brisard, S. (2018). *moisan2011*. `https://github.com/sbrisard/moisan2011` (cit. on p. 98).

Brisard, S. and L. Dormieux (2010). „FFT-based methods for the mechanics of composites: A general variational framework“. *Computational Materials Science* 49.3, pp. 663–671 (cit. on pp. 68, 70, 71).

Buffett, B. A. and O. Y. Zatsepina (2000). „Formation of gas hydrate from dissolved gas in natural porous media“. *Marine Geology* 164, pp. 69–77 (cit. on pp. 21, 31).

C

Chaouachi, M. (2015). „Microstructure of gas hydrates in sedimentary matrices“. PhD thesis. UNiversité de Göttingen (cit. on pp. 27, 91).

Chaouachi, M., A. Falenty, K. Sell, F. Enzmann, M. Kersten, D. Haberthür, and W. Kuhs (2015). „Microstructural evolution of gas hydrates in sedimentary matrices observed with synchrotron X-ray computed tomographic microscopy“. *Geochemistry* 16, pp. 1711–1722 (cit. on pp. 26, 27, 98).

Claypool, G. E. and K. A. Kvenvolden (1983). „Methane and other hydrocarbon gases in marine sediment“. *Annual Review of Earth and Planetary Sciences* 11, pp. 299–327 (cit. on p. 25).

Clayton, C., J. A. Priest, and A. Best (2005). „The effects of disseminated methane hydrate on the dynamic stiffness and damping of a sand“. *Géotechnique* 55.6, pp. 423–434 (cit. on pp. 31, 33, 34).

Collett, T., J.-j. Bahk, R. Baker, et al. (2015). „Methane Hydrates in Nature-Current Knowledge and Challenges“. *Journal of chemical and engineering data* 60.2, pp. 319–329 (cit. on p. 27).

Collett, T. S. (2002). „Energy resource potential of natural gas hydrates“. *AAPG Bulletin* 86.11, pp. 1971–1992 (cit. on pp. 24, 25).

Cortes, D. D., A. I. Martin, T. S. Yun, F. M. Francisca, J. C. Santamarina, and C. Ruppel (2009). „Thermal conductivity of hydrate-bearing sediments“. *Journal of Geophysical Research* 114.B11103 (cit. on p. 40).

D

Dai, S., J.-h. Cha, E. J. Rosenbaum, W. Zhang, and Y. Seol (2015). „Thermal conductivity measurements in unsaturated hydrate-bearing sediments“. *Geophysical Research Letters* 42, pp. 6295–6305 (cit. on p. 40).

Dai, S. and J. C. Santamarina (2014). „Sampling disturbance in hydrate-bearing sediment pressure cores : NGHP-01 expedition , Krishna e Godavari Basin example“. *Marine and Petroleum Geology* 58, pp. 178–186 (cit. on pp. 31, 40).

Dangla, P. (2017). *Bil*. `https://github.com/dangla/bil` (cit. on pp. 74, 75).

Dormieux, L., D. Kondo, and F. J. Ulm (2006). *Microporomechanics*. Ed. by L. John Wiley & Sons. Wiley. 1. Chippenham (cit. on pp. 45, 47).

Durham, W. B., S. H. Kirby, L. A. Stern, and W. Zhang (2003a). „The strength and rheology of methane clathrate hydrate“. *Journal of Geophysical Research* 108.B4 (cit. on p. 17).

Durham, W. B., L. A. Stern, and S. H. Kirby (2003b). „Ductile flow of methane hydrate“. *Canadian journal of physics* 81.1-2 (cit. on p. 17).

E

Ebinuma, T., Y. Kamata, H. Minagawa, R. Ohmura, J. Nagao, and H. Narita (2005). „Mechanical properties of sandy sediment containing methane hydrate“. *The Fifth International Conference on Gas Hydrates*. Trondheim, Norway (cit. on pp. 25, 31, 33, 34, 36, 38, 91).

Eshelby, J. D. (1957). „The determination of the elastic field of an ellipsoidal inclusion, and related problems“. *Proceedings of the Royal Society of London A.* 241, pp. 376–396 (cit. on p. 47).

Eyre, D. J. and G. W. Milton (1999). „A fast numerical scheme for computing the response of composites using grid refinement“. *The European Physical Journal Applied Physics* 6.1, pp. 41–47 (cit. on p. 68).

F

Freij-ayoub, R., C. Tan, B. Clennell, B. Tohidi, and J. Yang (2007). „A wellbore stability model for hydrate bearing sediments“. *Journal of Petroleum Science and Engineering* 57.1-2, pp. 209–220 (cit. on pp. 42, 43).

Frigo, M. and S. Johnson (2005). „The Design and Implementation of FFTW3“. *Proceedings of the IEEE* 93.2. Special issue on “Program Generation, Optimization, and Platform Adaptation”, pp. 216–231 (cit. on pp. 74, 118).

G

Geers, M. G. D., V. G. Kouznetsova, and W. A. M. Brekelmans (2010). „Journal of Computational and Applied Multi-scale computational homogenization : Trends and challenges“. *Journal of Computational and Applied Mathematics* 234.7, pp. 2175–2182 (cit. on pp. 114, 115).

Gélébart, L. and R. Mondon-Cancel (2013). „Non-linear extension of FFT-based methods accelerated by conjugate gradients to evaluate the mechanical behavior of composite materials“. *Computational Materials Science* 77, pp. 430–439 (cit. on pp. 70–72, 75, 76, 89, 125, 129).

Geuzaine, C. and J.-F. Remacle (2009). „Gmsh : a three-dimensional finite element mesh generator with built-in pre- and post-processing facilities“. *International journal for numerical methods in engineering* 79.11, pp. 1309–1331 (cit. on p. 75).

Ghiassian, H. and J. L. Grozic (2013). „Strength behavior of methane hydrate bearing sand in undrained triaxial testing“. *Marine and Petroleum Geology* 43, pp. 310–319 (cit. on pp. 34, 35).

Gibbs, J. W. (1928). *The collected works of J . Willard Gibbs, Thermodynamics*. Vol. I. New-York: Longmans, Green, pp. 55–353 (cit. on p. 14).

Glasby, G. P. (2003). „Potential impact on climate of the exploitation of methane hydrate deposits offshore“. *Marine and Petroleum Geology* 20.2, pp. 163–175 (cit. on p. 29).

Göküzüm, F. S. and M.-A. Keip (2018). „An algorithmically consistent macroscopic tangent operator for FFT-based computational homogenization“. *International journal for numerical methods in engineering* 113, pp. 581–600 (cit. on pp. 114, 116, 118, 124, 126, 130).

Guerin, G., D. Goldberg, and A. Meltser (1999). „Characterization of in situ elastic properties of gas hydrate-bearing sediments on the Blake Ridge“. *Journal of Geophysical Research* 104.B8, pp. 781–795 (cit. on p. 31).

Gupta, A. (2007). „Methane hydrate dissociation measurements and modeling: the role of heat transfer and reaction kinetics“. PhD thesis. Colorado School of Mines (cit. on pp. 18, 21).

Gupta, A., J. Lachance, E. D. Sloan, and C. A. Koh (2008). „Measurements of methane hydrate heat of dissociation using high pressure differential scanning calorimetry“. *Chemical Engineering Science* 63, pp. 5848–5853 (cit. on pp. 20, 21).

Gupta, S., R. Helmig, and B. Wohlmuth (2015). „Non-isothermal, multi-phase, multi-component flows through deformable methane hydrate reservoirs“. *Computational Geosciences* 19, pp. 1063–1088 (cit. on p. 42).

Gupta, S., B. Wohlmuth, and R. Helmig (2016). „Multi-rate time stepping schemes for hydro-geomechanical model for subsurface methane hydrate reservoirs“. *Advances in Water Resources* 91, pp. 78–87 (cit. on p. 42).

H

Hammerschmidt, E. G. (1934). „Formation of Gas Hydrates in Natural Gas Transmission Lines“. *Industrial and engineering chemistry* 26.8, pp. 851–855 (cit. on p. 11).

Handa, P. Y. (1990). „Effect of Hydrostatic pressure and salinity on the stability of gas hydrates“. *Journal of Physical Chemistry* 1.94, pp. 2652–2657 (cit. on p. 22).

Handa, Y. P. (1986). „Compositions, enthalpies of dissociation, and heat capacities in the range 85 to 270 K for clathrate hydrates of methane, ethane, and propane, and enthalpy of dissociation of isobutane hydrate, as determined by a heat-flow calorimeter“. *Journal of Chemical Thermodynamics* 18, pp. 915–921 (cit. on pp. 20, 21).

Helgerud, M. B., W. F. Waite, S. H. Kirby, and A. Nur (2003). „Measured temperature and pressure dependence of Vp and Vs in compacted , polycrystalline sI methane and sII methane – ethane hydrate“. *Canadian journal of physics* 81.1-2, pp. 47–53 (cit. on pp. 17, 18).

Helgerud, M. B., W. F. Waite, S. H. Kirby, and A. Nur (2009). „Elastic wave speeds and moduli in polycrystalline ice Ih , sI methane hydrate , and sII methane-ethane hydrate“. *Journal of Geophysical Research* 114.B02212 (cit. on p. 17).

Heriot-Watt Institute of Petroleum Engineering (2018). *What are gas hydrates ?* (Cit. on p. 13).

Hyodo, M., A. F. L. Hyde, Y. Nakata, N. Yoshimoto, M. Fukunaga, K. Kubo, Y. Nanjo, T. Matsuo, and K. Nakamura (2002). „Triaxial Compressive Strength of Methane Hydrate“. *The Twelfth International Offshore and Polar Engineering Conference*. Kitakyushu, Japan, pp. 422–428 (cit. on pp. 17–19, 100).

Hyodo, M., Y. Nakata, N. Yoshimoto, and T. Ebinuma (2005). „Basic research on the mechanical behavior of methane hydrate-sediments mixture“. *Soils and Foundations* 45.1, pp. 75–85 (cit. on pp. 17, 31).

Hyodo, M., J. Yoneda, N. Yoshimoto, and Y. Nakata (2013). „Mechanical and dissociation properties of methane hydrate-bearing sand in deep seabed“. *Soils and Foundations* 53.2, pp. 299–314 (cit. on pp. 31–34, 36, 37, 55–58).

J

Jan Lehmköster et al. (2014). *Marine Resources - Opportunities and Risks*. Tech. rep. Hamburg: maribus gGmbH (cit. on p. 28).

Jeffrey, G. A. (1984). *Inclusion Compounds*. Ed. by J. Atwood, J. Davies, and D. MacNichol. Vol. 1. London: Academic Press, p. 135 (cit. on p. 12).

K

Kamath, V. (1984). „Study of heat transfer characteristics during dissociation of gas hydrates in porous media“. PhD thesis. University of Pittsburgh (cit. on p. 15).

Kato, A., Y. Nakata, M. Hyodo, and N. Yoshimoto (2016). „Macro and micro behaviour of methane hydrate-bearing sand subjected to plane strain compression“. *Soils and Foundations* 56.5, pp. 835–847 (cit. on p. 34).

Kayen, R. E. and H. J. Lee (1991). „Pleistocene Slope Instability of Gas Hydrate-Laden Sediment on the Beaufort Sea Margin“. *Marine Geotechnology* 10, pp. 125–141 (cit. on p. 29).

Kennett, J., G. Cannariato, I. Hendy, and R. Behl (2003). *Methane hydrates in quaternary climate change : the clathrate gun hypothesis*. Ed. by T. A. G. Union. The American Geophysiscal Union (cit. on p. 29).

Kim, H. C., P. R. Bishnoi, R. A. Heidemann, and S. S. H. Rizvi (1987). „Kinetics of methane hydrate decomposition“. *Chemical Engineering Science* 42.7, pp. 1645–1653 (cit. on p. 42).

Kimoto, S., F. Oka, and T. Fushita (2010a). „A chemo-thermo-mechanically coupled analysis of ground deformation induced by gas hydrate dissociation“. *International Journal of Mechanical Sciences* 52.2, pp. 365–376 (cit. on p. 42).

Kimoto, S., F. Oka, and T. Fushita (2010b). „A chemo-thermo-mechanically coupled analysis of ground deformation induced by gas hydrate dissociation“. *International Journal of Mechanical Sciences* 52.2, pp. 365–376 (cit. on p. 43).

Klar, A., K. Soga, and M. Y. A. Ng (2010). „Coupled deformation–flow analysis for methane hydrate extraction“. *Géotechnique* 60.10, pp. 765–776 (cit. on pp. 42, 43).

Klar, A., S. Uchida, K. Soga, and K. Yamamoto (2013). „Formulation for Gas-Hydrate Sediments Explicitly Coupled Thermal Flow Mechanical Formulation for Gas-Hydrate Sediments“. *Society of Petroleum Engineers* 18.2, pp. 196–206 (cit. on p. 42).

Kneafsey, T. J., Y. Seol, A. Gupta, and L. Tomutsa (2011). „Permeability of Laboratory-Formed Methane-Hydrate-Bearing Sand : Measurements and Observations Using X-Ray Computed Tomography“. *Society of Petroleum Engineers* 16, pp. 78–94 (cit. on p. 40).

Konno, Y., Y. Jin, T. Uchiumi, and J. Nagao (2013). „Multiple-pressure-tapped core holder combined with X-ray computed tomography scanning for gas–water permeability measurements of methane-hydrate-bearing sediments“. *Review of scientific Instruments* 84.064501 (cit. on p. 40).

Konno, Y., J. Yoneda, K. Egawa, T. Ito, Y. Jin, M. Kida, K. Suzuki, T. Fujii, and J. Nagao (2015). „Permeability of sediment cores from methane hydrate deposit in the Eastern Nankai Trough“. *Marine and Petroleum Geology* 66, pp. 487–495 (cit. on pp. 40, 41).

Kouznetsova, V., W. A. M. Brekelmans, and F. P. T. Baaijens (2001). „An approach to micro-macro modeling of heterogeneous materials“. *Computational Mechanics* 27, pp. 37–48 (cit. on p. 114).

Kurihara, M., H. Ouchi, T. Inoue, T. Yonezawa, Y. Masuda, S. R. Dallimore, and T. S. Collett (2005). „Analysis of the JAPEX/JNOC/GSC et al. Mallik 5L-38 gas hydrate thermal-production test through numerical simulation“. *Geological Survey of Canada Bulletin* 585 (cit. on p. 41).

Kvenvolden, K. A. (1988). „Methane hydrate a major reservoir of carbon in the shallow geosphere?“ *Chemical Geology* 71, pp. 41–51 (cit. on p. 16).

Kvenvolden, K. A. (1993). „Gas hydrates Geological perspective and global change“. *Reviews of Geophysics* 31.2, pp. 173–187 (cit. on p. 16).

L

Le, T. X., P. Aimedieu, M. Bornert, B. Chabot, and A. M. Tang (2019). „Effect of temperature cycle on mechanical properties of methane hydrate-bearing sediment“. *Soils and Foundations* 59, pp. 814–827 (cit. on pp. 95, 105, 108, 109).

Le, T.-X. (2019). „Etude expérimentale des propriétés mécaniques et de la microstructure des sédiments contenant des hydrates de méthane“. PhD thesis. Paris Est (cit. on pp. 105, 106).

Li, C.-h., Q. Zhao, H.-j. Xu, K. Feng, and X.-w. Liu (2014). „Relation between relative permeability and hydrate saturation in Shenhu area, South China Sea“. *Applied Geophysics* 11.2, pp. 207–214 (cit. on p. 40).

Li, J.-f., J.-l. Ye, X.-w. Qin, H.-j. Qiu, N.-y. Wu, H.-l. Lu, and W.-w. Xie (2018). „China Geology The first offshore natural gas hydrate production test in South China Sea“. *China Geology* 1.1, pp. 5–16 (cit. on p. 27).

Lin, J.-s., Y. Seol, and J. H. Choi (2015). „An SMP critical state model for methane hydrate-bearing sands“. *International Journal for Numerical and Analytical Methods in Geomechanics* 39.9, pp. 969–987 (cit. on pp. 43, 44).

Liu, C.-s., P. Schnürle, Y. Wang, S.-H. Chung, S.-C. Chen, and T.-H. Hsiuan (2006). „Distribution and Characters of Gas Hydrate Offshore of Southwestern Taiwan“. *Terrestrial, Atmospheric and Oceanic sciences journal* 17.4, pp. 615–644 (cit. on p. 30).

Lu, W., M. I. Chou, and R. C. Burruss (2008). „Determination of methane concentrations in water in equilibrium with sI methane hydrate in the absence of a vapor phase by in situ Raman spectrocospy“. *Geochimica et Cosmochimica Acta* 72, pp. 412–422 (cit. on p. 22).

M

Macdonald, I. R., N. L. Guinasso JR., R. Sassen, J. M. Brooks, L. Lee, and K. T. Scott (1994). „Gas hydrate that breaches the sea floor on the continental slope of the Gulf of Mexico“. *Geology* 22.8, pp. 699–702 (cit. on p. 29).

Makogon, Y. F. (1997). *Hydrates of hydrocarbons*. Tulsa, Oklahoma: Pennwell Books (cit. on p. 11).

Makogon, Y. F. (2010). „Natural gas hydrates - A promising source of energy“. *Journal of Natural Gas Science and Engineering* 2, pp. 49–59 (cit. on pp. 11, 12, 27).

Malagar, B. R. C., K. P. Lijith, and D. N. Singh (2019). „Formation & dissociation of methane gas hydrates in sediments : A critical review“. *Journal of Natural Gas Science and Engineering* 65, pp. 168–184 (cit. on pp. 25, 31, 33).

Maslin, M., M. Owen, R. Betts, S. Day, T. Dunkley Jones, and A. Ridgwell (2010). „Gas hydrates: past and future geohazard?“ *Philosophical Transactions of the Royal Society A: Mathematical, Physical and Engineering Sciences* 368, pp. 2369–2393 (cit. on p. 29).

Masui, A., H. Haneda, Y. Ogata, and K. Aoki (2006). „Triaxial compression test on submarine sediment containing methane hydrate in deap sea off the coast off Japan“. Japonais. *41st Annual Conference, Jpn. Geotech. Soc.* (Cit. on pp. 31, 34).

Masui, A., H. Haneda, Y. Ogata, and K. Aoki (2005). „The effect of saturation degree of methane hydrate on the shear strength of synthetic methane hydrate sediments“. *The 5th International Conference on Gas Hydrates, Trondheim, Norway*, pp. 657–663 (cit. on pp. 25, 31, 33, 34, 36–38, 52, 54, 55, 57, 58).

Matouš, K., M. G. D. Geers, V. G. Kouznetsova, and A. Gillman (2017). „A review of predictive nonlinear theories for multiscale modeling of heterogeneous materials“. *Journal of Computational Physics* 330, pp. 192–220 (cit. on p. 115).

Mcknight, R. E. A., T. Moxon, A. Buckley, P. A. Taylor, T. W. Darling, and M. A. Carpenter (2008). „Grain size dependence of elastic anomalies accompanying the $\alpha - \beta$ phase transition in polycrystalline quartz“. *Journal of Physics: Condensed Matter* 20.075229 (cit. on p. 93).

Michel, J. C., H. Moulinec, and P. Suquet (2000). „A computational method based on augmented lagrangians and fast fourier transforms for composites with high contrast“. *Computer Modeling in Engineering and Sciences* 1.2, pp. 79–88 (cit. on p. 68).

Miehe, C. (1996). „Numerical computation of algorithmic (consistent) tangent moduli in large-strain computational inelasticity“. *Computer Methods in Applied Mechanics and Engineering* 134, pp. 223–240 (cit. on p. 114).

Miehe, C., J. Schotte, and J. Schröder (1999). „Computational micro ± macro transitions and overall moduli in the analysis of polycrystals at large strains rg Schr o“. *Computational Materials Science* 16, pp. 372–382 (cit. on p. 116).

Minagawa, H., Y. Nishikawa, I. Ikeda, K. Miyazaki, N. Takahara, Y. Sakamoto, T. Komai, and H. Narita (2008). „Characterization of sand sediment by pore size distribution and permeability using proton nuclear magnetic resonance measurement“. *Journal of Geophysical Research* 113.B07210 (cit. on p. 40).

Miyazaki, K., A. Masui, H. Haneda, Y. Ogata, K. Aoki, and T. Yamaguchi (2008). „Variable-Compliance-Type Constitutive Model for Methane Hydrate Bearing Sediment“. *Proceedings of the 6th International Conference on Gas Hydrates (ICGH 2008)*. Icgh. Vancouver (cit. on p. 31).

Miyazaki, K., A. Masui, Y. Sakamoto, K. Aoki, N. Tenma, and T. Yamaguchi (2011). „Triaxial compressive properties of artificial methane-hydrate-bearing sediment“. *Journal of Geophysical Research: Solid Earth* 116.B06102 (cit. on pp. 31, 34, 37, 49, 51–53).

Miyazaki, K., N. Tenma, K. Aoki, and T. Yamaguchi (2012). „A Nonlinear Elastic Model for Triaxial Compressive Properties of Artificial Methane-Hydrate-Bearing Sediment Samples“. *Energies* 5, pp. 4057–4075 (cit. on p. 43).

Moisan, L. (2011). „Periodic Plus Smooth Image Decomposition“. *Journal of Mathematical Imaging and Vision* 39.2, pp. 161–179 (cit. on p. 98).

Moridis, G. J. (2003). „Numerical Studies of Gas Production From Methane Hydrates“. *Society of Petroleum Engineers*, pp. 359–370 (cit. on p. 41).

Moridis, G. J. (2014). *User's manual for the hydrate v1.5 option of TOUGH+ v1.5: A code for the simulation of system behavior in hydrate-bearing geologic media*. Tech. rep. Berkeley: Lawrence Berkeley National Laboratory (cit. on pp. 41, 42).

Moulinec, H. and P. Suquet (1994). „A fast numerical method for computing the linear and nonlinear mechanical properties of composites“. *Comptes Rendus de l'Académie des Sciences Série II* 318.11, pp. 1417–1423 (cit. on pp. 63–65, 67, 68, 70, 71, 74).

Moulinec, H. and P. Suquet (1998). „A numerical method for computing the response of composites with complex microstructure“. *Computer Methods in Applied Mechanics and Engineering* 157, pp. 69–94 (cit. on pp. 64, 68, 69, 71, 75).

N

Ning, F., Y. Yu, S. Kjelstrup, J. H. Vlugt, and K. Glavatskiy (2012). „Mechanical properties of clathrate hydrates : status and perspectives“. *Energy & Environmental Science* 5, pp. 6779–6795 (cit. on p. 17).

O

Oyama, A. and S. M. Masutani (2017). „A Review of the Methane Hydrate Program in Japan“. *Energies* 10.10, p. 1447 (cit. on p. 27).

P

Pecher, I. A., C. R. Ranero, R. von Huene, T. A. Minshull, and S. C. Singh (1998). „The nature and distribution ofbottom simulating reflectors at the Costa Rican convergent margin Ingo“. *Geophysical Journal International* 133, pp. 219–229 (cit. on p. 30).

Pinkert, S. and J. L. H. Grozic (2014). „Journal of Geophysical Research : Solid Earth Prediction of the mechanical response of hydrate-bearing sands“. *Journal of Geophysical Research: Solid Earth* 119, pp. 4695–4707 (cit. on p. 43).

Potts, D. M. and L. Zdravkovic (1999). *Finite element analysis in geotechnical engineering*. Bath: Thomas Telford Publishing (cit. on pp. 69, 70, 113).

R

Rees, E. V., J. A. Priest, and C. R. Clayton (2011). „The structure of methane gas hydrate bearing sediments from the Krishna-Godavari Basin as seen from Micro-CT scanning“. *Marine and Petroleum Geology* 28, pp. 1283–1293 (cit. on pp. 27, 91, 98, 99).

Rutqvist, J. and G. J. Moridis (2007). „Numerical Studies on the Geomechanical Stability of Hydrate-Bearing Sediments“. *Offshore Technology Conference*. Houston, Texas, USA (cit. on p. 42).

Rutqvist, J. and G. J. Moridis (2009). „Numerical Studies on the Geomechanical Stability of Hydrate-Bearing Sediments“. *Society of Petroleum Engineers* 14.2, pp. 267–282 (cit. on p. 42).

S

Sánchez, M., X. Gai, and J. C. Santamarina (2017). „Computers and Geotechnics A constitutive mechanical model for gas hydrate bearing sediments incorporating inelastic mechanisms“. *Computers and Geotechnics* 84, pp. 28–46 (cit. on pp. 43, 44).

Sánchez, M., C. Santamarina, M. Teymouri, and X. Gai (2018). „Coupled Numerical Modeling of Gas Hydrate-Bearing Sediments : From Laboratory to Field-Scale Analyses“. *Journal of Geophysical Research: Solid Earth* 123, pp. 10, 326–10, 348 (cit. on pp. 42, 43).

Santamarina, J. C., S. Dai, J. Jang, and M. Terzariol (2012). „Pressure Core Characterization Tools for Hydrate-Bearing Sediments“. *Scientific Drilling* 14, pp. 44–48 (cit. on p. 30).

Santamarina, J. C. and C. Ruppel (2008). „The impact of hydrate saturation on the mechanical, electrical and thermal properties of hydrate-bearing sand, silts, and clay“. *The 6th International Conference on Gas Hydrates*. Vancouver, Canada (cit. on p. 33).

Seol, Y. and T. J. Kneafsey (2011). „Methane hydrate induced permeability modification for multiphase flow in unsaturated porous media“. *Journal of Geophysical Research* 116.B08102 (cit. on p. 40).

Shedd, W., R. Boswell, M. Frye, P. Godfriaux, and K. Kramer (2012). „Occurrence and nature of “ bottom simulating re fl ectors ” in the northern Gulf of Mexico“. *Marine and Petroleum Geology* 34, pp. 31–40 (cit. on p. 30).

Sloan, E. D. and C. Koh (2007). *Clathrate Hydrates of Natural Gases*. Ed. by T. Group and Francis. 3rd. Boca Raton: CRC Press, p. 752 (cit. on pp. 11–18, 21–25, 29, 30, 51, 52, 57, 95, 100).

Soga, K., S. L Lee, M. Y A Ng, and A. Klar (Nov. 2006). „Characterisation and engineering properties of Methane hydrate soils“. Vol. 4, pp. 2591–2642 (cit. on pp. 25, 32, 38, 41).

Stern, L. A., S. Circone, S. H. Kirby, and W. B. Durham (2003). „Temperature, pressure, and compositional effects on anomalous or “ self ” preservation of gas hydrates“. *Canadian journal of physics* 81, pp. 271–283 (cit. on p. 23).

Stern, L. A., S. H. Kirby, and W. B. Durham (1996). „Peculiarities of Methane Clathrate Hydrate Formation and Solid-State Deformation , Including Possible Superheating of Water Ice“. *Science* 273, pp. 1843–1848 (cit. on p. 17).

Stern, L. A., S. H. Kirby, and W. B. Durham (1998). „Polycrystalline Methane Hydrate : Synthesis from Superheated Ice , and Low-Temperature Mechanical Properties“. *Energy & Fuels* 12, pp. 201–211 (cit. on p. 33).

Subramanian, S. and E. D. Sloan (2002). „Solubility Effects on Growth and Dissolution of Methane Hydrate Needles“. *The 4th International Conference on Gas Hydrates*. Yokohama, Japan (cit. on p. 22).

Sultan, N., P. Cochonat, M. Canals, et al. (2004a). „Triggering mechanisms of slope instability processes and sediment failures on continental margins : a geotechnical approach“. *Marine Geology* 213, pp. 291–321 (cit. on p. 29).

Sultan, N., P. Cochonat, J. Foucher, and J. Mienert (2004b). „Effect of gas hydrates melting on seafloor slope instability“. *Marine Geology* 213, pp. 379–401 (cit. on p. 29).

Sultan, N. and S. Garziglia (2011). „Geomechanical constitutive modelling of gas-hydrate-bearing sediments“. *Proceedings of the 7th International Conference on Gas Hydrates*. Icgh. Edinburgh, pp. 1–11 (cit. on p. 43).

Sun, R. and Z. Duan (2007). „An accurate model to predict the thermodynamic stability of methane hydrate and methane solubility in marine environments“. *Chemical Geology* 244, pp. 248–262 (cit. on p. 22).

Suquet, P. (1990). „Une méthode simplifiée pour le calcul des propriétés élastiques de matériaux hétérogènes à structure périodique“. *Comptes Rendus de l'Académie des Sciences Série II* 311, pp. 769–774 (cit. on p. 63).

T

Taleb, F., S. Garziglia, and N. Sultan (2018). „Hydromechanical Properties of Gas Hydrate-Bearing Fine Sediments From In Situ Testing“. *Journal of Geophysical Research: Solid Earth* 123, pp. 9615–9634 (cit. on p. 30).

U

Uchida, S., K. Soga, and K. Yamamoto (2012). „Critical state soil constitutive model for methane hydrate soil“. *Journal of Geophysical Research: Solid Earth* 117.3, pp. 1–13 (cit. on pp. 43, 44, 55).

Uchida, T. and T. Tsuji (2004). „Petrophysical properties of natural gas hydrates-bearing sands and their sedimentology in the Nankai trough“. *Resource Geology* 54.1, pp. 79–87 (cit. on p. 40).

Ulm, F. J., G. Constantinides, and F. H. Heukamp (2004). „Is concrete a poromechanics materials?-A multiscale investigation of poroelastic properties“. *Materials and Structures* 37, pp. 43–58 (cit. on pp. 48, 50).

V

Villard, P. (1895). „Propriétés physiques de l'acétylène ; hydrate d'acétylène". *Comptes Rendus de l'Académie des Sciences* 120, p. 1262 (cit. on p. 13).

W

Waite, F., J. Santamarina, D. Cortes, et al. (2009). „Physical properties of hydrate-bearing sediments". *Reviews of Geophysics* 47.RG4003 (cit. on pp. 20, 21, 25, 26, 33, 40, 91).

Waite, W. F., L. Y. Gilbert, W. J. Winters, and D. H. Mason (2005). „Thermal property measurements in tetrahydrofuran (THF) hydrate and hydrate-bearing sediment between -25 and +4°C, and their application to methane hydrate". *Fifth International Conference on Gas Hydrates*. Trondheim, Norvège (cit. on pp. 18, 20).

Waite, W. F., W. J. Winters, and D. H. Mason (2004). „Methane hydrate formation in partially water-saturated Ottawa sand". *American Mineralogist* 89, pp. 1202–1207 (cit. on p. 31).

Weitemeyer, K. A., S. C. Constable, K. W. Key, and J. P. Behrens (2006). „First results from a marine controlled-source electromagnetic survey to detect gas hydrates offshore Oregon". *Geophysical Research Letters* 33 (cit. on p. 30).

White, M. D. and B. P. Mcgrail (2008). „Numerical Simulation of Methane Hydrate Production from Geologic Formations via Carbon Dioxide Injection". *Offshore Technology Conference*. Houston, Texas, USA (cit. on p. 41).

White, M. D. and M. Oostrom (2006). *Subsurface Transport Over Multiple Phases User 's Guide*. Tech. rep. Pacific Northwest National Laboratory (cit. on p. 41).

Wilder, J. W., G. J. Moridis, S. J. Wilson, et al. (2008). „An international effort to compare gas hydrate reservoir simulators". *The 6th International Conference on Gas Hydrates*. Vancouver, Canada (cit. on p. 42).

Willot, F. (2015). „Fourier-based schemes for computing the mechanical response of composites with accurate local fields". *Comptes Rendus Mecanique* 343.3, pp. 232–245 (cit. on pp. 68, 71–73, 79, 81).

Willot, F. and Y.-p. Pellegrini (2008). „Fast Fourier Transform computations and build-up of plastic deformation in 2D, elastic-perfectly plastic, pixelwise disordered porous media". *Continuum Models and Discrete Systems* (cit. on p. 71).

Winters, W. J., I. A. Pecher, W. F. Waite, and D. H. Mason (2004). „Physical properties and rock physics models of sediment containing natural and laboratory-formed methane gas hydrate". *American Mineralogist* 89, pp. 1221–1227 (cit. on p. 31).

Winters, W. J., I. A. Pecher, J. S. Booth, D. H. Mason, M. K. Relle, and W. P. Dillon (1999). „Properties of samples containing natural gas hydrate from the JAPEX/JNOC/GSC Mallik 2L-38 gas hydrate research well, determined using Gas Hydrate And Sediment Test Laboratory Instrument (GHASTLI)". *Geological Survey of Canada* Bulletin 5, pp. 241–250 (cit. on pp. 31, 34).

Winters, W. J., W. F. Waite, D. H. Mason, W. P. Dillon, and I. A. Pecher (2002). „Sediment properties associated with gas hydrate formation". *Fourth International Conference on gas hydrates*. Yokohama, pp. 722–727 (cit. on pp. 34, 35).

Y

Yoneda, J., M. Hyodo, N. Yoshimoto, Y. Nakata, and A. Kato (2013). „Development of high-pressure low-temperature plane strain testing apparatus for methane hydrate-bearing sand“. *Soils and Foundations* 53.5, pp. 774–783 (cit. on p. 34).

Yoneda, J., M. Kida, Y. Konno, Y. Jin, S. Morita, and N. Tenma (2019). „In Situ Mechanical Properties of Shallow Gas Hydrate Deposits in the Deep Seabed“. *Geophysical Research Letters* 46.24, pp. 14459–14468 (cit. on p. 95).

Yoneda, J., A. Masui, Y. Konno, Y. Jin, K. Egawa, M. Kida, T. Ito, J. Nagao, and N. Tenma (2015). „Mechanical behavior of hydrate-bearing pressure-core sediments visualized under triaxial compression“. *Marine and Petroleum Geology* 66, pp. 451–459 (cit. on pp. 31, 34).

Yu, F., W. Liu, Y. Song, Y. Li, R. Wang, and X. Nie (2011a). „Study on Strength of Artificial Methane Hydrate- Bearing Clay Sediments Under Triaxial Compression“. *Proceedings of the 7th International Conference on Gas Hydrates*. Edinburgh, Scotland, United Kingdom (cit. on p. 34).

Yu, F., Y. Song, W. Liu, Y. Li, and W. Lam (2011b). „Analyses of stress strain behavior and constitutive model of artificial methane hydrate“. *Journal of Petroleum Science and Engineering* 77.2, pp. 183–188 (cit. on pp. 17–20, 100).

Yun, T. S., J. C. Santamarina, and C. Ruppel (2007). „Mechanical properties of sand, silt, and clay containing tetrahydrofuran hydrate“. *Journal of Geophysical Research* 112.B04106 (cit. on pp. 33, 36, 39).

Z

Zatsepina, O. Y. and B. A. Buffett (1998). „Thermodynamic conditions for the stability of gas hydrate in the seafloor“. *Journal of Geophysical Research* 103.B10, pp. 24, 127–24, 139 (cit. on pp. 21, 22).

Zatsepina, O. Y. and B. A. Buffett (2001). „Experimental study of the stability of CO2-hydrate in a porous medium“. *Fluid Phase Equilibria* 192, pp. 85–102 (cit. on p. 33).

Zeman, J., J. Vondrejc, J. Novák, and I. Marek (2010). „Accelerating a FFT-based solver for numerical homogenization of periodic media by conjugate gradients“. *Journal of Computational Physics* 229, pp. 8065–8071 (cit. on pp. 68, 70).

Zhang, X.-H., X.-B. Lu, L.-M. Zhang, S.-Y. Wang, and Q.-P. Li (2012). „Experimental study on mechanical properties of methane-hydrate-bearing sediments.“ *Acta Mechanica Sinica* 28.5, pp. 1356–1366 (cit. on p. 34).

Zhao, J., L. Yang, Y. Liu, and Y. Song (2015). „Microstructural characteristics of natural gas hydrates hosted in various sand sediments“. *Physical Chemistry Chemical Physics* 17, pp. 22632–22641 (cit. on p. 26).

List of Figures

List of Tables